Strong field sub-femtosecond electronic processes

Alexander W. Bray

Research School of Physics
Australian National University

A thesis presented for the degree of
Doctor of Philosophy

February 28, 2020

Declaration

This thesis is an account of research undertaken between February 2017 and February 2020 at the Australian National University. The pages of this document constitute an original work which has not been submitted in whole or part to any other university.

Alexander W. Bray

February 28, 2020

Acknowledgements

I firstly must thank Professor Anatoli Kheifets, my supervisor, for his guidance, orchestration of the research conducted, and fantastic opportunities along the way. Next, I thank Doctor Serguei Patchkovskii for access to his codes which underpin this work, and for hosting me in Berlin, a time in which I learned a great deal. I additionally thank all of our many collaborators for their contributions, efforts, and insights towards the many projects I have been fortunate to be a part of. I acknowledge support of the the Deakin and Dean's Merit Scholarships from the Australian National University (ANU). I further acknowledge the ANU Vice-Chancellor's and the Atoms Journal travel grants, funds from the Max Born Institute (MBI), and Professor Kheifets' Australian Research Council Discovery Project for support of associated travel. I thank the National Computing Infrastructure and its equivalent at the MBI for providing the computational infrastructure critical to this work. Finally, I thank my friends, family, and loving wife.

Publications

Entries marked by an asterisk (*) are explicitly featured in this thesis.

A.W. Bray, D. Freeman, F. Naseem, V. K. Dolmatov, A. S. Kheifets, "Correlation enhanced HHG spectra of the Mn atom and Mn^+ ion," Phys. Rev. A, *Submitted*.

* **A.W. Bray**, U. Eichmann, S. Patchkovskii, "Dissecting strong-field excitation dynamics with atomic-momentum spectroscopy," Phys. Rev. Lett., *Submitted*.

S. Grundmann, V. Serov, F. Trinter, K. Fehre, N. Strenger, A. Pier, M. Kircher, D. Trabert, M. Weller, J. Rist, L. Kaiser, **A.W. Bray**, L. Ph. H. Schmidt, J. B. Williams, T. Jahnke, R. Dörner, M. S. Schöffler, and A. S. Kheifets, "Probing the two-electron cusp in the ground states of He and H_2," Phys. Rev. Lett., *Submitted*.

* **A.W. Bray**, "The attoclock and tunnelling time," J. Phys. Conf. Ser. (ICPEAC 2019), *Accepted*.

I. Bray, H. Hayat, D. V. Fursa, A.S. Kadyrov, **A.W. Bray**, M. Cytowski, "Complete calculations of electron scattering on H-like ions," Phys. Rev. A **101**, 022703 (2020).

* **A.W. Bray**, D. Freeman, S. Eckart, and A. S. Kheifets, "Correlation enhancement of high-order harmonic generation in Xe," Phys. Rev. A **100**, 013404 (2019).

V. V. Serov, **A.W. Bray**, and A. S. Kheifets, "Numerical attoclock on atomic and molecular hydrogen," Phys. Rev. A **99**, 063428 (2019).

* U. S. Sainadh, H. Xu, X. Wang, A. Atia-Tul-Noor, W. C. Wallace, N. Douguet, **A. Bray**, I. Ivanov, K. Bartschat, A. Kheifets, R. T. Sang, and I. V. Litvinyuk, "Attosecond angular streaking and tunnelling time in atomic hydrogen," Nature **568**, 75–77 (2019).

I. Bray, **A.W. Bray**, D. V. Fursa, and A. S. Kadyrov, "Near-threshold cross sections for electron and positron impact ionization of atomic hydrogen," Phys. Rev. Lett. **121**, 203401 (2018).

S. Grundmann, F. Trinter, **A.W. Bray**, S. Eckart, J. Rist, G. Kastirke, D. Metz, S. Klumpp, J. Viefhaus, L. P. H. Schmidt, J. B. Williams, R. Dörner, T. Jahnke, M. S. Schöffler, and A. S. Kheifets, "Separating dipole and quadrupole contributions to single-photon double ionization," Phys. Rev. Lett. **121**, 173003 (2018).

* **A.W. Bray**, F. Naseem, and A. S. Kheifets, "Photoionization of Xe and Xe@C_{60} from the 4*d* shell in RABBITT fields," Phys. Rev. A **98**, 043427 (2018).

* **A.W. Bray**, S. Eckart, and A. S. Kheifets, "Keldysh-Rutherford model for the attoclock," Phys. Rev. Lett. **121**, 123201 (2018).

A. Jain, T. Gaumnitz, **A. Bray**, A. Kheifets, and H. J. Wörner, "Photoionization delays in xenon using single-shot referencing in the collinear back-focusing geometry," Opt. Lett. **43**, 4510–4513 (2018).

* **A.W. Bray**, F. Naseem, and A. S. Kheifets, "Simulation of angular-resolved RABBITT measurements in noble-gas atoms," Phys. Rev. A **97**, 063404 (2018).

I. Bray, I. B. Abdurakhmanov, J. J. Bailey, **A.W. Bray**, D. V. Fursa, A. S. Kadyrov, C. M. Rawlins, J. S. Savage, A. T. Stelbovics, and M. C. Zammit, "Convergent close-coupling approach to light and heavy projectile scattering on atomic and molecular hydrogen," J. Phys. B **50**, 202001 (2017).

A.W. Bray, A. S. Kheifets, and I. Bray, "Calculation of atomic photoionization using the nonsingular convergent close-coupling method," Phys. Rev. A **95**, 053405 (2017).

A.W. Bray, I. Abdurakhmanov, A. Kadyrov, D. Fursa, and I. Bray, "Solving close-coupling equations in momentum space without singularities for charged targets," Comput. Phys. Commun. **212**, 55 – 58 (2017).

A. S. Kheifets, **A.W. Bray**, and I. Bray, "Attosecond time delay in photoemission and electron scattering near threshold," Phys. Rev. Lett. **117**, 143202 (2016).

I. I. Fabrikant, **A.W. Bray**, A. S. Kadyrov, and I. Bray, "Near-threshold behavior of positronium-antiproton scattering," Phys. Rev. A **94**, 012701 (2016).

A. Bray, I. Abdurakhmanov, A. Kadyrov, D. Fursa, and I. Bray, "Solving close-coupling equations in momentum space without singularities II," Comput. Phys. Commun. **203**, 147 – 151 (2016).

A. Bray, I. Abdurakhmanov, A. Kadyrov, D. Fursa, and I. Bray, "Solving close-coupling equations in momentum space without singularities," Comput. Phys. Commun. **196**, 276 – 279 (2015).

Notable presentations

A. W. Bray, "Current state of the attoclock and tunnelling time debate," Progress Report, ICPEAC XXXI, 2019, Deauville, France.

A. W. Bray, "Keldysh-Rutherford model for the attoclock," Poster, 49th Annual DAMOP meeting, 2018, Ft. Lauderdale, USA.

A. W. Bray, "Attoclock@hydrogen: Does the attoclock provide evidence of a tunnelling time?," Visiting scholar presentation, National University of Defence Technology, Changsha, China.

A. W. Bray, "Attosecond time delay in photoemission and electron scattering near threshold," Hot topic, ICPEAC XXX, 2017, Cairns, Australia.

A. W. Bray, "The nonsingular convergent close-coupling method: An application to positron-hydrogen scattering," Invited speaker, POSMOL 2017, Magnetic Island, Australia.

Contents

List of Figures

Abstract

This thesis is comprised of theoretical investigations on several different strong field and/or sub-femtosecond processes resulting from the interaction between atoms and short laser pulses. Said theory is based on the numeric solution of the time-dependent Schrödinger equation (TDSE) by high performance computing methods. Specifically, Chapter 2 examines the Attoclock, a strong field problem designed to clock the escape of an electron as it tunnel ionises. In which, we present both the result of a collaboration yielding the first agreement between *ab initio* theory and experiment [Sainadh *et al.*, Nature 568, 75 (2019)], and a straightforward model based on classical scattering for an idealised version of the problem [Bray *et al.*, Phys. Rev. Lett. 121, 123201 (2018)]. Chapter 3 considers reconstruction of attosecond beating by interference of two-colour transitions (RABBITT) in which an attosecond pulse train 'pump' and infrared pulse 'probe' simultaneously impinge on a target with a precisely controlled delay between them. The oscillating phase of the ionisation probability as a function of this delay yields the angular anisotropy parameter and Wigner time delay for its corresponding energy. We calculate and present these quantities for the valence p-shell of various noble gas atoms [Bray *et al.*, Phys. Rev. A 97, 063404 (2018)] and additionally examine the effect of an encapsulating C_{60} fullerene cage on the $4d$ shell of Xe [Bray *et al.*, Phys. Rev. A 98, 043427 (2018)]. In Chapter 4 we look at the effect of electron correlation on high harmonic generation (HHG), the process by which attosecond pulses are produced, from one and two colour fields. We perform single active electron calculations for the $5p$ shell of Xe and model the correlation as an enhancement factor taken as the ratio between photoionisation cross-sections computed with and without said correlations. Doing so we report solid agreement with experimentally observed spectra for both field setups [Bray *et al.*, Phys. Rev. A 100, 013404 (2019)]. Finally, Chapter 5 investigates the non-dipole problem of the state resolved strong field acceleration of neutral species. This requires the solution of the coupled two-body TDSE of the centre of mass and reduced mass electron, each with three degrees of freedom, in a non-spatially uniform field. Accordingly it necessitates its own dedicated solution method. Developing and applying said method to atomic hydrogen we compute

an acceleration for each state consistent with experimental observation [Bray *et al.*, Phys. Rev. Lett., *Submitted*]. Additionally our method allows us, via comparison with classical expressions, to derive the time at which each excited state was produced and, by similar means, an effective polarisibility for the ground state. Most interestingly this latter value is of opposite sign to the typical +9/2, providing an unambiguous signature of having entered the Kramers-Henneberger regime.

Chapter 1

Introduction

We begin with general motivation for the problems considered within this work and with definitions and theory common to two or more subsequent chapters. Note that our presentation is within a non-relativistic spin-free framework (will the small exception of Section 4.1.1) and given in atomic units.

1.1 Motivation

The role of time in quantum mechanics is under never greater scrutiny due to the development and application of ultrafast pulsed lasers. Similar to a snapshot camera, by interacting with a system on a timescale comparable with its dynamics, one gains access to its underlying temporal nature. With pulse durations now commonly in the few-femtoseconds (10^{-15} s) or even attoseconds (10^{-18} s), the motion of electrons within atoms is within reach. As such, problems involving these pulses interacting with atoms are sufficiently fundamental that experiments provide unprecedented tests of the theory at the heart of quantum mechanics. In this work we consider several such problems and compute experimental observables by means of methods based on the solution of the time-dependent Schrödinger equation. Namely; we consider the attoclock (Chapter 2), reconstruction of attosecond beating by interference of two-photon transitions (Chapter 3), high harmonic generation (Chapter 4), and the state-resolved acceleration of neutrals (Chapter 5). Problem specific motivation and background for the work we have conducted can be found immediately following each respective chapter heading.

1.2 Pulse description

Our description of the laser pulse is as an external freely propagating (zero scalar potential) electromagnetic wave of electric field $\boldsymbol{E}$, and magnetic field $\boldsymbol{B}$, via the

vector potential $\boldsymbol{A}$, such that

$$\boldsymbol{B} = \boldsymbol{\nabla} \times \boldsymbol{A} \tag{1.1}$$

$$\boldsymbol{E} = -\frac{\partial \boldsymbol{A}}{\partial t} \, . \tag{1.2}$$

1.2.1 Dipole approximation

In the 'dipole' or 'long wavelength' approximation we assume the wavelength of the electromagnetic oscillation is much larger that the physical dimensions of our system of interest. Equivalently we say that the field is uniform in space across our system such that $\boldsymbol{A}(\boldsymbol{r}, t) \to \boldsymbol{A}(t)$. Dropping this spatial dependence sets the curl of $\boldsymbol{A}$ to be zero and accordingly the same for the magnetic field $\boldsymbol{B}$.

The shortest wavelengths typically encountered in strong field problems are of the order of 100's of nanometres while the physical dimensions are on the scale of Bohr radii (~ 0.053 nm). Accordingly the dipole approximation is commonly used in such problems to the point where it often does not receive explicit mention. An exceptional problem for which we must go beyond this approximation is discussed in Chapter 5.

1.2.2 Explicit form

Unless otherwise stated, the form of the vector potential used to describe the pulse is the following

$$\boldsymbol{A}(t) = \frac{A_0 f(t)}{\sqrt{1+\epsilon^2}} \left[\cos(\omega t + \phi)\hat{\boldsymbol{x}} + \epsilon \sin(\omega t + \phi)\hat{\boldsymbol{y}}\right] \, . \tag{1.3}$$

In (1.3) A_0 is the amplitude, $f(t)$ is an envelope function (maximal for $t = 0$), ϵ is the ellipticity, ω is the frequency, and ϕ is the carrier envelope phase (CEP). This form relates straightforwardly to the peak intensity as (see Appendix A.1)

$$I = (\omega A_0)^2 = E_0^2 \, . \tag{1.4}$$

The two commonly used envelope functions are:

Sinusoidal

$$f(t) = \begin{cases} \left[\cos\left(\frac{\omega t}{2N}\right)\right]^n & -N\pi/\omega \leq \; t \; \leq N\pi/\omega \\ 0 & \text{elsewhere} \end{cases} \tag{1.5}$$

Here N determines the number of cycles and n the steepness of the falloff. The advantage of this form is that it has a natural well defined point from which the

pulse is both differentiable and zero.

Gaussian

$$f(t) = \begin{cases} \exp\left\{-\alpha t^2\right\} & |t| \leq t_1 \\ \exp\left\{-\alpha\left(t_1 + \frac{2}{\pi}(t_2 - t_1)\tan\left(\frac{\pi}{2}\frac{|t|-t_1}{t_2-t_1}\right)\right)^2\right\} & t_1 < |t| \leq t_2 \\ 0 & t_2 < |t| \end{cases} \tag{1.6}$$

Here t_1 and t_2 are positive times which determine the 'soft' and 'hard' cutoffs of the raw Gaussian. Such modification is necessary as a Gaussian function is only zero in the infinite limit and to ensure where the hard zero is chosen is reached smoothly. The parameter α determines the steepness of the envelope and is related to the full-width-half-maximum w (FWHM) of the intensity as the limit of the convergent sequence (see Appendix A.2)

$$\alpha = \lim_{n\to\infty} \alpha_n, \qquad \alpha_{n+1} = \frac{2}{w^2}\left[\ln 2 + \ln(1 + (w\alpha_n/\omega)^2)\right] \tag{1.7}$$

$$\alpha_0 = \frac{2\ln 2}{w^2}\,. \tag{1.8}$$

For sufficiently long pulses for which the time derivative of the envelope can be neglected we simply have

$$\alpha = \frac{2\ln 2}{w^2}\,. \tag{1.9}$$

Gaussian pulses are thought to better approximate those produced in experiment.

1.2.3 Keldysh parameter

The Keldysh parameter [1]

$$\gamma = \frac{\omega\sqrt{2I_p}}{E_0} = 4\pi\frac{\tau_{\text{tunnelling}}}{\tau_{\text{field}}}\,; \qquad \tau_{\text{field}} = \frac{2\pi}{\omega}\,,\ \ \tau_{\text{tunnelling}} = \frac{I_p/E_0}{\sqrt{2I_p}}\,, \tag{1.10}$$

is an often encountered quantity when considering laser-atom interactions. It can be thought of as a ratio between the time for a classical particle to transmit through the distorted potential barrier of the atom (field-free ionisation energy I_p) exposed to a laser field and the oscillation period of the field itself. For $\gamma \ll 1$ the oscillation of the field is slow relative to the potential tunnel ionisation process and thus the latter is expected to dominate. Such a scenario is accordingly said to be in the tunnelling regime. Conversely for $\gamma \gg 1$ and multiphoton ionisation/regime.

The Keldysh parameter can also be interpreted as a ratio of the ionisation po-

tential and a quantity known as the ponderomotive energy for an electron

$$\gamma^2 = \frac{I_p}{2U_p} \, . \tag{1.11}$$

This quantity is the cycle averaged kinetic energy for a free particle in a sinusoidal electric field of amplitude E_0 and frequency ω. For a particle of charge q and mass m it is given by

$$U_p = \frac{q^2 E_0^2}{4m\omega^2} \, . \tag{1.12}$$

1.3 Solution method

The time-dependent Schrödinger equation describes exactly the evolution of a non-relativistic system

$$i\frac{\partial}{\partial t}|\Psi\rangle = \hat{H}|\Psi\rangle \, . \tag{1.13}$$

It is this equation that we seek to solve within the single-active-electron approximation. The remainder of this section is dedicated to the three distinctive features of our approach

- The propagator is 'split' into several parts via a Peaceman-Rachford based formulation. Doing so avoids the need for matrix inversion in favour of tridiagonal algorithms and allows for greater parallel computation.

- A rotating coordinate frame is used such that the vector potential is always aligned with the local z-axis and corresponding angular momentum projection. This provides us with the familiar and desirable conservation rule of $\Delta m = 0$ even when departing from linear polarisation at the cost of performing small angle rotations for each timestep.

- Spatial derivatives are of the form $\boldsymbol{\nabla}^{(1,2)} = \mathbf{M}_{1,2}^{-1}\boldsymbol{\Delta}_{1,2}$ where $\mathbf{M}$ and $\boldsymbol{\Delta}$ are tridiagonal matrices i.e. only involve nearest neighbour terms. In such a form for a uniform grid of spacing h yields derivatives accurate to $O(h^4)$ at the cost of no longer being strictly anti-Hermitian or Hermitian for first $^{(1)}$ and second $^{(2)}$ orders respectively.

1.3.1 Gauge choice

The Hamiltonian describing a particle of mass m and charge q interacting with our laser field in the presence of a central potential $V(\boldsymbol{r})$ written in the so-called velocity

gauge [2, 3] is

$$\hat{H}^v = \frac{1}{2m}(\hat{\boldsymbol{p}} - q\boldsymbol{A}(t))^2 + V(\boldsymbol{r}) \; . \tag{1.14}$$

Here $\hat{\boldsymbol{p}} = -i\boldsymbol{\nabla}_{\boldsymbol{r}}$ is the momentum operator for said particle. Applying the unitary transformation

$$G^v = \exp(-iq\boldsymbol{r} \cdot \boldsymbol{A}(t)) \tag{1.15}$$

such that $|\Psi\rangle \to G|\Psi\rangle$ yields the equivalent expression in the length gauge

$$\hat{H}^l = \frac{1}{2m}\hat{\boldsymbol{p}}^2 - q\boldsymbol{r}\cdot\boldsymbol{E}(t) + V(\boldsymbol{r}) \; . \tag{1.16}$$

Applying instead the following Kramers-Henneberger transformation [4]

$$G^a = \exp\left(-i\boldsymbol{\alpha}(t) \cdot \hat{\boldsymbol{p}}\right) \tag{1.17}$$

$$\boldsymbol{\alpha}(t) = -\frac{q}{m}\int_{-\infty}^{t} \boldsymbol{A}(t')\mathrm{d}t' \tag{1.18}$$

yields the acceleration gauge / frame

$$\hat{H}^a = \frac{1}{2m}(\hat{\boldsymbol{p}}^2 + q^2\boldsymbol{A}^2(t)) + V(\boldsymbol{r} + \boldsymbol{\alpha}(t)) \; . \tag{1.19}$$

This form constitutes a shift of coordinates to that which follows the position of the particle under the influence of the pulse alone. Accordingly, for this formulation the Coulomb potential is moving in time.

Our numerical approach [5, 6] is based on the velocity gauge. The reasoning behind this is that for the length gauge expression the presence of the $\boldsymbol{r}\cdot\boldsymbol{E}(t)$ term is prone to precision loss when describing ionisation ($\boldsymbol{r} \to \infty$), while the consequences of having a moving Coulomb field for the acceleration form are more costly than any benefit gained. Nonetheless do note that our choice is not universal and in different contexts others may be made, a particularly interesting example of which being the mixed gauge choice in [7].

1.3.2 Propagator on a grid

The solution method is said to be 'on-the-grid' as opposed to using time-dependent basis functions. In such, the wavefunction is defined on a discrete radial grid at a given time t, and a propagator is calculated such that for a sufficiently small timestep $|\Psi(t + \delta t)\rangle \approx \hat{U}(t + \delta t, t)|\Psi(t)\rangle$ to any desired precision. Accordingly the substantive part of such an approach is in the construction of this propagator.

Recall that the equation we wish to solve is of the form [8]

$$i\frac{\partial}{\partial t}|\Psi\rangle = \hat{H}|\Psi\rangle \tag{1.20}$$

$$\implies |\Psi(t+\delta t)\rangle = \exp\left(-i\hat{H}\delta t\right)|\Psi(t)\rangle \tag{1.21}$$

$$\implies \hat{U}(t+\delta t, t) = \exp\left(-i\hat{H}\delta t\right) . \tag{1.22}$$

As such, the simplest approximation for the propagator is obtained by taking the first two terms (constant and linear) in the expansion of the matrix exponential

$$\hat{U}^{\text{Eul}}_{\text{fwd}}(t+\delta t, t) = \hat{1} - i\hat{H}\delta t \, , \tag{1.23}$$

known as the forward Euler method. Similarly, we have the backward Euler

$$\hat{U}^{\text{Eul}}_{\text{bak}}(t+\delta t, t) = \left(\hat{1} + i\hat{H}\delta t\right)^{-1} . \tag{1.24}$$

The Crank-Nicolson method [9]

$$\hat{U}^{\text{CN}}(t+\delta t, t) = \left(\hat{1} + i\hat{H}\frac{\delta t}{2}\right)^{-1}\left(\hat{1} - i\hat{H}\frac{\delta t}{2}\right) , \tag{1.25}$$

improves on the above by approximating instead the matrix exponential to quadratic order. This is a central difference, or the trapezoidal rule, an approximation combining both the forward and backward Euler steps for $t + \delta t/2$. It is also worthy of note that the resulting operator from this combination is unitary.

For the Crank-Nicolson method, the computationally limiting factor is the involved matrix inversion. However, in several cases (e.g. diffusion), properties of the Hamiltonian may be exploited such that it may be instead solved using tridiagonal matrices. To make full use of such properties we turn to the iterative methods known as Peaceman-Rachford [10, 11]. In which we consider

$$\hat{H} = \hat{H}_1 + \hat{H}_2 \tag{1.26}$$

$$\implies \hat{U}(t+\delta t, t) = \exp\left(-i(\hat{H}_1 + \hat{H}_2)\delta t\right) , \tag{1.27}$$

and make the approximation

$$\begin{aligned}\hat{U}^{\text{PR}}(t+\delta t, t) = &\left(\hat{1} + i\hat{H}_1\frac{\delta t}{2}\right)^{-1}\left(\hat{1} + i\hat{H}_2\frac{\delta t}{2}\right)^{-1} \\ &\times \left(\hat{1} - i\hat{H}_2\frac{\delta t}{2}\right)\left(\hat{1} - i\hat{H}_1\frac{\delta t}{2}\right) .\end{aligned} \tag{1.28}$$

Doing so allows us to instead of finding the matrix inverse of our Hamiltonian in aggregate, to treat its summed components separately via tridiagonal methods in parallel.

Note that while the above discussion in the strictest sense only applies for a time-

independent Hamiltonian, the extension of Crank-Nicolson for time dependence is

$$\hat{U}^{\mathrm{CN}}(t+\delta t,t)=\left(\hat{1}+i\hat{H}(t+\delta t)\frac{\delta t}{2}\right)^{-1}\left(\hat{1}-i\hat{H}(t)\frac{\delta t}{2}\right)\ , \tag{1.29}$$

and accordingly for Peaceman-Rachford

$$\begin{aligned}\hat{U}^{\mathrm{PR}}(t+\delta t,t)=&\left(\hat{1}+i\hat{H}_1(t+\delta t)\frac{\delta t}{2}\right)^{-1}\left(\hat{1}+i\hat{H}_2(t+\delta t)\frac{\delta t}{2}\right)^{-1}\\&\times\left(\hat{1}-i\hat{H}_2(t)\frac{\delta t}{2}\right)\left(\hat{1}-i\hat{H}_1(t)\frac{\delta t}{2}\right)\ .\end{aligned} \tag{1.30}$$

1.3.3 Rotating coordinate frame

For problems involving non-linear polarisation we choose to rotate our coordinate system such that $\boldsymbol{A}(t)$ is always aligned with the local z-axis and its corresponding angular momentum projection m. Doing so allows us to consider only a single momentum operator with the familiar property of $\Delta m=0$. Let us now examine the consequences of working in such a rotating coordinate system.

We define the rotation relative to the laboratory frame as the 3×3 unitary matrix $\mathbf{R}$ such that

$$\mathbf{R}(t)\cdot\boldsymbol{A}(t)=\begin{pmatrix}0\\0\\A_r(t)\end{pmatrix}\ , \tag{1.31}$$

where A_r is the radial magnitude of $\boldsymbol{A}$. Using $\mathbf{R}$ we relate our wavefunction in the lab frame and the local frame via

$$\Psi^{\mathrm{lab}}(\boldsymbol{r},t)=\sum_{LM}\frac{\Psi^{\mathrm{loc}}_{LM}(r,t)}{r}Y_{LM}\left(\mathbf{R}(t)\cdot\hat{\boldsymbol{r}}\right)\ , \tag{1.32}$$

where Y_{LM} is the spherical harmonic of total angular momentum $L\in[0,\infty)$ and z-projection $M\in[-L,L]$. Substituting this wavefunction into the lab frame TDSE with velocity gauge Hamiltonian (1.14) yields a Hamiltonian in the rotating local frame of the form

$$\hat{H}^{\mathrm{loc}}(t)=\hat{H}_{\mathrm{laser}}(t)+\hat{H}_{\mathrm{atom}}+\hat{H}_{\mathrm{rot}}(t)\ . \tag{1.33}$$

Here $\hat{H}_{\mathrm{atom}}$ is the familiar time-independent Hamiltonian

$$\hat{H}_{\mathrm{atom}}=\frac{1}{2}\hat{p}_r^2+V(r)+\frac{L(L+1)}{r^2}\ , \tag{1.34}$$

while $\hat{H}_{\mathrm{laser}}$ and $\hat{H}_{\mathrm{rot}}$ are the time-dependent laser and rotational couplings respectively (see Eqs. (18)-(25) of [6]).

Applying (1.30) to this derived Hamiltonian we have our 'H.G. Muller' propaga-

tor

$$\hat{U}_{\mathrm{HGM}}(t+\delta t,t) = \left(\hat{1}+i\hat{H}_{\mathrm{laser}}(t+\delta t)\frac{\delta t}{4}\right)^{-1}\left(\hat{1}+i\hat{H}_{\mathrm{atom}}\frac{\delta t}{4}\right)^{-1}\left(\hat{1}+i\hat{H}_{\mathrm{rot}}(t+\delta t)\frac{\delta t}{4}\right)^{-1} \times \left(\hat{1}-i\hat{H}_{\mathrm{rot}}(t)\frac{\delta t}{4}\right)\left(\hat{1}-i\hat{H}_{\mathrm{atom}}\frac{\delta t}{4}\right)\left(\hat{1}-i\hat{H}_{\mathrm{laser}}(t)\frac{\delta t}{4}\right) . \tag{1.35}$$

It is this propagator that is applied to our wavefunction at each timestep throughout the calculation. For details on the computation of each term please see Eqs. (37)-(47) and corresponding Sections 2.3.1-4 of [6].

1.3.4 Implicit spatial derivatives

Please note that the discussion in this section only considers the interior points of a uniformly spaced grid of spacing h. For the treatment of the grid edges or non-uniform spacing please see Section 2.2 of [6].

In the calculation of our propagator we unsurprisingly need first and second radial derivatives. While we could simply take use the following finite difference expressions accurate to $O(h^2)$

$$\nabla^{(1)} f \approx \frac{f_{n+1}-f_{n-1}}{2h} \tag{1.36}$$

$$\nabla^{(2)} f \approx \frac{f_{n+1}-2f_n+f_{n-1}}{h^2} , \tag{1.37}$$

the accuracy of such spatial derivatives strongly influences the quality of the calculation for a given radial grid. While expressions (1.36) and (1.37) are not sufficiently accurate, they are exceedingly simple to calculate due to being tridiagonal in matrix form, a property we wish to preserve. As such we look for approximations of the form

$$\boldsymbol{\nabla}^{(1,2)} \approx \mathbf{M}_{1,2}^{-1}\boldsymbol{\Delta}_{1,2} , \tag{1.38}$$

where $\mathbf{M}_{1,2}$ and $\boldsymbol{\Delta}_{1,2}$ are tridiagonal. Applying this to a function f defined on our radial grid, we have

$$\begin{aligned} &M_{n-1}f^{(1,2)}(r-h) + M_n f^{(1,2)}(r) + M_{n+1}f^{(1,2)}(r+h) \\ \approx\ &\Delta_{n-1}f(r-h) \quad + \Delta_n f(r) \quad + \Delta_{n+1}f(r+h) , \end{aligned} \tag{1.39}$$

for M_n and Δ_n being the non-edge diagonal elements of the matrices. We will additionally impose the constraint that $M_{n-1}+M_n+M_{n+1}=1$ to ensure the solution is unique and non-trivial. Expanding f around the point r in a Taylor

series we have

$$M_{n-1}\left(\sum_{m=0}^{\infty}\frac{f^{(m+1,2)}(r)}{m!}(-h)^m\right)+M_n f^{(1,2)}(r)+M_{n+1}\left(\sum_{m=0}^{\infty}\frac{f^{(m+1,2)}(r)}{m!}h^m\right)$$
$$\approx \Delta_{n-1}\left(\sum_{m=0}^{\infty}\frac{f^{(m)}(r)}{m!}(-h)^m\right)\quad+\Delta_n f(r)\quad+\Delta_{n+1}\left(\sum_{m=0}^{\infty}\frac{f^{(m)}(r)}{m!}h^m\right)\ . \tag{1.40}$$

With our previously mentioned constraint, we essentially have an equation in 5 unknowns and, accordingly, from equating derivatives of $f^{(m)}$ for $m \in 0,4$ we will completely define said unknowns. These equations are of the form

$$\frac{H(m-x)}{h^2}\left(M_{n-1}\frac{(-1)^{m-x}}{(m-x)!}+\delta_{x,m}M_n+M_{n+1}\frac{1}{(m-x)!}\right)$$
$$=\quad \Delta_{n-1}\frac{(-1)^m}{m!}\quad+\delta_{0,m}\Delta_n+\Delta_{n+1}\frac{1}{m!}\ , \tag{1.41}$$

for the approximation to $\boldsymbol{\nabla}^{(x)}$, $x \in 1,2$. Here $H(x)$ is the unit step function with $H(0)=1$, and $\delta_{i,j}$ is the Kronecker delta. The explicit solutions are

$$\boldsymbol{\nabla}^{(1)} \approx \quad \{M_{n-1},M_n,M_{n+1}\}=\frac{1}{6}\{1,4,1\}\ , \qquad \{\Delta_{n-1},\Delta_n,\Delta_{n+1}\}=\frac{1}{2h}\{-1,0,1\} \tag{1.42}$$

$$\boldsymbol{\nabla}^{(2)} \approx \quad \{M_{n-1},M_n,M_{n+1}\}=\frac{1}{12}\{1,10,1\}\ , \qquad \{\Delta_{n-1},\Delta_n,\Delta_{n+1}\}=\frac{1}{h^2}\{1,-2,1\}\ . \tag{1.43}$$

By our construction we will have an equality up to terms in $f^{(4)}$ which corresponds to errors of order $O(h^4)$ and $O(h^3)$ for $\boldsymbol{\nabla}^{(1)}$ and $\boldsymbol{\nabla}^{(2)}$, respectively. Upon inspection, however, we find that the second derivative solution also satisfies (1.41) for $m=5$. Accordingly both operators have errors $O(h^4)$.

An important consequence of this approximate construction, however, is that the operator $\mathbf{M}_1^{-1}\boldsymbol{\Delta}_1$ is not strictly anti-Hermitian as $(\boldsymbol{\nabla}^{(1)})^\dagger = -\boldsymbol{\nabla}^{(1)}$. In fact, similarly for non-uniform radial grids, the approximation $\mathbf{M}_2^{-1}\boldsymbol{\Delta}_2$ is no longer Hermitian [6]. Accordingly, our Hamiltonian itself is only approximately Hermitian and, as such, requires special treatment. For a non-Hermitian matrix $\mathbf{H}$ we must consider both left and right eigenvectors of the form

$$\mathbf{H}\boldsymbol{R}=\epsilon\boldsymbol{R} \tag{1.44}$$
$$\boldsymbol{L}^\dagger\mathbf{H}=\epsilon\boldsymbol{L}^\dagger \tag{1.45}$$

as $\boldsymbol{L} \neq \boldsymbol{R}$. Equivalently we must consider both left and right wavefunctions which

satisfy

$$\begin{aligned} i\frac{\partial}{\partial t}|\Psi_R\rangle &= \quad \hat{H}\ |\Psi_R\rangle \\ i\frac{\partial}{\partial t}|\Psi_L\rangle &= -\hat{H}^\dagger|\Psi_L\rangle\ . \end{aligned} \tag{1.46}$$

From which we observe that the two functions may be propagated in an identical fashion simply by replacing $\hat{H} \to -\hat{H}^\dagger$. Under this non-Hermitian formulation the expectation value of an observable O is

$$\langle O\rangle = \langle\Psi_L|O|\Psi_R\rangle\ . \tag{1.47}$$

It is truly worthily of note that the accuracy and efficiency saving of these operators is such that it supersedes the cost of propagating a second wavefunction. Additionally it can be shown that there exists a Hermitian Hamiltonian equivalent, that while impractical to repeatedly evaluate, guarantees that propagation is possible without an exponentially growing norm [6].

1.3.5 Photoelectron spectra extraction

In Chapters 2 and 3 the primary observable of interest is the distribution of photoelectron momenta, or spectra, resulting from the given process. To do so we employ the surface flux methods of [12, 13] for which their basis is detailed in the following.

Assuming we have the wavefunctions $|\Psi\rangle$ which are solutions for Hamiltonian $\hat{H}$, let us consider instead the solutions $|X\rangle$ of $\hat{H}_A$ which is comprised of only the asymptotic in r parts of $\hat{H}$. Accordingly the $|X\rangle$ are the asymptotic states of $|\Psi\rangle$ such that the amplitude given by

$$a(t)_X = \langle X(t)|\Psi(t)\rangle \tag{1.48}$$

for sufficiently large t is the ionisation probability to $|X(t)\rangle$. However, at such large t, it is numerically impractical to maintain the entirety of the wavefunction within a finite radial box. As such, we turn to surface flux methods.

Let us say at large asymptotic time t the overlap (1.48) is dominated far from the origin, beyond some radius R. Therefore we can write

$$a(T)_X = \int \mathrm{d}^3 r X^*(\boldsymbol{r}, T)\hat{\Theta}_R\Psi(\boldsymbol{r}, T)\ , \tag{1.49}$$

where $\hat{\Theta}_R$ is the operator form of the positive spherical step function with the definition on the boundary $\hat{\Theta}_R|R\rangle = |R\rangle$. Similarly, let our R be such that at time 0 the entire wavefunction is contained within $r < R$, hence

$$a(0)_X = \int \mathrm{d}^3 r X^*(\boldsymbol{r}, 0)\hat{\Theta}_R\Psi(\boldsymbol{r}, 0) = 0\ . \tag{1.50}$$

Accordingly, we can write

$$\begin{aligned} a(T) &= a(T) - a(0) \\ &= \int_0^T \mathrm{d}t \, \frac{\partial}{\partial t} \int \mathrm{d}^3 r X^*(\boldsymbol{r}, t) \hat{\Theta}_R \Psi(\boldsymbol{r}, t) \\ &= \int_0^T \mathrm{d}t \, i \int \mathrm{d}^3 r X^*(\boldsymbol{r}, t) \left(\hat{H}_A \hat{\Theta}_R - \hat{\Theta}_R \hat{H} \right) \Psi(\boldsymbol{r}, t) \\ &= \int_0^T \mathrm{d}t \, i \int \mathrm{d}^3 r X^*(\boldsymbol{r}, t) \left[\hat{H}_A, \hat{\Theta}_R \right] \Psi(\boldsymbol{r}, t) \, , \end{aligned} \tag{1.51}$$

where $\left[\hat{H}_A, \hat{\Theta}_R\right]$ is their commutator. This commutator is only non-zero on the boundary $r = R$ as it is here where it does not trivially commute with radial derivative operators. We will see this explicitly below. Accordingly, we write (1.51) as the surface integral

$$a(T) = \int_0^T \mathrm{d}t \, i \int_{r=R} \mathrm{d}\Omega \, X^*(\boldsymbol{r}, t) \left[\hat{H}_A, \hat{\Theta}_R \right] \Psi(\boldsymbol{r}, t) \, . \tag{1.52}$$

Infinite time correction

However, for (1.52) to be the asymptotic value with respect to time, we require the entire of the wavefunction to have passed through said surface, which requires significant propagation beyond the end of the pulse. To overcome this, we consider an infinite time correction to (1.52) given that $\boldsymbol{A}(t > T) = \boldsymbol{0}$. Beyond this point the Hamiltonian is now time independent and consequently the wavefunction simply is given by

$$|\Psi(t)\rangle = e^{-iE(t-T)} |\Psi(T)\rangle \qquad t > T \, , \tag{1.53}$$

where the total energy E satisfies $\hat{H}(t > T)|\Psi(t)\rangle = E|\Psi(t)\rangle$. Similarly, we can write the time dependence of $\langle X(t)|$ as

$$\langle X(t)| = \langle X(T)| e^{i(\epsilon + i0)(t-T)} \, , \tag{1.54}$$

where ϵ is the energy of the state. Here an infinitesimal imaginary component $i0 = \lim_{x \to 0} ix$ is added to ensure outgoing spherical boundary conditions ($\to 0$) at infinity. Accordingly, the extension of (1.52) becomes

$$\begin{aligned} a(\infty) - a(T) &= \int_T^\infty \mathrm{d}t \, i e^{i(\epsilon + i0 - E)(t-T)} \int_{r=R} \mathrm{d}\Omega \, X^*(\boldsymbol{r}, T) \left[\hat{H}_A, \hat{\Theta}_R \right] \Psi(\boldsymbol{r}, T) \\ &= \frac{1}{\epsilon + i0 - E} \int_{r=R} \mathrm{d}\Omega \, X^*(\boldsymbol{r}, T) \left[\hat{H}_A, \hat{\Theta}_R \right] \Psi(\boldsymbol{r}, T) \, . \end{aligned} \tag{1.55}$$

Asymptotic states

We now have our amplitudes given by (1.52) and (1.55). What remains is our choice of the asymptotic Hamiltonian $\hat{H}_A$ of which we will consider the two: Volkov and

Coulomb,

$$\hat{H}_V = \frac{1}{2}(\hat{\boldsymbol{p}} + \boldsymbol{A}(t))^2 \tag{1.56}$$

$$\hat{H}_C = \frac{1}{2}\hat{\boldsymbol{p}}^2 + V(r) \, . \tag{1.57}$$

The Volkov states have the advantage of being solutions in the presence of the external field allowing the projection to be calculated while the pulse is present via (1.52). After the pulse the Volkov states are simply plane waves. A consequence, however, is that R must be sufficiently large such that the atomic potential may be neglected. Contrastingly, the Coulomb waves solutions of its corresponding Hamiltonian are exact regardless of the R chosen yet require the pulse to be over. As such, we require T sufficiently large such that the entirety of the wavefunction remains within the volume $r < R$, or equivalently the right hand side of Eq. (1.52) is equal to zero, effectively losing any efficiency gained from this surface formulation. Nonetheless, it provides a useful check against the Volkov form when both are numerically viable.

Let us finally evaluate the explicit forms of Eqs. (1.52) and (1.55) by computing the commutator with the step function. For the Volkov Hamiltonian

$$\begin{aligned}
\left[\hat{H}_V, \hat{\Theta}_R\right] &= -\frac{1}{2}\left[\nabla\cdot\nabla, \hat{\Theta}_R\right] + i\left[\boldsymbol{A}\cdot\nabla, \hat{\Theta}_R\right] \\
&= -\frac{1}{2}\left(\nabla\cdot\left[\nabla, \hat{\Theta}_R\right] + \left[\nabla\cdot, \hat{\Theta}_R\right]\nabla\right) + i\boldsymbol{A}\cdot\left[\nabla, \hat{\Theta}_R\right] \\
&= -\frac{1}{2}\left(\frac{1}{r^2}\partial_r\left(r^2\delta(r-R)\right) + \delta(r-R)\partial_r\right) + iA_r\delta(r-R) \, ,
\end{aligned} \tag{1.58}$$

where $\delta(r-R)$ is the Dirac delta function and A_r is the radial magnitude of $\boldsymbol{A}$. Substituting this result into Eq. (1.52) and conjugating to make the operator $i\partial_r/r^2$ act to the left, we have

$$a(T) = \int_0^T \mathrm{d}t \int_{r=R} \mathrm{d}\Omega \left(\frac{i}{2}\left[\partial_r, X^*(\boldsymbol{r},t)\right] - A_r X^*(\boldsymbol{r},t)\right)\Psi(\boldsymbol{r},t) \, . \tag{1.59}$$

The commutator for the Coulomb Hamiltonian is identical to (1.58) setting $A_r = 0$ but, as mentioned above, Eq. (1.59) is thus invalid for $t < T$ where $\boldsymbol{A}(t)$ is non-zero. Accordingly, however, for Eq. (1.55) defined such that $\boldsymbol{A}(t) = \boldsymbol{0}$ for $t > T$ both Hamiltonians yield

$$a(\infty) - a(T) = \frac{1}{\epsilon + i0 - E}\int_{r=R} \mathrm{d}\Omega \, \frac{1}{2}\left[\partial_r, X^*(\boldsymbol{r},T)\right]\Psi(\boldsymbol{r},T) \, . \tag{1.60}$$

Chapter 2

Attoclock

This chapter is based on the following publications:

> A. W. Bray, S. Eckart, and A. S. Kheifets, "Keldysh-Rutherford model for the attoclock," Phys. Rev. Lett. **121**, 123201 (2018).
>
> U. S. Sainadh, H. Xu, X. Wang, A. Atia-Tul-Noor, W. C. Wallace, N. Douguet, A. Bray, I. Ivanov, K. Bartschat, A. Kheifets, R. T. Sang, and I. V. Litvinyuk, "Attosecond angular streaking and tunnelling time in atomic hydrogen," Nature **568**, 75 (2019).
>
> A. W. Bray, "The attoclock and tunnelling time," J. Phys. Conf. Ser. (ICPEAC 2019), *Accepted*.

A quintessential example of a time resolved atomic physics problem is that known as the 'attoclock'. In such, the rotating electric field vector of a (near)-circularly polarised laser pulse applied to a target atom or molecule maps the timing of the resultant tunnel ionisation onto the photoelectron momentum. From the distribution of this momentum, a measurement of the 'tunnelling time' for the process is derived. However, despite a decade passing since the techniques inception [14], lack of consensus persists over its interpretation, in no small part due to the notion of tunnelling time itself.

First examined by MacColl [15] in 1932, the concept of a tunnelling time has received great attention and is the subject of a recent review [16]. The problem of a Gaussian wavepacket scattering from a rectangular finite potential barrier as examined by [15, 17] is illustrated in Figure 2.1. However, due to its somewhat arbitrary nature, in several different contexts a quantity using this moniker has been defined. Each of these definitions are mutually incomparable as they are fundamentally different methods of quantifying the underlying physical process. Hence the question is, does the attoclock contain any physics attributable to a tunnelling time, and if so, is it compatible with an existing definition or is yet of another form?

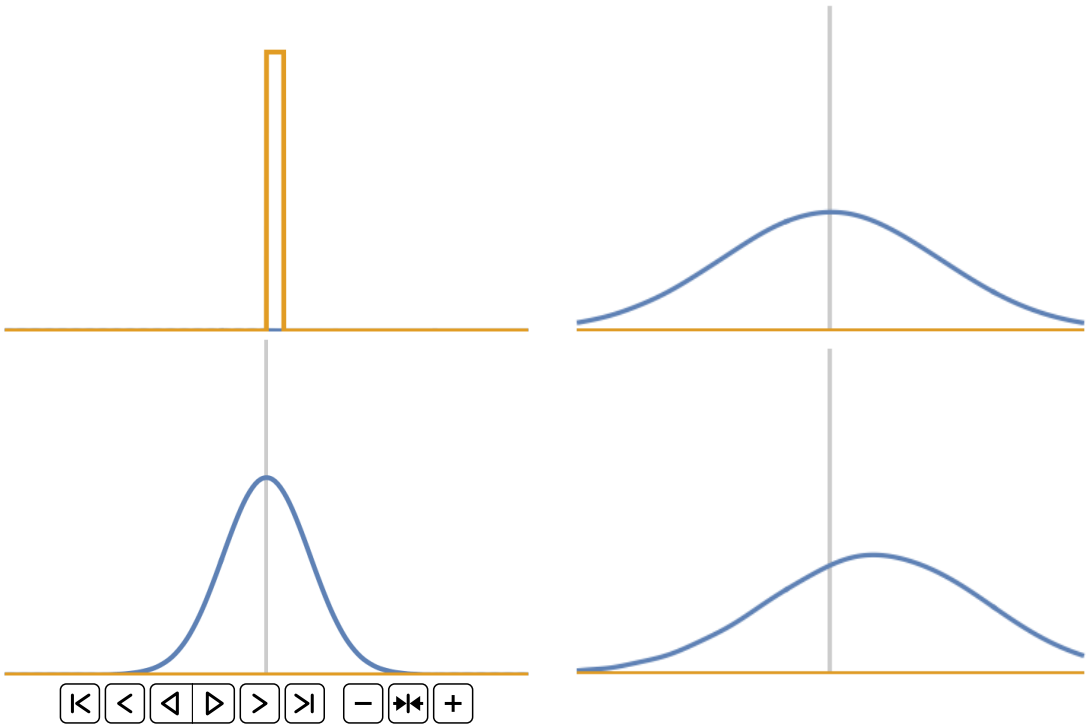

Figure 2.1: (Animation for javascript enabled PDF viewer, left to right stills in print) Animation: (Left column) Illustration of a Gaussian wavepacket tunnelling through a rectangular finite potential barrier as examined by [15, 17] in a stationary coordinate system (top) or one which follows the centre of an undisturbed packet (bottom). (Right column) A comparison between an undisturbed wavepacket (top) and that which is transmitted, scaled to be of equal magnitude (bottom). Stills: As for the (Left column) described above but only for the stationary coordinate system.

For an attoclock experiment to conclude an observation of tunnelling time, the rotation observed in the photoelectron momentum distribution must be unexplained by classical trajectories assuming instantaneous tunnelling. For the earliest reported attoclock measurements, this was not found to be the case [18, 19]. In stark contrast, the results of Landsman *et al.* [20] observed rotations far beyond what could be explained by such trajectories. However, to this date, the data remains unexplained by *ab initio* theory despite considerable effort [21, 22]. The remaining suggestion of tunnelling times in attoclock problems is from Camus *et al.* [23]. This work relies on the finding that the difference in rotations from two atomic targets is not well explained by trajectories both with instantaneous tunnelling and zero initial velocity.

On the theoretical side, using near single-cycle pulses, the nature of the rotation has been found to be of entirely Coulombic origin [24, 25]. To experimentally confirm this finding it has been suggested to examine negative ions [26]. Further evidence is provided via backpropagation [27] or through application of an additional linearly polarised field [28]. Most convincing, however, is the recent work of Sainadh *et al.* [29], which presents agreement between theory and experiment for an atomic

hydrogen target, and concludes that they see no rotations attributable to a delay in the tunnelling process.

The remainder of this chapter is dedicated to the physics behind the attoclock (Section 2.1) and the contributions to this problem that [29] and [25] constitute (Sections 2.2 and 2.3 respectively).

2.1 Physical mechanism

As mentioned above, an attoclock experiment makes use of the rotating electric field vector of a (near)-circularly polarized laser pulse applied to a target atom or molecule to map the timing of the resultant tunnel ionisation onto the photoelectron momentum. In this section, we wish to elucidate the physics by which this mapping is possible.

The problem is one of strong field ionisation and, accordingly, falls within the so-called tunnelling regime. Typical pulse parameters are 800 nm wavelengths, peak intensities around 1×10^{14} W/cm^2, and full-width-half-maximums in intensity of several femtoseconds. In this regime, we may think of the influence of our laser field as a modification to the atomic binding potential such that

$$V_{\text{tot}}(\boldsymbol{r}, t) = -1/r + \boldsymbol{E}(t) \cdot \boldsymbol{r} \ . \tag{2.1}$$

As the pulse progresses in time the V_{tot} potential 'tips over' and, for non-linear polarisation, rotates. This allows the initially bound electron to escape via tunnelling through the tipped-over barrier to energetically allowed regions. Figure 2.2 illustrates this process. The momentum distribution of these escaped electrons (e.g. Figure 2.3) is then contrasted against those of classical trajectories to determine if the tunnelling process involved any delay. The core of these comparisons rely on the mapping of the pulse vector potential at the moment of ionisation onto the photoelectron momenta which, in its simplest form, is

$$\boldsymbol{p}_{t\to\infty} = -\boldsymbol{A}(t_{\text{ion}}) \ . \tag{2.2}$$

The above expression is the result of integrating Newton's law from some moment of ionisation (t_{ion}) to infinity of the electron moving classically due to the electric field of the pulse. This can clearly be improved upon, most notably by the inclusion of the Coulomb force from the parent ion, but nonetheless captures the mechanism by which the timing of the electrons appearance in the continuum is imprinted onto its final momentum. The imprint manifests as a rotation of the resulting momentum distribution and, should the rotation be to an extent unexplainable by classical trajectories beginning at the peak electric field, the remaining angle is interpreted as the delay of the tunnelling process.

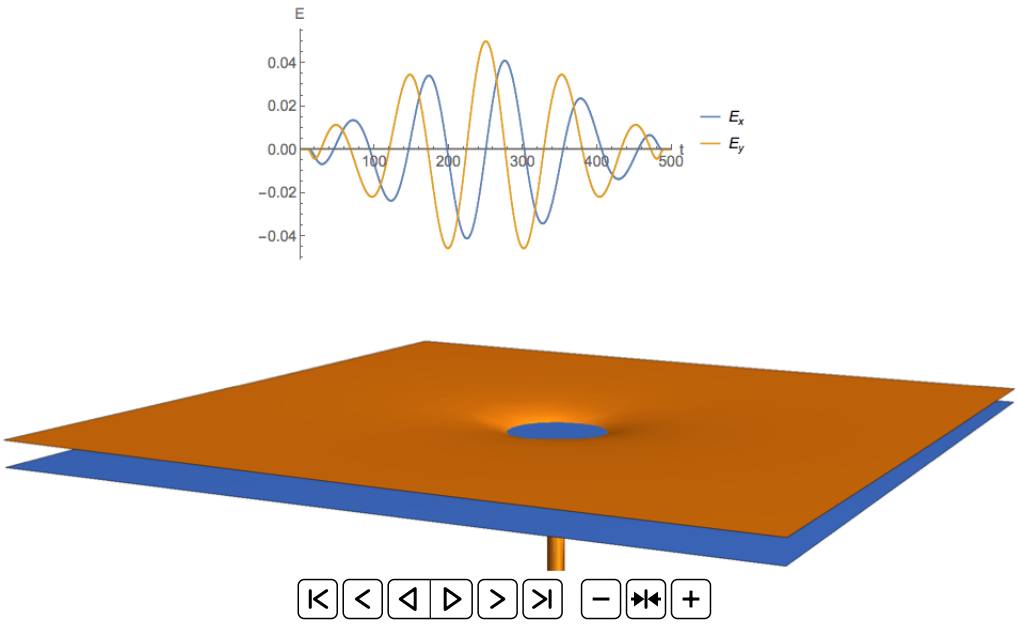

Figure 2.2: (Animation for javascript enabled PDF viewer, left to right stills in print) The distortion of the atomic potential as a function of time for a typical attoclock pulse (orange surface) vs the initial binding energy (blue plane). Where these two surfaces intersect the bound electron is able to adiabatically tunnel.

However, the comparison of the distribution of a fundamentally quantum mechanical process with classical trajectories is not straightforward. Firstly, the distribution needs to be characteristic of these trajectories. This is indeed the case for the near-single-cycle pulses (top row of Figure 2.3) that have been theoretically examined, as the resulting distributions have a well defined angle about which it is symmetric. In contrast, for few-femtosecond pulses, the distribution is complicated by above-threshold-ionisation (ATI) fringes from inter-cycle interference, a phenomena unexplainable by classical physics. Secondly, the boundary conditions appropriate for the trajectory are critical to its comparison, this being contingent on assumptions of the adiabaticity of the tunnelling process.

A further consideration pertinent to the observed attoclock distribution in Figure 2.3 is the carrier envelope phase or CEP (see Equation (1.3)). This is the phase of the underlying electric field profile of the pulse within its envelope. For short pulses with circular polarisation (top row), the peak field strength simply rotates in the plane with varying CEP and accordingly the same occurs for the resulting momentum distribution. However, for the few-femtosecond pulses with elliptical polarisation (bottom row), the direction of the peak field strength only changes subtly with variation of CEP. In fact, it is only the ellipticity that modulates the field strength significantly enough for the distribution to exhibit the characteristic two-lobes observed in experiment. Consequently, these ‘long pulse’ distributions are dependent on the precise CEP, and are accordingly averaged over for comparison.

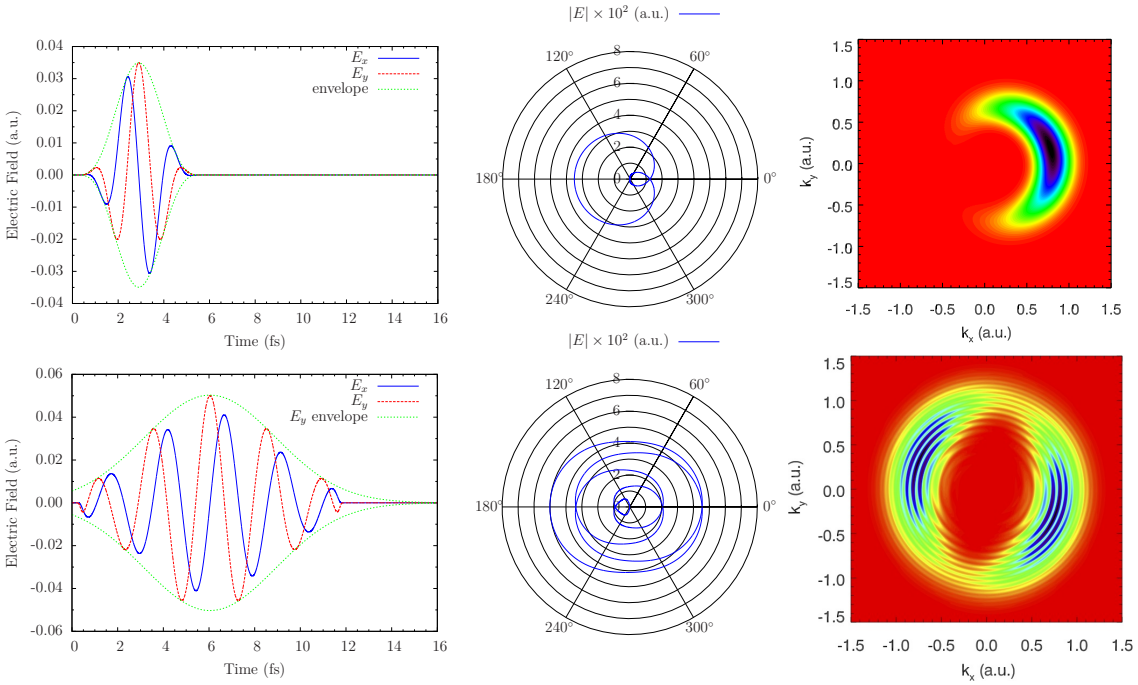

Figure 2.3: Example photoelectron spectra resulting from hydrogen for short (top row) and long (bottom row) pulses. Left column: electric field components of the pulse as a function of time. Centre column: electric field magnitude vs direction of vector-potential parametrically with time. Right column: the 3D-TDSE calculated spectra in the polarisation plane coloured linearly from red (min) to black (max). The short pulse is approximately 1.6 fs FWHM in intensity of peak 0.86×10^{14} W/cm^2, 800 nm, ellipticity 1.0, and anti-clockwise helicity. Its corresponding distributions assume CEP stability. The long pulse is approximately 6 fs FHWM in intensity of peak 1.5×10^{14} W/cm^2, 770 nm, ellipticity 0.85, and clockwise helicity. Its corresponding distributions are averaged over CEP.

2.2 Atomic hydrogen *ab initio* theory and experiment

Our work [29] constitutes the first demonstrated agreement between *ab inito* theory and experiment for the attoclock problem. By examining the simplest atomic target, hydrogen, we are able to have the highest confidence in our findings. In contrast, all previous works [14, 18–20, 23] have been performed on multi-electron noble gasses for which the TDSE based theoretical treatment involves potentially detrimental approximations. Particularly the persistent disagreement surrounding the helium experiment of [20] motivates our own, given the considerable effort made in aim of its resolution [21, 22, 30].

A pulse of approximately 6 fs FWHM at 770 nm and ellipticity 0.85 is applied to an atomic hydrogen target and the CEP averaged momentum distribution as a function of peak intensity is both measured in experiment and calculated. Additionally, we perform identical calculations with a Yukawa potential $V(r) = Ze^{-r/\lambda}/r$ with

$Z = 1.908$ and $\lambda = 1.0$. Doing so yields a contrasting distribution from a hydrogenic initial wavefunction of equal energy while exponentially screening the Coulomb potential. Two such contrasting distributions are given in the bottom row of Figure 2.4. Equivalent calculations involving short pulses (1.6 fs FWHM) are given in the top frame for comparison. These distributions are radially integrated and fitted with Gaussians to extract an angle which is then compared directly between theory and experiment in Figure 2.5.

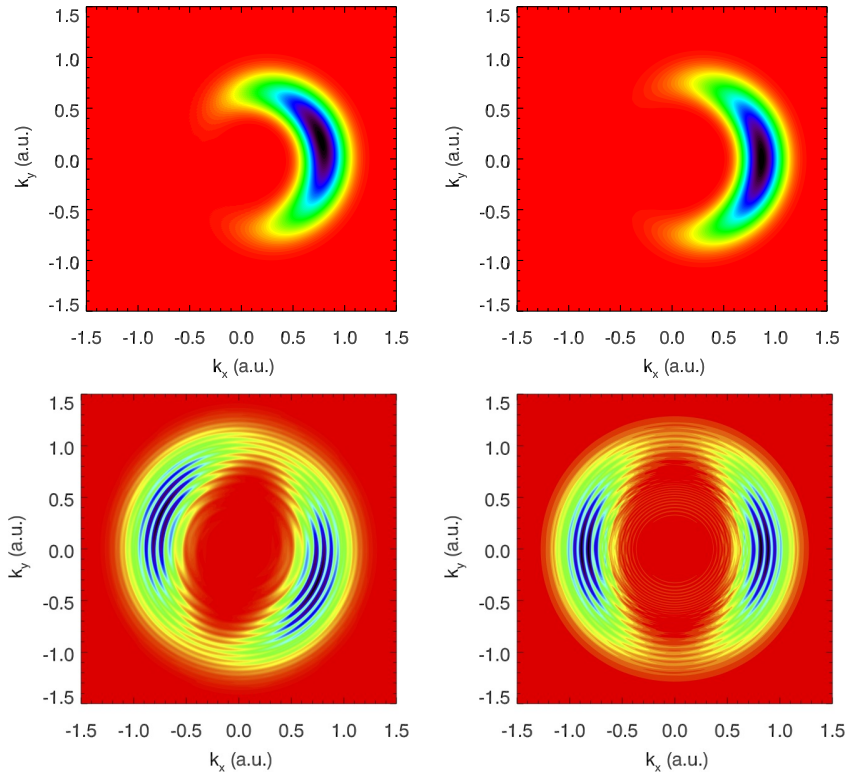

Figure 2.4: Left column: 3D-TDSE calculated photoelectron spectra from hydrogen for short (top) and long (bottom) pulses. The short pulse is approximately 1.6 fs FWHM in intensity of peak 0.86×10^{14} W/cm^2, 800 nm, ellipticity 1.0, and anti-clockwise helicity. Its corresponding distributions assume CEP stability. The long pulse is approximately 6 fs FWHM in intensity of peak 1.5×10^{14} W/cm^2, 770 nm, ellipticity 0.85, and clockwise helicity. Its corresponding distributions are averaged over CEP. Right column: As for left but from a Yukawa potential (screening parameter $\lambda = 1$) of hydrogenic binding energy. The colouration of probability is linear and normalised from red (min) to black (max).

As mentioned in Section 2.1 and illustrated in Figure 2.4, in general, for long pulses, the fringes resulting from inter-cycle interference each feature distinct rotations [31]. Consequently, the radial integration of a distribution consisting of several Gaussians of differing rotations is sensitive on their individual weighting. To overcome this, care was taken such that the same extraction method was applied directly to both theoretically calculated and experimentally observed spectra. In doing so, we find excellent agreement between the two. Amusingly, no such issue occurs for the strongly screened distribution as each fringe has a rotation of zero.

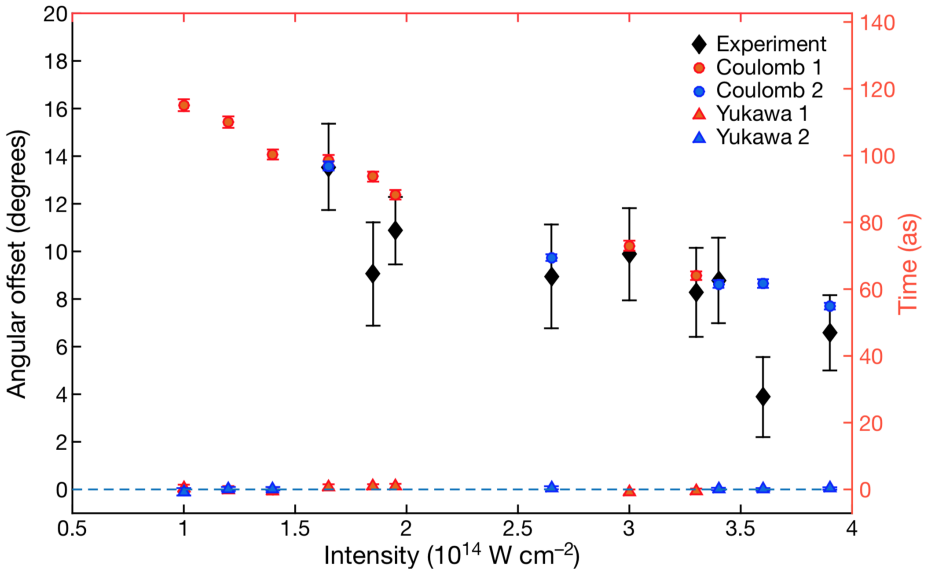

Figure 2.5: Experimental and theoretical attoclock rotations as a function of intensity [29]. The experimental observations (black diamonds with estimated experimental and fitting errors) are compared to *ab initio* 3D-TDSE simulations with Coulomb potentials provided by two independently developed computational methods marked as 1 and 2 (respectively orange and blue filled circles). To disentangle the effects of the Coulomb potential on the continuum electron, we also include the TDSE simulations for a Yukawa potential (orange and blue filled triangles representing calculations by the same two independent groups marked as 1 and 2). Numerical errors are comparable to, or less than, the symbol size. The horizontal dashed blue line is drawn at the zero offset angle. The same extraction procedure was used to determine the offset angles from experimental results and theoretical simulations for both Coulomb and Yukawa potentials. Our numerical experiment demonstrates that the observed angular offsets are entirely due to the photoelectron scattering by the long-range Coulomb potential of the ion.

After establishing consensus between the TDSE theory and observation we turn to the Yukawa screened potential. We find that identical calculations with this potential yield zero rotations within numerical accuracy across the entire range of intensities considered. This we take as strong indication of the observed rotations being entirely due to the Coulombic attraction to the ionised core which is being removed in the latter scenario. Nonetheless, to demonstrate this connection more directly, we next look to the idealised short pulse attoclock problem.

2.3 Short pulse theory

Having established the validity of our theoretical methods for physically realisable pulses, we turn to idealised short pulse attoclocks [25]. As discussed in Section 2.1, for such pulses non-zero rotations can be unambiguously attributed to a given distribution due to their perfect symmetry. Figure 2.6 presents the computed distributions for various Yukawa screening parameters λ with hydrogenic initial state energy. We

find that the rotation can be smoothly controlled by the level of screening between the hydrogenic case ($\lambda \to \infty$) and zero ($\lambda \to 0$). From this further suggestion that the cause of rotation is from the Coulombic force the electron experiences throughout its escape trajectory, we next look to formulate an appropriate classical scattering theory that we may contrast against our TDSE calculated dependency.

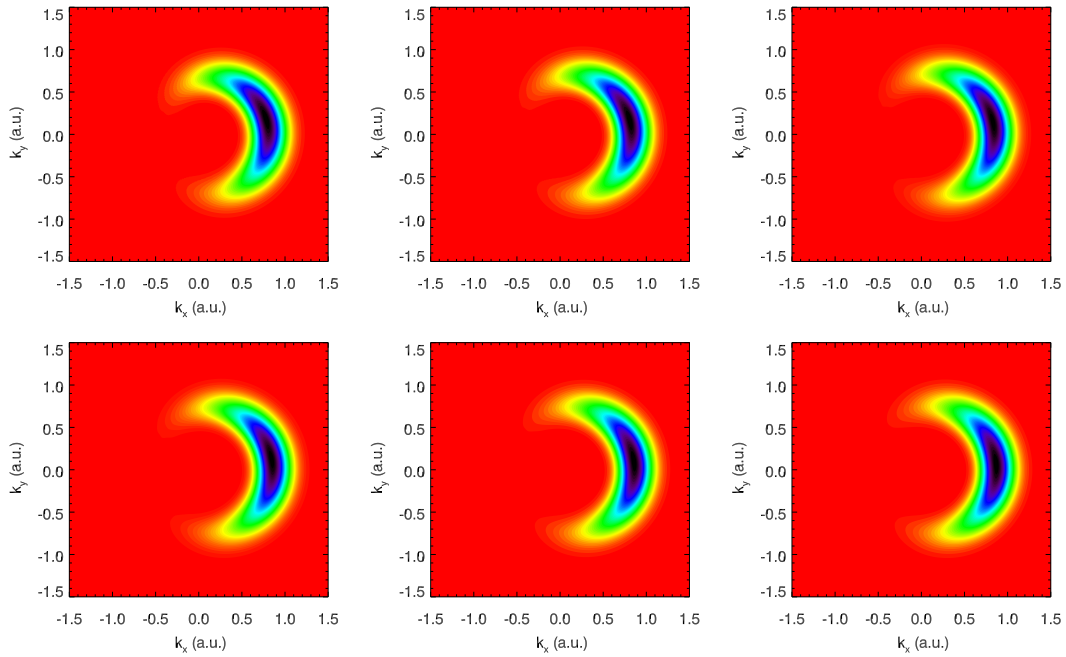

Figure 2.6: 3D-TDSE calculated photoelectron spectra from Yukawa potentials of varying screening and equal initial state energy of 0.5 a.u. The pulse is approximately 1.6 fs FWHM in intensity of peak 0.86×10^{14} W/cm^2, 800 nm, ellipticity 1.0, and anti-clockwise helicity. The explicit screening values from left to right are $\lambda \in \{\infty, 40, 20, 13, 10, 7\}$ and $Z \in \{1.0, 1.0249, 1.0495, 1.0739, 1.0980, 1.1458\}$.

2.3.1 Keldysh-Rutherford model

As opposed to the commonly employed 'strong field approximation' for the attoclock [1, 32–35] in which the effect of the Coulombic interaction is neglected, we instead look to neglect the effect of the pulse post ionisation. By doing so the resulting trajectory becomes that of Rutherford scattering or its equivalent for a screened potential. For short pulses at low intensity, we expect this approximation to be reasonable, and by comparison in this regime provide significant insight into the physics behind the attoclock observable.

The scattering angle for a charged particle in a central $1/r$ potential is given by the Rutherford formula [36]

$$\theta = 2\cot^{-1}\left(\frac{\rho v_\infty^2}{Z}\right) , \tag{2.3}$$

where ρ is the impact parameter and v_∞ is the asymptotic velocity. In a more general case of a screened potential of the form $V(r) = -Z/r \exp(-r/\lambda)$, the offset angle is given by a modified expression [37]

$$\theta = 2\cot^{-1}\left(\frac{\rho v_\infty^2}{Z\exp(-1/z_0)}\right) + \frac{2\rho}{\lambda}\int_0^{z_0}\frac{1}{\sqrt{y_0(z)}} - \frac{1}{\sqrt{y(z)}}\,\mathrm{d}z\,, \tag{2.4}$$

where z_0 is the root of

$$y(z) = 1 - (\rho/\lambda)^2 z^2 - (d/\lambda) z \exp(-1/z), \tag{2.5}$$

and

$$y_0(z) = 1 - (\rho/\lambda)^2 z^2 - (d/\lambda) z \exp(-1/z_0)\,. \tag{2.6}$$

Here $d = 2Z/(mv_\infty^2)$ is the so-called collision diameter. If the last term in the RHS of $y(z)$ can be neglected, Eq. (2.4) simply becomes

$$\theta = 2\cot^{-1}\left(\frac{\rho v_\infty^2}{Z\exp(-\rho/\lambda)}\right)\,. \tag{2.7}$$

The trajectory for an attractive potential is depicted in the left frame of Figure 2.7 along with the instantaneous electric and vector potential at the moment of ionisation and equivalent attoclock angle $\theta_A = \theta/2$.

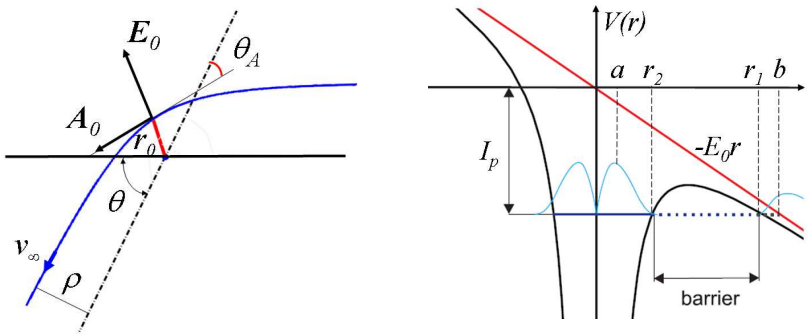

Figure 2.7: Left: The classical scattering trajectory of a particle in a central attractive potential. The scattering angle θ is defined by the impact parameter ρ and the asymptotic velocity v_∞. The tunnel ionized electron enters this trajectory at the point of the closest approach r_0 driven by the peak electric field E_0 and arriving to the detector at the angle θ_A relative to the vector potential A_0. Right: The Coulomb potential is tipped by the light field. A finite width potential barrier is created, through which the electron wave packet leaks out. I_p refers to the binding energy of the electron in an unperturbed atomic system. See text for further symbol definitions.

To evaluate Eq. (2.3) (or (2.4)) we simply need a ρ and v_∞. Firstly, we consider the distance of closest approach r_0 from the maximally 'tipped-over' potential depicted in the right frame of Figure 2.7. The largest solution (r_1) of

$$Z/r + E_0 r = I_p \quad , \quad r_{1,2} = b/2 \pm \sqrt{b^2/4 - ab} \; , \tag{2.8}$$

where $b = I_p/E_0$ is the Keldysh tunnel width and $a = Z/I_p$ gives the distance of closest approach assuming adiabatic tunnelling $r_0 = r_1$. Instead, however, we will simply take $r_0 \approx b$, and further that the impact parameter $\rho \approx r_0$. To a similarly approximate level, we will take $v_\infty \approx A_0$ obtained directly from Eq. (2.2). Do note that these are both very crude approximations but, accordingly, provide the greatest simplicity and hence intuition into to the problem possible.

To demonstrate this we present the low intensity scaling of our models against hydrogen TDSE results in Figure 2.8. It is in this region that we anticipate our field-free treatment to be most applicable. If we apply the small angle approximation to the cotangent function the KR model predicts a $I^{-0.5}$ intensity dependence. In contrast, instead fitting the KR model without this approximation, labelled KR', in the low intensity region yields $I^{-0.44}$ or $I^{-0.41}$ from the TDSE.

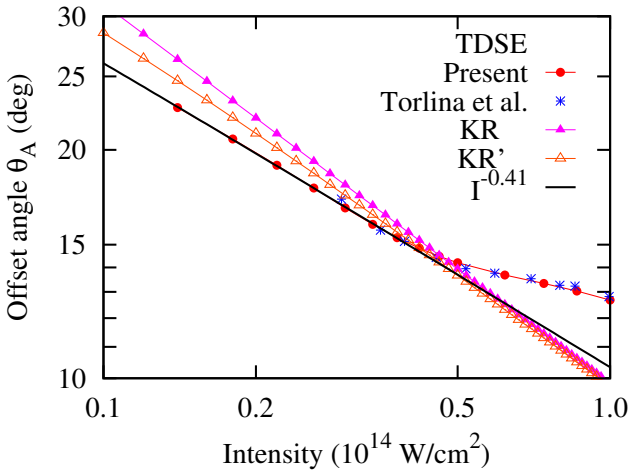

Figure 2.8: The attoclock offset angle θ_A as a function of the field intensity I from the present set of TDSE calculations on hydrogen (red filled circles), the set labelled H2 of [24] (blue asterisks), and the KR and KR$'$ models (filled and empty triangles). The present TDSE results are fitted with $I^{-0.41}$.

Angles extracted from TDSE of various screenings are given in the top frame of Figure 2.9 and contrasted against the prediction from Eq. (2.4), labelled KY', in the bottom frame. In which we find the predicted and calculated dependencies to be broadly similar. The largest exception to this occurs with decreasing intensity for the intermediate λ at which the tunnel width $b = I_p/E_0$ becomes comparable with the screening length and, as such, a classical treatment becomes inadequate

[37]. From this value and beyond, the angle is exponentially suppressed to the point where it is identically zero across all intensities considered at $\lambda = 1$. We take this similarity to classical scattering as further indication that there is no physics contained within this problem that would be attributable to a tunnelling time.

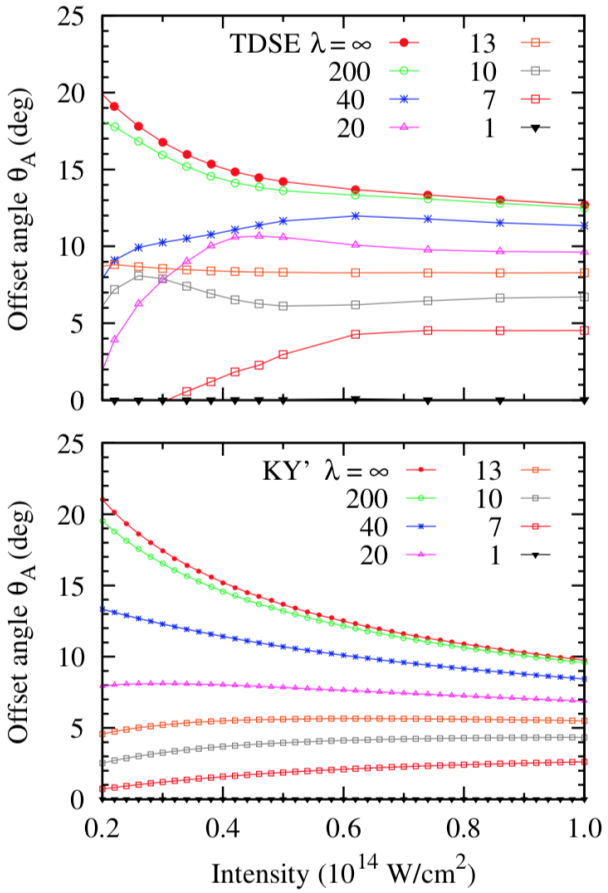

Figure 2.9: The attoclock offset angle as a function of the field intensity for a model Yukawa atom with different screening constants λ. Top: TDSE calculations. Bottom: Predictions of the KY' model.

Finally, to better demonstrate the significance of the attoclock angles dependence with Yukawa screening, we consider the barriers from which the electron must escape at the peak of the pulse in Figure 2.10. With decreasing intensity, the barriers increase in height and width, with the effect on the attoclock angle being a gradual increase. Conversely, an increasing screening yields a similarly wider and higher barrier, yet the resulting angles are decreasing and, in fact, for the strongest screening presented disappear entirely. This again indicates that the attoclock observable is not attributable to the tunnelling process. However, it should be noted that while the initial state energy is identical in each case, their wavefunctions are comparatively compressed in coordinate space, albeit remaining hydrogenic.

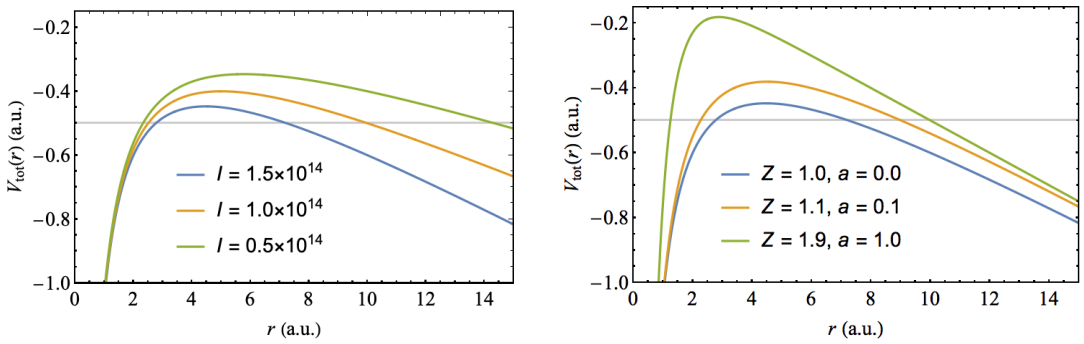

Figure 2.10: Left: The distorted atomic potential at the peak field strength for several intensities in units of W/cm^2. Right: The same but for several Yukawa screenings $a = 1/\lambda$. In the former case the attoclock rotations increase with barrier width and height while in the latter they are strongly suppressed.

2.4 Conclusions

In Section 2.2 we have demonstrated the first agreement between exact *ab initio* theory and experiment by considering an atomic hydrogen target. Additionally, we find that for identical calculations, involving strongly screened Yukawa potentials of the same initial state energy, the rotations in the photoelectron momentum distribution become completely negligible.

In Section 2.3 we examine an idealised attoclock with 'short' near single cycle pulses and make comparison with a simple model based on the assumption of scattering purely due to the effect of the central potential. We hypothesise for such short pulses at low intensity this to be the origin behind the attoclock observable, and indeed find solid qualitative agreement with said model. Additionally, we demonstrate a smooth transition between the hydrogenic and 'hard zero' scenarios with variation of the Yukawa screening parameter.

Taken in aggregate, we consider the above findings as strong evidence against the interpretation of the attoclock rotations in terms of a tunnelling time. This is in addition to a plethora of works coming to the same conclusion by various other means [24, 26–28]. However, it must be said that such work does not directly address the yet outstanding opposite conclusion drawn by the experiments of Landsman *et al.* [20] and Camus *et al.* [23].

Chapter 3

Reconstruction of attosecond beating by interference of two-photon transitions (RABBITT)

This chapter is based on the following publications:

> A. W. Bray, F. Naseem, and A. S. Kheifets, "Simulation of angular-resolved RABBITT measurements in noble-gas atoms," Phys. Rev. A **97**, 063404 (2018).
>
> A. W. Bray, F. Naseem, and A. S. Kheifets, "Photoionization of Xe and Xe@C_{60} from the $4d$ shell in RABBITT fields," Phys. Rev. A **98**, 043427 (2018).

Reconstruction of attosecond beating by interference of two-photon transitions (RABBITT) is a spectroscopic technique in which an attosecond pulse train (APT) 'pump' and its attenuated driving infrared (IR) pulse 'probe' impinge on a target with a well controlled delay between them [38–40]. The APT is comprised in frequency space of a wide range of large odd harmonics and is produced by the process described in Chapter 4. These high energy frequency components ionise the target atom and lead to a series of peaks in the photoelectron with spacing 2ω. Once ionised, they interact with the IR probe field via the mechanism of above threshold ionisation [41], absorbing and emitting photons of energy ω. This leads to the primary ionisation peaks corresponding to the odd harmonics N being interspersed with sidebands at the even harmonics from absorption of an IR photon from the $N\omega$ peak and emission from the $(N+2)\omega$ peak (see Figure 3.1). It is the interference between these two quantum pathways, and the resulting oscillation of their combined signal with the IR/APT delay, that gives rise to the methods name.

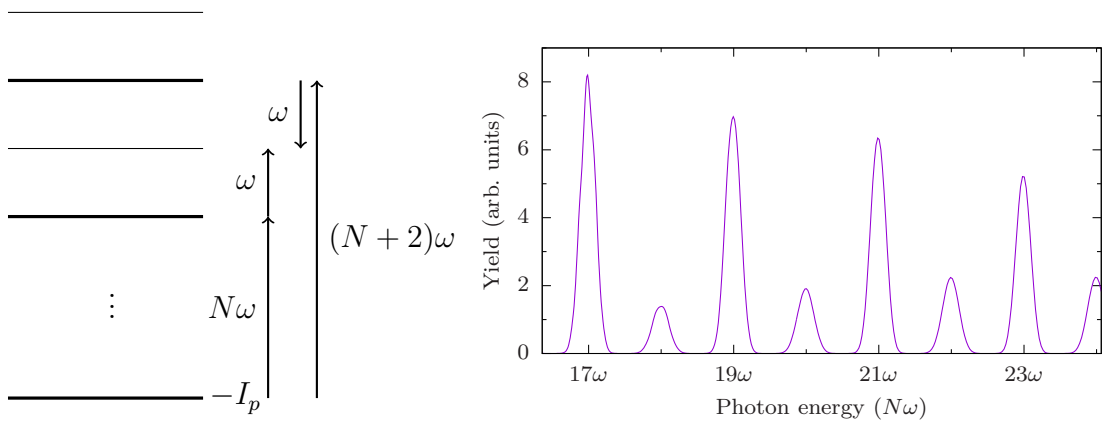

Figure 3.1: Left: depiction of the energy levels involved in the two interfering quantum pathways leading to the $(N+1)\omega$ sideband in a RABBITT measurement. These being absorption of the odd harmonic $N\omega$ followed by an IR photon ω and absorption of the harmonic $(N+2)\omega$ followed by emission of ω. Right: an example of RABBITT spectra, in this case for He at a driving frequency of 780 nm, featuring primary ionisation peaks (PP) at odd harmonics and sidebands (SB) in between.

3.1 Theory

In this section we derive the relation between the TDSE calculated photoelectron spectra and two quantities known as the angular anisotropy parameter β and the Wigner time delay τ_W. It should be noted that our description [42] is contingent on the IR intensity being sufficiently low that the soft-photon approximation is valid [43, 44] and that only single photon absorption or emission from the field is non-negligible. Working under these assumptions allows us to write the amplitude for the sideband as the coherent sum of the two pathways [45, 46]

$$\begin{aligned} T_{\text{sideband}} &= \left|\mathcal{M}_N^{(+)} + \mathcal{M}_{N+2}^{(-)}\right|^2 \\ &= \left|\mathcal{M}_N^{(+)}\right|^2 + \left|\mathcal{M}_{N+2}^{(-)}\right|^2 + 2\left|\mathcal{M}_N^{(+)}\left(\mathcal{M}_{N+2}^{(-)}\right)^*\right| \cos\left[\arg\left(\mathcal{M}_N^{(+)}\left(\mathcal{M}_{N+2}^{(-)}\right)^*\right)\right] . \end{aligned} \tag{3.1}$$

Here $\mathcal{M}_N^{(+)}$ is the amplitude for the absorption of the N XUV harmonic followed by absorption of an IR photon and, similarly, $\mathcal{M}_{N+2}^{(-)}$ is for the $N+2$ harmonic and IR emission.

In the soft photon approximation (see Eqs. (1) and (11) of Maquet and Taïeb [44]) the two above amplitudes are written as

$$\mathcal{M}_N^{(+)} = -2\pi i J_{-1}(\boldsymbol{a}_0 \cdot \boldsymbol{k}) \exp[-i(\phi_N + \phi_{\text{IR}}^{(+)})] \sum_{\psi_i} \langle \boldsymbol{k}|\boldsymbol{\epsilon}\cdot\hat{\boldsymbol{p}}|\psi_i\rangle \tag{3.2}$$

$$\mathcal{M}_{N+2}^{(-)} = -2\pi i J_{+1}(\boldsymbol{a}_0 \cdot \boldsymbol{k}) \exp[-i(\phi_{N+2} + \phi_{\text{IR}}^{(-)})] \sum_{\psi_i} \langle \boldsymbol{k}|\boldsymbol{\epsilon}\cdot\hat{\boldsymbol{p}}|\psi_i\rangle , \tag{3.3}$$

where $\boldsymbol{\alpha}_0 = \boldsymbol{E}_0/\omega^2$, $k \simeq [2((N+1)\omega - I_p)]^{1/2}$ is the shifted momentum of the

photoelectron, approximate as we have neglected the ponderomotive shift of the ionisation potential, ω is the driving IR frequency, $\phi_{\mathrm{IR}}^{(\pm)}$ is the phase associated with absorption or emission of a photon of said frequency, and ϕ_N and ϕ_{N+2} are the two odd harmonic XUV phases. $\langle \boldsymbol{k}|\boldsymbol{\epsilon}\cdot\hat{\boldsymbol{p}}|\psi_i\rangle$ is the velocity form dipole matrix element for the field with polarisation vector $\boldsymbol{\epsilon}$ from the initial bound state $|\psi_i\rangle$ of energy I_p to the continuum state $|\boldsymbol{k}\rangle$. $J_{\pm 1}$ is the corresponding Bessel function of the first kind.

With these expressions, let us now consider the terms in Eq. (3.1). Firstly, we find that

$$\left|\mathcal{M}_N^{(+)}\right|^2,\ \left|\mathcal{M}_{N+2}^{(-)}\right|^2,\ \left|\mathcal{M}_N^{(+)}\left(\mathcal{M}_{N+2}^{(-)}\right)^*\right| \propto |J_1(\boldsymbol{\alpha}_0\cdot\boldsymbol{k})|^2 \sum_{\psi_i} |\langle \boldsymbol{k}|\boldsymbol{\epsilon}\cdot\hat{\boldsymbol{p}}|\psi_i\rangle|^2$$
$$\propto \cos^2\theta\Big[1+\beta P_2(\cos\theta)\Big]\,, \tag{3.4}$$

where we have taken $J_1(x)\simeq x/2+O(x^3)$ and employed both the property $J_{-n}=(-1)^n J_n$ and the summation (Eq. (3.15) of Amusia [47])

$$\frac{d\sigma_i}{d\Omega}=\sum_{\psi_i}|\langle \boldsymbol{k}|\boldsymbol{\epsilon}\cdot\hat{\boldsymbol{p}}|\psi_i\rangle|^2=\frac{\sigma_i}{4\pi}\Big[1+\beta P_2(\cos\theta)\Big]\,. \tag{3.5}$$

Here σ_i and $d\sigma_i/d\Omega$ are the total and differential photoionisation cross-sections for the i-th atomic shell, respectively, and θ is the polar angle from the axis aligned with the laser polarisation $\boldsymbol{\epsilon}$. β is known as the angular anisotropy parameter which characterises the change in cross-section with θ and P_2 is the 2nd order Legendre polynomial. Hence, we expect both our constant value and magnitude of oscillation with the interference to behave as Eq. (3.4).

For the phase of the interference term in Eq. (3.1) we have

$$\arg\left(\mathcal{M}_N^{(+)}\left(\mathcal{M}_{N+2}^{(-)}\right)^*\right)=2\omega\left(\tau_{\mathrm{GD}}+\tau_{\mathrm{CC}}+\tau_{\mathrm{W}}\right)\,, \tag{3.6}$$

where the finite difference group delay of the XUV is

$$\tau_{\mathrm{GD}}=\frac{\phi_{N+2}-\phi_N}{2\omega}\,, \tag{3.7}$$

the continuum-continuum (CC) delay associated with the difference between IR absorption and emission is

$$\tau_{\mathrm{CC}}=\frac{\phi_{\mathrm{IR}}^{(-)}-\phi_{\mathrm{IR}}^{(+)}}{2\omega}\,, \tag{3.8}$$

and the Wigner delay is

$$\tau_{\mathrm{W}}\equiv\frac{1}{2\omega}\arg\left[\sum_{\psi_i}|\langle \boldsymbol{k}|\boldsymbol{\epsilon}\cdot\hat{\boldsymbol{p}}|\psi_i\rangle|^2\right]\,. \tag{3.9}$$

Additionally, we observe that if we introduce a shift τ to the IR relative to the APT we add a further phase $2\omega\tau$ to (3.6). Hence, in aggregate, we expect the RABBITT signal (3.1) to behave as

$$T_{\text{sideband}} = A + B\cos(2\omega\tau - C)\ , \tag{3.10}$$

where

$$\begin{aligned} A,\ B &\propto \cos^2\theta\Big[1 + \beta P_2(\cos\theta)\Big] \\ C &= 2\omega(\tau_{\text{GD}} + \tau_{\text{CC}} + \tau_{\text{W}})\ . \end{aligned} \tag{3.11}$$

Though note in the following we will take $\tau_{\text{GD}} = 0$ as by our construction (see (3.12)) $\phi_N = 0$ for each odd harmonic N. We will refer to the remainder $\tau_a = \tau_{\text{CC}} + \tau_{\text{W}}$ as the atomic time delay.

3.1.1 RABBITT pulse description

In our calculation the RABBITT external field is the sum of both XUV and IR fields. The XUV field is modelled by an attosecond pulse train (APT) with the vector potential

$$A_x(t) = \sum_{n=-5}^{5} (-1)^n A_n \exp\left(-2\ln 2\frac{(t - nT/2)^2}{\tau_x^2}\right) \times \cos\Big[\omega_x(t - nT/2)\Big]\ , \tag{3.12}$$

where

$$A_n = A_0 \exp\left(-2\ln 2\frac{(nT/2)^2}{\tau_T^2}\right)\ .$$

Here $T = 2\pi/\omega$ is the period of the IR field. By placing alternating sign attosecond pulses at each half period, the field is spectrally comprised of odd harmonics about a central XUV frequency of ω_x and the relative strength of neighbouring harmonics about this determined by time constants τ_x, τ_T. Each are chosen as appropriate for the various atoms of interest based on their ionisation energies.

The vector potential of the IR pulse is modelled by the cosine squared envelope

$$A(t) = A_0\cos^2\left(\frac{\pi(t-\tau)}{2\tau_{\text{IR}}}\right)\cos[\omega(t-\tau)]\ , \tag{3.13}$$

of duration $\tau_{\text{IR}} = 14.5$ fs and zero otherwise. The IR pulse is shifted relative to the APT by a variable delay τ.

3.2 Noble gasses

In this section we present the results of our computations of β and τ_{W} within our single active electron (SAE) TDSE approach. By considering Ne though to Xe, our goal is to both test the validity of several differing effective potentials as well as the universality of a hydrogenic continuum-continuum correction τ_{CC}. This latter point is motivated by the persistent disagreement between theory and experiment for Ar, in which a hydrogenic correction was used [48]. More recently, however, a similar situation was rectified for Ne [49] in contrast to an earlier experiment [50].

3.2.1 Effective potentials

As in the previous work on He and Ne [46], we employed an optimized effective potential (OEP) [51]. This potential is derived by a simplified treatment of the exchange term in the Hartree-Fock (HF) equations using the Slater X-α ansatz [52]. The OEP potential takes the form

$$V_e(r) = -\frac{1}{r}\left(1 + (Z_0 - 1)\sum_{p=0}^{S}\sum_{k=1}^{n_p} c_{k,p} r^p e^{-\beta_{k,p} r}\right) \equiv -\frac{Z^*(r)}{r} \,, \tag{3.14}$$

where the effective charge $Z^*(r)$ varies from the unscreened nucleus charge Z_0 as $r \to 0$ and unity at large distances $r \to \infty$. The former limit is satisfied by imposing the condition $\sum_{k=1}^{n_0} c_{k,0} = 1$.

A further model potential that we employ is that of a localized Hartree-Fock (LHF) potential generated from a known continuous orbital calculated in a frozen HF core [53]. The radial Schrödinger equation with the atomic Hamiltonian can be rewritten such that the LHF is expressed in terms of the known HF radial orbital and its second derivative

$$V_{\mathrm{HF}}(r) = \frac{\kappa^2}{2} - \frac{\ell(\ell+1)}{2r^2} + \frac{P''_{\kappa\ell}(r)}{P_{\kappa\ell}(r)} \,. \tag{3.15}$$

The LHF should be weakly sensitive to the choice of the momentum κ and the orbital momentum ℓ. For practical reasons, we chose $\kappa = 0.01$ and $\ell = 0$ to avoid multiple nodes of $P_{\kappa\ell}(r)$ where the RHS of Eq. (3.15) diverges. The effective charge $Z^* = -rV_{\mathrm{HF}}(r)$ derived from Eq. (3.15) is a smooth function outside of these nodes and can be fitted with an analytical expression

$$Z^*_{\mathrm{HF}}(r) = (Z_0 - 1)e^{-\alpha r} + 1 \,. \tag{3.16}$$

The $p = 0$ term in Eq. (3.14) is analogous to the Muller potential introduced

specifically for Ar [40]

$$V_{\mathrm{M}}(r) = -\frac{1}{r}\Big[1 + 5.4\exp(-r) + 11.6\exp(-3.682r)\Big] \ . \tag{3.17}$$

Miller and Dow [54] suggested an alternative analytical expression

$$Z^{*}_{\mathrm{MD}}(r) = 1 + \frac{(Z_0 - 1)(1 - r/R)^2\theta(R - r)}{1 + Cr + Dr^2} \ , \tag{3.18}$$

where $\theta(R-r)$ is the unit step function. The numerical parameters R, C and D are chosen to match the variation of the angular anisotropy parameter β with energy across the Cooper minimum (CM) known from experiment.

The valence shell energies calculated with various model potentials along with the experimental threshold energies are compiled in Table 3.1. For the LHF potential, we also show in parentheses the α parameters from Eq. (3.16).

Table 3.1: The valence shell energies, in atomic units, calculated with various model potentials. The experimental thresholds are from [55]. The LHF entries also contain the α parameters from Eq. (3.16).

Method	Ne $2p$	Ar $3p$	Kr $4p$	Xe $5p$
Expt [55]	0.792	0.579	0.514	0.445
HF	0.850	0.591	0.524	0.457
OEP [51]	0.851	0.590	0.528	0.467
LHF	0.843(2.29)	0.583(2.11)	0.202(2.80)	0.412(2.54)
Muller [40]		0.581		
MD [54]		0.423	0.203	

3.2.2 Neon $2p$

In Figure 3.2 we display the angular anisotropy β parameters for the Ne $2p$ valence shell extracted from the TDSE calculations with the LHF potential (top) and the OEP potential (bottom). The β^{HH} parameters extracted from the angular dependence of the high harmonic peaks are plotted along with the β^{SB} parameters extracted from the angular variation of the RABBITT A and B parameters in Eq. (3.11). We make comparison with those computed via the random phase approximation with exchange (RPAE, see Section 4.1.1) shown with the solid line. This calculation is known to reproduce accurately the experimental β parameters across the studied photon energy range [56].

We see that the harmonics and sidebands TDSE calculations of β parameters are consistent between each other and are fairly close to the XUV-only RPAE cal-

culation, with the LHF results marginally closer to the RPAE than the OEP ones. In the previous work [46] they employed the OEP potential and quoted $\beta^{\mathrm{SB}} \simeq 0.3$ for sideband 20 (SB20) which is in reasonable agreement with the present results of both potentials.

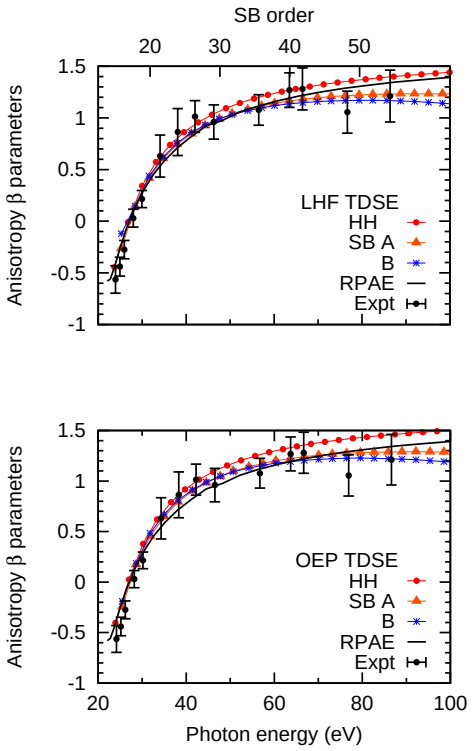

Figure 3.2: Angular anisotropy β parameters for the Ne $2p$ valence shell extracted from the TDSE calculations with the LHF potential (top) and the OEP potential (bottom). The β^{HH} parameters extracted from the angular dependence of the high harmonic peaks are plotted with (red) filled circles. The same parameters β^{SB} extracted from the angular variation of the RABBITT A and B coefficients in Equation (3.11) are plotted with (orange) triangles and (blue) asterisks, respectively. The RPAE calculation is shown with the solid line. The experiment [56] is given by the points with the error bars.

Angular dependence of the atomic time delay $\tau_a(\theta_k)$ as a function of the escape angle is shown in Figure 3.3. The top and middle panels display the TDSE calculations with the LHF and OEP potentials, respectively. The bottom panel shows the angular dependence of the Wigner time delay $\tau_{\mathrm{W}}(\theta_k)$ from the XUV-only RPAE calculation. We see that both TDSE calculations are quite close to one another while the RPAE calculation suggests an angular dependence which is an order of magnitude weaker. The consequence being that nearly all the angular dependence of the atomic time delay in Ne comes from the CC correction introduced by the probe IR field. A similar observation was made in He where the Wigner time delay is isotropic [57]. In Ne, the Wigner time delay is not entirely isotropic because the $2p \to \epsilon s$ and $2p \to \epsilon d$ channels enter the ionization amplitude with their own spherical harmonics,

namely $Y_{00}(\theta_k)$ and $Y_{20}(\theta_k)$. However, as a result of the Fano propensity rule [58], the d-continuum is strongly dominant and the s-continuum contributes only a very weak angular modulation. We note that this situation would change drastically near the CM in Ar and heavier noble gases where the angular dependence of the Wigner time delay is very strong.

The time delay in the polarization axis direction $\theta_k = 0$ is shown in Figure 3.4. On the top panel, we compare the atomic time delay from the TDSE calculation with the LHF potential and the Wigner time delay τ_{W} from the RPAE calculation. The hydrogenic CC correction τ_{CC}, which is shown separately, is then added to the Wigner time delay. This correction, as a function of the photoelectron energy, is represented by the analytic expression

$$\tau_{\mathrm{CC}}(E) = NE^{-3/2}[a\log(E) + b]\ , \tag{3.19}$$

where the coefficients N, a, and b are found from fitting the regularized continuum-continuum delay shown in Fig. 7 of [59]. We see that except for the near threshold region where the photoelectron energy is very small and where the regularization of τ_{CC} may not be applicable, the identity $\tau_a \simeq \tau_{\mathrm{W}} + \tau_{\mathrm{CC}}$ holds very well.

3.2.3 Argon 3*p*

The β parameters for the Ar $3p$ shell extracted from the angular dependence of the high harmonic peaks and sidebands are shown in Figure 3.5. The TDSE calculations performed with the LHF and OEP potentials are shown on the top and bottom panels, respectively. The three sets of β parameters are compared with the RPAE calculation and the experiment [60]. We observe from this figure that all three sets of β parameters extracted from the TDSE calculation with the LHF potential follow closely the RPAE prediction and agree with the experiment. At the same time, the OEP TDSE results are displaced relative to the RPAE in the photon energy scale by as much as 10 eV. This mismatch is a reflection of the displacement of the CM position in the photoionisation cross-section. This position can be located very accurately from the squared radial integral [61]

$$\left| \int_0^\infty P_{3p}(r) P_{Ed}(r)\ r dr \right|^2 \ . \tag{3.20}$$

A plot of this integral is given in Figure 3.6 where the radial orbitals of the bound and continuous states have been calculated using the LHF, OEP, Muller [40], and Miller and Dow [54] potentials. The equivalent value from the HF and RPAE calculations are also shown. We see that the CM position is misplaced for each of the potentials except the LHF. Subsequently, in the following, we present our TDSE re-

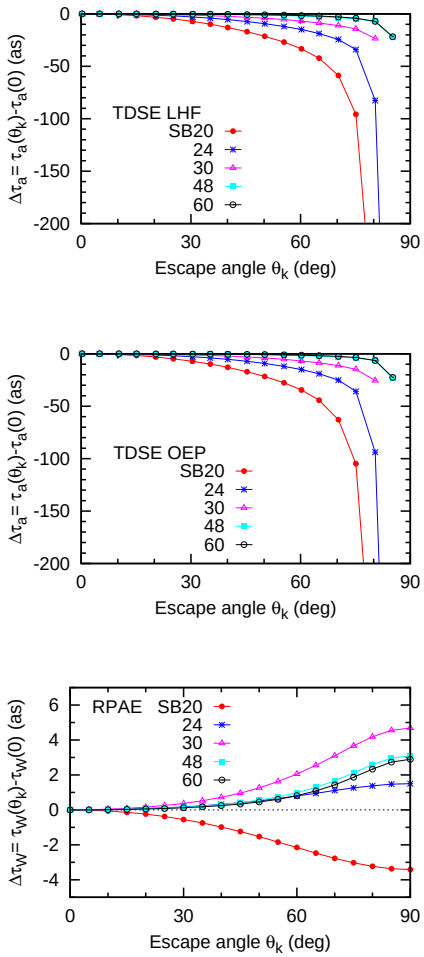

Figure 3.3: Angular variation of the atomic time delay $\Delta\tau_a = \tau_a(\theta_k) - \tau_a(0)$ in various sidebands of the Ne $2p$ RABBITT trace calculated with the LHF potential (top) and the OEP potential (middle). Bottom: angular variation of the Wigner time delay $\Delta\tau_{\mathrm{W}} = \tau_{\mathrm{W}}(\theta_k) - \tau_{\mathrm{W}}(0)$ from the XUV-only RPAE calculation.

sults calculated with the LHF potential only. The angular variations of the atomic time delay $\Delta\tau_a = \tau_a(\theta_k) - \tau_a(0)$ in various sidebands of the Ar $3p$ RABBITT trace, and the Wigner time delay angular variation $\Delta\tau_{\mathrm{W}} = \tau_{\mathrm{W}}(\theta_k) - \tau_{\mathrm{W}}(0)$ at the same photon energies, are displayed in Figure 3.7 (top and bottom panels respectively). In stark contrast to the analogous set of data for Ne $2p$ shown in Figure 3.3, the angular variation of the Wigner time delay for Ar $3p$ is of the same order of magnitude, and is almost identical for SB30 near the CM. As a reference, in both panels of Figure 3.7, the lowest order perturbation theory (LOPT) calculation [62] for SB32 is shown. Beyond the CM (SB48 and SB60), the angular variation of the Wigner time delay flattens whereas the same variation of the atomic time delay changes its sign and simultaneously weakens in magnitude. In Figure 3.8 we compare the angular variation of the atomic time delay $\Delta\tau_a = \tau_a(\theta_k) - \tau_a(0)$ in SB14 (top) and SB16. In the experiment [63], SB16 is tuned in resonance with the $4s^{-1}5p$ autoionising state

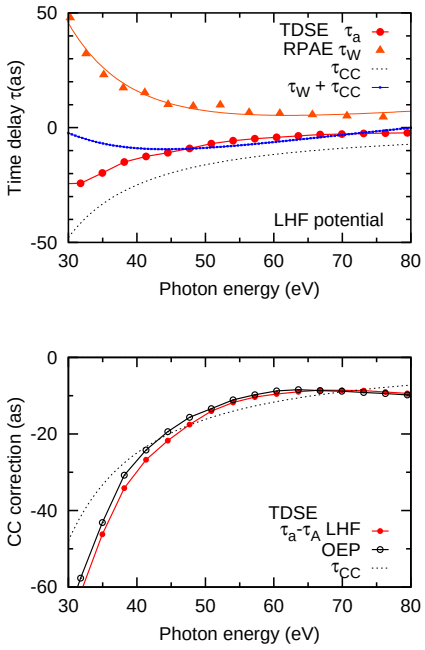

Figure 3.4: Time delay in the polarization axis direction $\theta_k = 0$. Top: the atomic time delay τ_a from the TDSE calculation (red filled circles) is compared with the Wigner time delay (orange triangle) from the RPAE calculation. The CC correction $\tau_{\rm CC}$ is shown with the thin dotted line whereas the sum $\tau_{\rm W} + \tau_{\rm CC}$ is displayed with the (blue) dotted line. Bottom: the CC correction $\tau_{\rm CC}$ (thin dotted line) is compared with the atomic and Wigner time delay difference $\tau_a - \tau_{\rm W}$ from the TDSE calculations with the LHF and OEP potentials (shown with the red filled and black open circles).

while SB14 is off the resonance. For SB14 we find a fairly good agreement between the experiment and the present LHF TDSE calculation. The LOPT calculation reported in [63] is also very close. For SB16 both the TDSE and LOPT calculations predict considerably weaker angular dependence than in the experiment and the calculation which accounts for resonance by the Fano configuration interaction formalism.

Various time delays for the Ar $3p$ shell in the zero angle polarization direction are shown in Figure 3.9. On the top panel, we display the atomic time delay τ_a from the TDSE LHF calculation, the Wigner time delay $\tau_{\rm W}$ from the RPAE calculation, the regularized hydrogenic CC correction $\tau_{\rm CC}$ and their sum $\tau_{\rm W} + \tau_{\rm CC}$. We also show the atomic time delay τ_a from the LOPT calculation [62]. The latter is almost indistinguishable from the sum $\tau_{\rm W} + \tau_{\rm CC}$, but visibly different from the TDSE calculation for τ_a. On the bottom panel we show the hydrogenic $\tau_{\rm CC}$ and the argon specific value $\tau_{\rm CC} = (\phi^-_{\rm CC} - \phi^+_{\rm CC})/2\omega$ obtained from the phases $\phi^\pm_{\rm CC}$ reported in [63]. Both values, which are remarkably close, are compared with the difference $\tau_a - \tau_{\rm W}$. Unlike in the Ne $2p$ case, displayed on the bottom panel of Figure 3.4, these two derivations of the CC correction give quite different results. This difference may

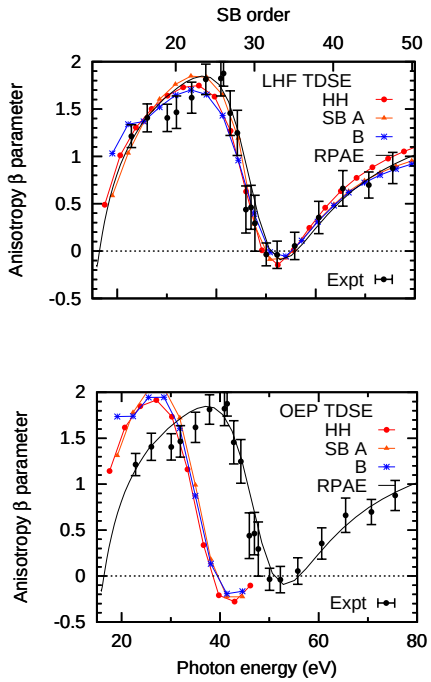

Figure 3.5: The same as Figure 3.2 for Ar $3p$ shell. The experiment [60] is given by the points with error bars.

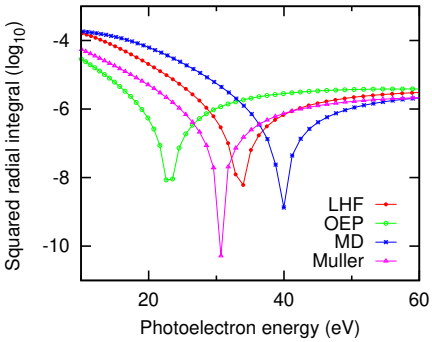

Figure 3.6: The squared radial integral (3.20) calculated with the LHF (red filled circles), OEP (open green circles), Miller and Dow [54] (blue asterisks) and Muller [40] (purple triangles) potentials for Ar. The HF and RPAE results are shown with black dotted and solid lines respectively.

in principle be attributed to the different approximations used in TDSE-LHF and RPAE calculations. The former employs a localized version of the HF potential and neglects the correlation while the latter gives the full account to the exchange and inter-shell correlation. However, the same calculations return quite similar sets of β parameters. As such it is more likely that the hydrogenic approximation to τ_{CC} breaks for the argon $3p$ shell.

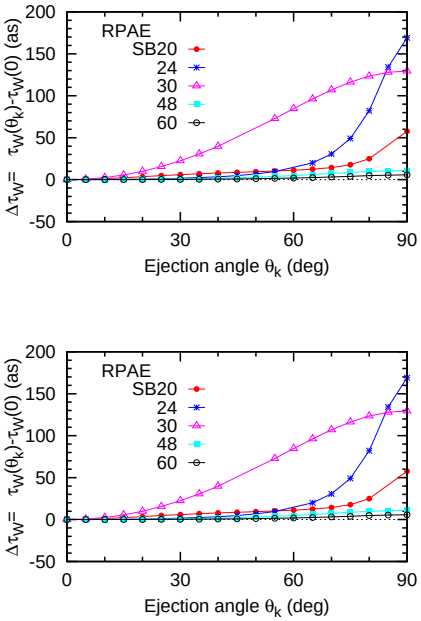

Figure 3.7: Top: angular variation of the atomic time delay $\Delta\tau_a = \tau_a(\theta_k) - \tau_a(0)$ in various sidebands of the Ar $3p$ RABBITT trace calculated with the LHF potential. Bottom: angular variation of the Wigner time delay $\Delta\tau_{\mathrm{W}} = \tau_{\mathrm{W}}(\theta_k) - \tau_{\mathrm{W}}(0)$ from the XUV-only RPAE calculation. The angular variation of time delay for SB32 from [62] is shown for comparison.

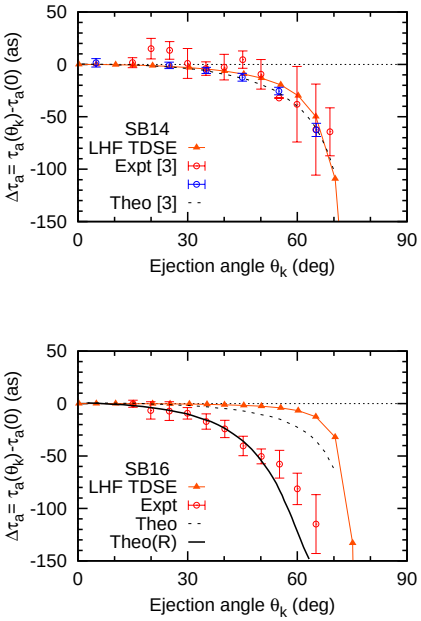

Figure 3.8: The same as Figure 3.7 for SB14 (top) and SB16 (bottom). Two sets of measurements from [63] are shown by open circles with error bars. The LOPT result from the same work is visualized by a dashed line. The LHF TDSE result is shown with orange triangles connected by the solid line. The bottom panel also shows the calculation from [63] which includes the Fano resonance (black solid line).

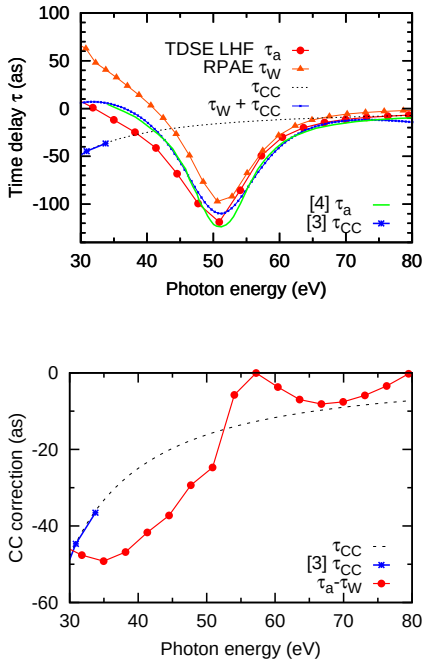

Figure 3.9: The same as Figure 3.4 for Ar $3p$ shell. In addition, the atomic time delay τ_a from the LOPT calculation [62] and the CC correction $\tau_{\rm CC} = (\phi^-_{\rm CC} - \phi^+_{\rm CC})/2\omega$ obtained from the phases $\phi^\pm_{\rm CC}$ reported in [63] are shown.

3.2.4 Krypton $4p$

We test validity of various effective potentials for Kr by determining the CM position in the $4p$ photoionisation cross-section. We do so by comparing the squared radial integrals (3.20) calculated with the bound state $4p$ orbital and the continuous d-wave. This comparison is shown in Figure 3.10. Unlike in the case of Ar $3p$ photoionisation, illustrated in Figure 3.6, the CM position calculated in the HF and RPAE differs by nearly 20 eV. This is so because of the influence of the inter-shell correlation between the $4p$ and $3d$ shells which is accounted for in the RPAE but not in the HF calculation. This correlation is absent in the case of Ar $3p$ as the $3d$ shell is vacant for this atom. The CM position calculated with the LHF and MD potentials is in between the HF and RPAE whereas the OEP calculation displaces the CM to lower energies very significantly. We discard the OEP in the following.

The three sets of angular anisotropy β parameters extracted from the high harmonic peaks and the side bands are shown in Figure 3.11 calculated with the LHF (top) and MD (bottom) potentials. We see that agreement between the TDSE and RPAE calculations is generally good but these calculations diverge at higher photon energies. This occurs well below the $3d$ threshold whose position can be identified by the converging autoionisation resonances visible in the RPAE curve. The experiment [64] clearly favours the RPAE calculation. Partial agreement between the

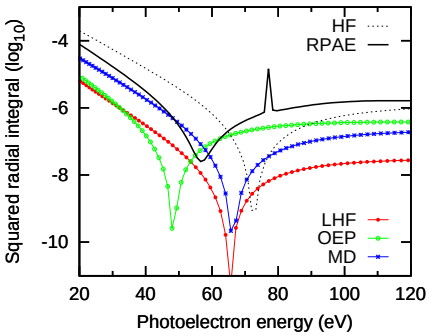

Figure 3.10: The squared radial integral (3.20) calculated with the LHF (red filled circles), OEP (open green circles), Muller [40] (blue asterisks) and Miller&Dow [54] (purple triangles) potentials for Kr. The HF and RPAE results are shown with black dotted and solid lines respectively.

TDSE calculations with the LHF and MD potentials, the RPAE, and the experiment may be somewhat fortuitous given a strong deviation of the TDSE binding energies from the experimental threshold (see Table 3.1). Should the β parameters in Figure 3.11 be plotted versus the photoelectron energy, this agreement will disappear.

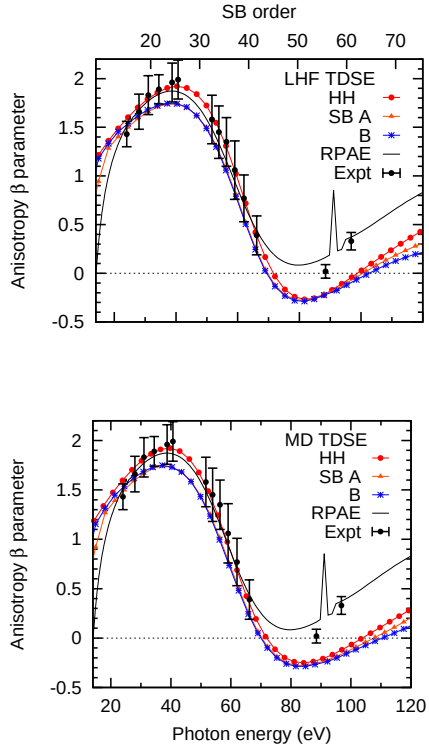

Figure 3.11: The same as Figure 3.2 for the Kr $4p$ shell. The experimental data are from [64].

3.2.5 Xenon 5*p*

This tendency of deviation of the TDSE calculations with various local potentials from the RPAE and experiment is aggravated further in Xe. As an illustration, we show in Figure 3.12 the CM position deduced from the squared radial integral (3.20). Firstly, we observe that the HF and RPAE results diverge by as much as 40 eV. This is a clear sign of a very strong correlation between the 5*p* and 4*d* shells accounted for in the RPAE but missing in the HF. Similarly, both the LHF and OEP give CM positions displaced by 20 eV from the RPAE.

It is well known that missing the inter-shell correlation between the 5*p* and 4*d* shells in Xe has a profound effect on the anisotropy β parameter. It becomes strongly displaced relative to the experiment as shown graphically in Figure 1 of [65]. We therefore do not expect any reasonable agreement of the presently employed TDSE/SAE model with the experiment either.

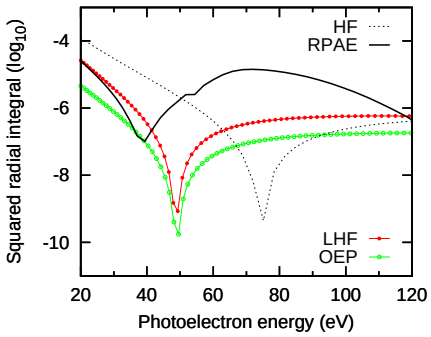

Figure 3.12: The squared radial integral (3.20) calculated with the LHF (red filled circles), and OEP (open green circles) potentials for Xe. The HF and RPAE results are given by the black dotted and solid lines respectively.

3.3 C_{60} caged Xe

In this section we examine the RABBITT process from the 4*d*-shell of Xe within our SAE TDSE approach. Away from the inner 4*p* threshold, the effects of intershell correlation are negligible. This is in contrast to ionisation from the 5*p* orbital considered earlier (Section 3.2.5). Additionally, we consider the effect of a encapsulating C_{60} cage by adding the potential

$$V(r) = \begin{cases} -U_0 < 0 & \text{if } R_{\text{inner}} \leq r \leq R_{\text{inner}} + \Delta \\ 0 & \text{otherwise} \end{cases}, \tag{3.21}$$

to that used in Section 3.2.5. Here $R_{\text{inner}} = 5.8$ a.u., $\Delta = 1.9$ a.u., and $U_0 = 0.302$ a.u. Such a simple model is adequate in the present case because the 4*d*-shell

is sufficiently deeply bound such that it cannot hybridize with any of the levels of C_{60}. In addition, the photon energy range (80 to 200 eV) is well away from the C_{60} plasmons so that interchannel coupling with atomic photoionisation is negligible.

The calculations for the free Xe and encapsulated Xe@C_{60} atoms are shown along with their difference in Figure 3.13. The corresponding sets of β parameters from the XUV only RPAE calculation are displayed on the top panel of this figure. The two sets of experimental data collated in [66] are shown with empty circles and diamonds. The β parameters display a fair correspondence between the RPAE and the three sets from the TDSE HH, A, and B parameters. The β oscillations with photon energy in the trapped Xe@C_{60} atom are similar but somewhat dampened in the TDSE calculation as compared to the RPAE. The progressive deviation of the RPAE calculation from the experiment visible on the top panel of Figure 3.13 indicates an onset of the $4d/4p$ inter-shell correlation which is not included in the present calculation. This agreement can be significantly improved in a fully relativistic RRPA calculation with inclusion of all interacting shells [67].

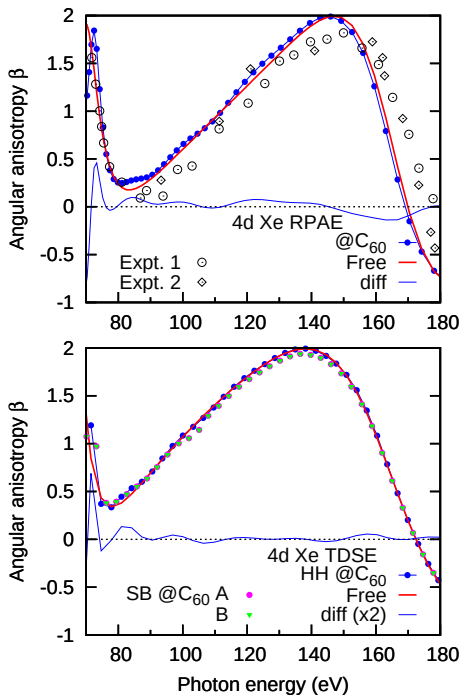

Figure 3.13: Angular anisotropy β parameters of the $4d$-shell of Xe from the RPAE (top) and TDSE (bottom) calculations. The dotted line visualises the encapsulated Xe@C_{60} atom whereas the solid red line displays the free Xe atom. The difference of the Xe@C_{60} and Xe results is highlighted by a thin blue solid line. The three sets of the β parameters in the TDSE are deduced from the angular variation of the high harmonic peaks (HH) as well as the A and B parameters (3.11). The cage-free experimental data collated in [66] are shown with empty circles and diamonds (top panel).

The atomic time delay in the polarization direction is shown in Figure 3.14. On

the top panel we show the RPAE result which we express as the sum $\tau_a = \tau_{\mathrm{W}} + \tau_{\mathrm{cc}}$ of the Wigner time delay and the regularized CC correction displayed in Fig. 7 of [59]. The Wigner time delay is calculated as the energy derivative of the phase of the $4d$ photoionisation amplitude [68]. On the bottom panel we show the TDSE result calculated directly using Eq. (3.11). We see that both sets of calculations show a close correspondence, both for the free and encapsulated Xe atoms. The largest oscillation of the time delay occurs at the same photon energy range as of the β parameter and the angular integrated cross-section. The energy ($\approx$ 80 eV) corresponds to the de Broglie wavelength resonating with the fullerene cage.

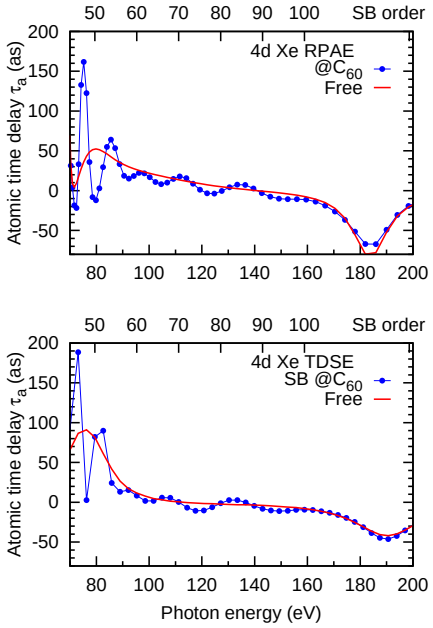

Figure 3.14: Atomic time delay τ_a in the polarization direction deduced from the RPAE calculation as the sum $\tau_{\mathrm{W}} + \tau_{\mathrm{cc}}$ (top) and as obtained directly from TDSE by Eq. (3.11) (bottom). The dotted blue line visualizes the Xe@C_{60} calculation whereas the solid red line shows the free Xe atom result.

The angular variation of the atomic time delay $\Delta\tau_a = \tau_a(\theta_k) - \tau_a(0)$ is displayed in Figure 3.15 for the free (top) and encapsulated (bottom) Xe atoms. In this figure we selected the sidebands where the energy oscillation of the time delay shown in Figure 3.14 is largest. We see that the angular variation changes significantly with increase of the SB order. This change is somewhat larger in the free Xe atom with a significant negative variation in SB48 and 50. This effect is less prominent in the Xe@C_{60} atom. All the sidebands presented with the except SB44 only exhibit noticeable angular variation close to 90° emission angle.

At higher photon energies, the $4d \rightarrow Ef$ photoionisation channel dominates completely and the angular variation of the time delay vanishes. Another area of a significant angular variation of the time delay is near the Cooper minimum

above the photon energy of 180 eV. This region is shown in Figure 3.16. Here the angular variation is always positive and the time delay grows with increasing photoelectron emission angle. This growth begins immediately with the angular increase in contrast to the near threshold region shown in Figure 3.15. It is attributed to the weakening of the typically stronger $4d \rightarrow Ef$ photoemission channel and a more intense competition from its normally minor partner $4d \rightarrow Ep$. The effect of trapping is minimal at the photoelectron energy as the de Broglie wavelength is much smaller than the cage radius.

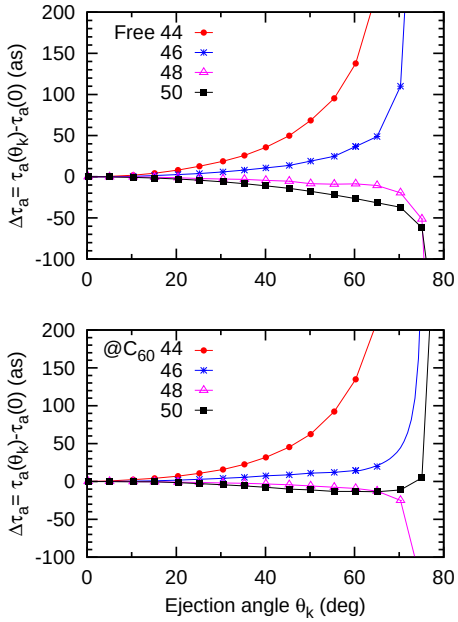

Figure 3.15: Angular variation of the atomic time delay $\Delta\tau_a = \tau_a(\theta_k) - \tau_a(0)$ with the photoelectron emission direction for various side bands. Top: the free Xe atom, bottom - the trapped Xe@C_{60} atom.

3.4 Conclusions

Our results can be broadly categorized into the two groups. In lighter atoms, Ne and Ar, the single active electron model is generally valid. The Ne calculations are particularly robust with all the tested effective potentials producing accurate results close to the RPAE predictions both for the angular anisotropy and the time delay. In Ar, because of the appearance of the Cooper minimum, the TDSE calculations become very sensitive to the choice of the effective potential and a simple analytic fit to the localized HF potential produces the best results for β parameters. At the same time, this calculation suggests deviation of the CC correction from the regularized hydrogenic expression. Because of the Cooper minimum, the angular

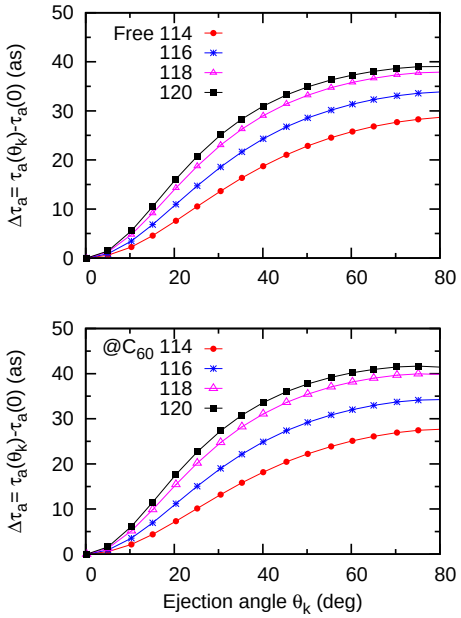

Figure 3.16: The same as in Figure 3.15 near the Cooper minimum.

variation of the Wigner time delay is of the same magnitude as the variation of the atomic time delay. In Ne, the angular variation of the Wigner time delay is negligible.

In heavier atoms, Kr and particularly in Xe, the inter-shell correlation between the valence np-shell and sub-valent $(n-1)d$-shell becomes very strong. In Kr, with some choice of effective potentials, the present model can return sensible Cooper minimum position and β parameters away from the $(n-1)d$ shell threshold. In Xe, no effective potential is expected to replace the strong effect of inter-shell correlation and the present model is generally invalid.

Finally, we examined the effect of a C_{60} cage on the RABBITT ionisation of the $4d$-shell of Xe in a region away from resonances. The computed angular anisotropy parameters and time delays are generally quite close with the largest effect being when the photoelectron de Broglie wavelength $\lambda = 2\pi/k$ is close to the cage radius R. Approaching this point, significant oscillations with energy of these quantities occur.

Chapter 4

High harmonic generation (HHG)

This chapter is based on the following publication:

> A. W. Bray, D. Freeman, S. Eckart, and A. S. Kheifets, "Correlation enhancement of high-order harmonic generation in Xe," Phys. Rev. A **100**, 013404 (2019).

High harmonic generation (HHG) is the process by which an atom interacting with an intense laser pulse re-emits radiation at large multiples of the driving frequency. This upconversion is made possible by the strong non-linearity of said interaction [69]. Thought of as a three step (or simple man) model [70–72] the process is comprised of: (1) tunnel ionisation, (2) propagation, and (3) radiative recombination (see Figure 4.1). Accordingly HHG is most often considered involving linearly polarised fields for which the probability of recombination is high. In such a case, along with validity of the dipole approximation (see Section 1.2.1) and a homogeneous medium, only odd harmonics may be produced due to the inversion symmetry present [73, 74].

A typical HHG spectrum is characterised by a rapid decrease for low harmonics, a broad plateau region, and finally a sharp cutoff beyond a photon energy $E_{\text{cutoff}} \simeq 3.17U_p + I_p$. This cutoff is explained within the three step model as the maximum energy the electron can gain during the propagation stage. For a given gained energy there are two corresponding classical trajectories, one 'short' and another 'long' in terms of recombination time [75]. At the cutoff energy, the two classical trajectories within the model converge. The purely quantum analogue of this model [76, 77] makes use of the saddle point approximation and in doing so similarly invites interpretation via short and long trajectories.

In an experimental target, there are a multitude of atoms each of which is a contributing source of radiation. For their coherent sum to be a simple multiple of that of a single atom, each must be phase matched such that they are constructively interfering with one another. However, this is made complicated by differing intensity

dependencies of the phase from the contributing short and long trajectories as well as dispersive effects from the presence of free electrons in the medium generated by ionisation [78–81]. Theoretically these effects can be modelled by accounting for the experimental geometries and simultaneously solving Maxwell's equations in concert with TDSE albeit with some complications regarding boundary conditions [82]. Conversely, macroscopic effects can be experimentally minimised by working in regimes where ionisation is negligible, employing thin targets, and optimising geometries [83, 84]. Similarly, in two colour HHG, the breaking of symmetry between subcycles means only a single trajectory contributes and accordingly needs to be phase matched [85, 86].

Most importantly, by further novel field combinations or exploiting macroscopic phenomena, single [87, 88] or trains [39, 89] of attosecond pulses can be generated. Employing such pulses grants access to the timescale at which electrons evolve, the study of which is now termed attosecond science. As such, maximising the conversion efficiency of their generation is of considerable interest. One such mechanism for achieving this is simply increasing the source density by using solid targets [90–92]. Another is by making use of the greatly enhanced probability of recombination driven by electron correlation [83–86, 93]. It is the latter mechanism that we investigate in the remainder of this chapter.

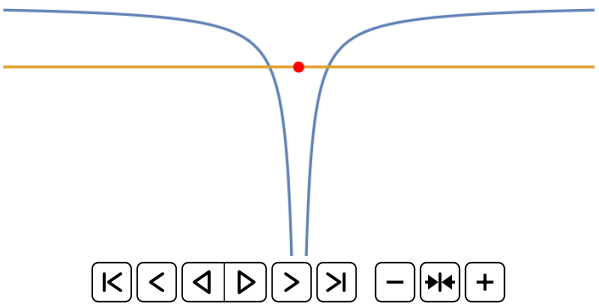

Figure 4.1: (Animation for javascript enabled PDF viewer, left to right stills in print) The distortion of the atomic potential as a function of time within a single cycle of a linearly polarised pulse to illustrate the three-step HHG process. The electron tunnel ionises, propagates, is driven back towards the parent ion, and radiatively recombines. The blue curve depicts the potential $-1/r + \boldsymbol{E}(t) \cdot \boldsymbol{r}$, the orange line the ground state energy of -0.5 a.u., the red dot the electron, and the black undulating line the emitted photon.

4.1 Theory

The expectation value of the power radiated by a single atom is given by the Larmor formula [94, 95]

$$\langle \boldsymbol{P}(t) \rangle = \frac{2}{3c^2} \left\langle \left[\frac{\mathrm{d}^2 \boldsymbol{r}(t)}{\mathrm{d}t^2} \right]^2 \right\rangle , \tag{4.1}$$

where c is the speed of light. This proportionality to the acceleration can be seen from entirely classical physics in which it is directly proportional to the electric field which, when squared, gives the power. The spectral composition is then analysed by taking the Fourier transform.

However, it is not uncommon to compute instead the spectra via only the displacement $\langle \boldsymbol{r}(t) \rangle$ (differing from the dipole by a factor of q) [96]. Importantly, this is only equivalent upon multiplication by ω^4 when the dipole is vanishing for large t and hence ionisation must be negligible [97]. In the following, we choose instead a more general approach of computing the acceleration directly via

$$\begin{aligned} \left\langle \frac{\mathrm{d}^2 \boldsymbol{r}(t)}{\mathrm{d}t^2} \right\rangle &= \frac{\mathrm{d}^2 \langle \boldsymbol{r}(t) \rangle}{\mathrm{d}t^2} \\ &= \langle -\boldsymbol{\nabla} V(r) + \boldsymbol{E}(t) \rangle , \end{aligned} \tag{4.2}$$

assuming a multiplicative potential (i.e. $[\hat{H}, V] = 0$) and applying the Ehrenfest theorem [98].

The computation of Eq. (4.1) requires the full wavefunction for the system of interest. While for single electron targets our method indeed provides this, for others we must work within the single active electron approximation. In many circumstances within strong field physics such a treatment is sufficient (see Chapter 2, for example). However, this is not the case for HHG. Recombination or, equivalently, its inverse of photoionisation, can be strongly influenced by multi-electron correlation particularly across and approaching thresholds [99]. As such, we look to account for its effect within our approach. Furthermore, it is worth explicitly stating that from this point onwards we will only be considering the spectrum in the polarisation direction z due to the pseudo-one-dimensional nature of the problem.

To do so, we make the ansatz that effect of correlation can be factorised our from the uncorrelated HHG acceleration such that

$$\langle P_z(\omega) \rangle \propto \rho_z(\omega) \int \mathrm{d}t \left\langle \frac{\mathrm{d}^2 z(t)}{\mathrm{d}t^2} \right\rangle_{\mathrm{SAE}} e^{-i\omega t} , \tag{4.3}$$

where $\rho_z(\omega)$ accounts for the correlated enhancement and the subscript SAE denotes computation under the single active electron approximation. The validity of such an ansatz was demonstrated by Morishita *et al.* [100] and underpins the quantitative

rescattering approach (QRS) [101, 102]. We further assume that this enhancement $\rho(\omega)$ is given by the ratio of photoionisation cross-sections in the polarisation direction computed with and without correlations,

$$\rho_z(\omega) = \sigma_z^{\text{corr.}}(\omega)/\sigma_z^{\text{uncorr.}}(\omega) \ . \tag{4.4}$$

For the uncorrelated cross-section we simply compute the transition amplitude between the Dirac-Hartree-Fock orbitals for initial and final states [103]. Doing so we are essentially taking the other electrons to be 'frozen' throughout the process. For the cross-section computed including the effects of electronic correlation our chosen method is the relativistic random phase approximation (RRPA) [104] due to its applicability for high Z targets such as Xe. Figure 4.2 depicts the direct and correlated photoionisation processes as included within the RRPA and we briefly outline the theory behind the method in Section 4.1.1.

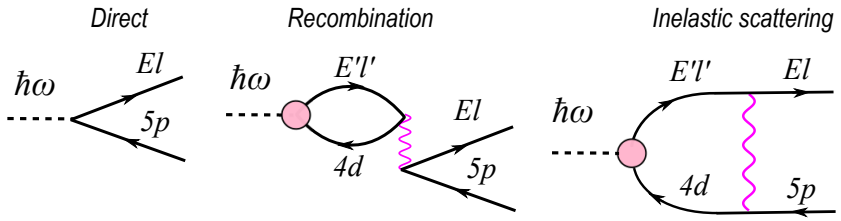

Figure 4.2: Graphical representation of the direct (left) and correlation (centre and right) photoionisation processes included in the RRPA. Straight lines with arrows to the right/left represent a photoelectron/hole. The dashed line depicts a photon and the wavy line represents the Coulomb interaction. The dashed circle indicates summation of direct and exchange correlation processes to infinite order. The arrow direction corresponds to photoionisation and is the reverse in the case of HHG.

For our single active electron TDSE computation, we choose model potentials as in Chapter 3 based on their appropriate asymptotic forms ($V(r) \to -1/r$ for $r \to \infty$ and $V(r) \to -Z/r$ for $r \to 0$), accuracy in reproducing experimental bound state energies, and Cooper minima positions. Namely, for Kr we use the potential described in [105]

$$V_{\text{Kr}}(r) = -\frac{1}{r}\left(1 + 6.42e^{-0.905r} + 28.58e^{-4.20r}\right) \ , \tag{4.5}$$

and for Xe the form of [51]

$$\begin{aligned} V_{\text{Xe}}(r) = -\frac{1}{r}\Bigg(1 + 53\Big(&0.89e^{-13.42r} + 0.11e^{-0.71r} \\ &+ r \quad 4.05e^{-6.20r} \\ &- r^2\ 33.18e^{-63.45r} \\ &+ r^3\ 16.15e^{-7.08r} \\ &+ r^4\ 15.67e^{-6.14r}\Big)\Bigg) \ . \end{aligned} \tag{4.6}$$

Finally, it should be noted that single atom theoretical spectra, as derived above, exhibit sharp oscillations over several orders of magnitude at an energy resolution unattainable by experiment. Consequently, for comparison, we apply the following Gaussian convolution to our raw data

$$\langle P_z^{\text{conv.}}(\omega)\rangle = \frac{\int_0^\infty \langle P_z(\omega')\rangle e^{-\sigma(\omega-\omega')^2} d\omega'}{\int_0^\infty e^{-\sigma(\omega-\omega')^2} d\omega'} \,, \tag{4.7}$$

with $\sigma = 0.01$. The effect of this convolution is demonstrated in Figure 4.3.

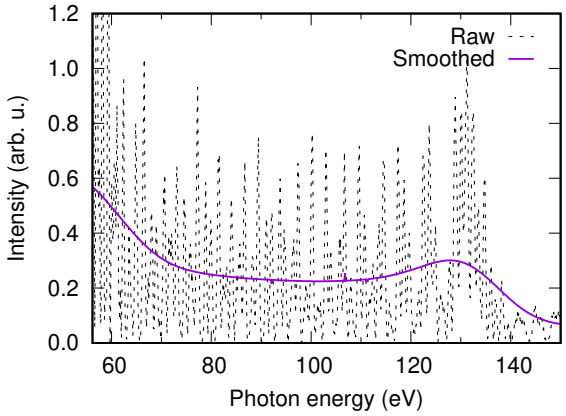

Figure 4.3: Comparison between the raw theoretical HHG spectrum (4.3) (dashed black line) and that smoothed via Gaussian convolution (4.7) (blue solid line). The spectra in particular are from the Kr computation described in Section 4.2.1.

4.1.1 Relativistic Random Phase Approximation (RRPA)

The random phase approximation (RPA) [106] is derived as an extension of the Hartee-Fock approximation for a many electron target to interaction with a weak-external field. To do so, the full time-dependant Hartree-Fock [107] equations are expanded in powers of the external field, and truncated at first order. From there, terms corresponding to doubly excited orbitals are neglected, an approximation thought reasonable for large systems such terms describing the interaction of many alternative pairs of excited particles have essentially 'random' coefficients, consequently nullifying their contribution [108]. It is interesting to note however, that the states neglected within the RPA introduce a Pauli violation associated error of order N^{-1} where N is the total number of atomic electrons [47].

The relativistic formulation (RRPA) [104] is derived from the time-dependent Dirac-Hartree-Fock equivalent. In which, the transition amplitude corresponding to ionisation by an external field of frequency ω is given by

$$T(\omega) = \sum_{i=1}^{N} \int \mathrm{d}^3 r \, \langle w_{i+}|\boldsymbol{\alpha}\cdot\boldsymbol{A}(\omega)|u_i\rangle + \langle u_i|\boldsymbol{\alpha}\cdot\boldsymbol{A}(\omega)|w_{i-}\rangle \,. \tag{4.8}$$

Here $|u_i\rangle$ and $|w_{i\pm}\rangle$ are the Dirac-Fock and field perturbed orbitals respectively,

$$\boldsymbol{\alpha} = \begin{pmatrix} \mathbf{0} & \boldsymbol{\sigma} \\ \boldsymbol{\sigma} & \mathbf{0} \end{pmatrix} \tag{4.9}$$

and $\boldsymbol{\sigma}$ are Pauli spin matrices [109]. It is this $T(\omega)$ amplitude which, squared, is proportional to the photoionisation cross-section at energy ω, and subsequently that which we take as the correlated component of our enhancement ratio (4.4).

4.2 Results

We now examine the applicability of our formulation to the long wavelength experiments of Shiner *et al.* [84, 110] and the two colour problem of Faccialà *et al.* [85, 86]. Both cases are strongly affected by electron correlation driven enhancement and increasingly test our ansatz with the complexity of the applied external field.

4.2.1 Single-colour

As the first test of our computational procedure we calculate the HHG spectrum of Kr. We do so as its spectra are not substantively affected by correlation enhancement due to no prominent resonances in the region of interest. The pulse (1.3) is a linearly polarised field of duration 8.8 fs FWHM in intensity of peak 1.8×10^{14} at 1800 nm. Figure 4.3 presents the raw result of our computation (4.3) contrasted against its convolution (4.7). This convolution is contrasted against experiment [84, 110] and an analogous R-matrix calculation [111] in the top frame of Figure 4.4. The agreement between each is generally favourable. In particular, our computation matches well the location of the spectral cutoff of the experimental spectra albeit with a marginally higher magnitude. All three datasets have approximately equal predictions for the Cooper minimum. We next calculate the HHG spectrum from Xe under identical conditions. In this case, the spectra are strongly enhanced across the so-called 'giant resonance' induced to the valence $5p$-shell by its correlation with the $4d$-shell [112]. Our results before and after RRPA enhancement are given in the bottom frame of Figure 4.4 and compared again with the experiment [84] and the R-matrix calculation [111]. Additionally we include the QRS 25 Torr dataset from Fig. 3(c) of [113] given for peak intensity 2×10^{14} W/cm^2. This latter approach includes macroscopic effects introducing dependencies on the focusing position and gas pressure. Of the QRS calculations presented [113], it is this which appears to have the best agreement with the Shiner experiment. Our reproduction of the giant resonance is an improvement over the R-matrix method. However, both of these

approaches exhibit a broader tail at high energies than that seen in the experiment. Conversely, the QRS method places the resonance well in line with the experiment but with an altogether sharper dependency.

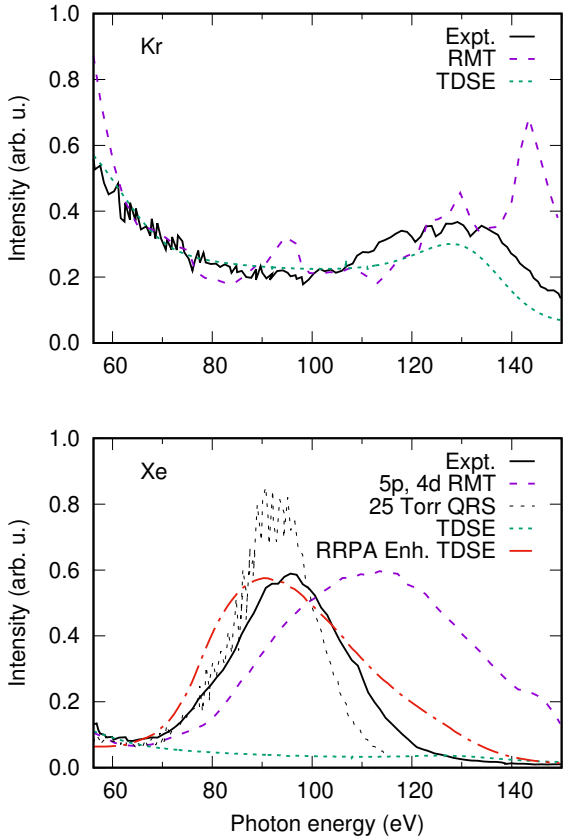

Figure 4.4: Top: The HHG spectrum of Kr from experiment [84] (black solid line), the R-matrix calculation [111] (blue sparse dashed line), and our present TDSE theory (green dense dashed line). Bottom: As above for Xe with the addition of our RRPA enhanced TDSE theory (red dash-dotted line) and QRS calculation [113] (black thin dashed line).

4.2.2 Two-colour

Having examined our approach applied to a strongly correlated problem involving an ordinary external field, we now look to calculate the two-colour HHG spectra of Xe [85]. To do so we sum two linearly polarised pulses of the form (1.3). The primary ω field corresponds to 1550 nm, is of peak intensity 7×10^{13} W/cm^2, and has FWHM duration of 8.8 fs with respect to this intensity. The secondary 2ω field, accordingly corresponding to 775 nm, has the same FWHM duration, phase χ and electric field strength 0.4 relative to the primary. The present TDSE calculated HHG spectra, both raw and enhanced by the RRPA $5p/4d$ intershell correlation, are displayed in the middle and bottom frames of Figure 4.5 respectively. They are drawn as two-dimensional (2D) false colour plots in the energy and relative phase χ coordinates. The top frame of Figure 4.5 exhibits the experiment as presented in

[86].

We find solid qualitative agreement between our results and that of the experiment and, as desired, applying the enhancement ratio appropriately magnifies the caustic in the cutoff region. The most notable difference is the differing phase at which the low-energy maxima occurs, being approximately $\chi = 0.75\pi$ in the experiment and our theory predicting closer to 0.10π below this. Additionally, the experiment exhibits a much stronger relative background across phases than what we see in our calculation. This being a feature similarly found in their comparison with time-dependent configuration interaction singles (TDCIS) based theory [85]. A more detailed comparison is made in Figure 4.6 where the phase maximum of the spectra shown in Figure 4.5 is traced ($\max_\chi \langle P_z^{\text{conv.}} \rangle$). On the top panel we display the TDSE calculation compared with the uncorrelated ($5p$ only) TDCIS theory. Here we find the observed trend to be essentially equivalent bar minor features. On the bottom panel comparison is made of between our RRPA enhanced spectra and the correlated TDCIS ($5p$, $4d$, $5s$) as well as the experiment. Again we find very solid agreement between all three datasets. Most notably, we did not find a noticeable disagreement between our calculation and the experiment around 63 eV photon energy which is visible in the TDCIS calculation.

4.3 Conclusions

We performed simulations of HHG spectra from Xe in both one- and two-colour fields from the numerical solution of the one-electron TDSE and account for the effects of intershell correlation as a ratio of photoionisation cross-sections. In both cases, we find solid agreement between our results and those of experiment and to either be an improvement, or equivalently accurate, to those of more elaborate theories. This is attributed to the equivalence of the recombination process in the production of HHG to the time reversal of photoionisation. Accordingly, we find the correlation effects to behave similarly, even when the dynamics is complicated significantly by the introduction of the secondary field. Such an observation suggests that further aspects of two-colour HHG production can be efficiently and effectively studied through the lens of correlated photoionisation. To this end, we will next apply our techniques to other atomic systems where the HHG process is enhanced by intershell correlation and giant resonances. One such system is atomic manganese where a giant autoionisation resonance due to transition from the $3p$ to a partially filled $3d$ shell enhances strongly photoionisation and photorecombination from the outer valence shell. This enhancement is recorded in the HHG spectrum accordingly [93].

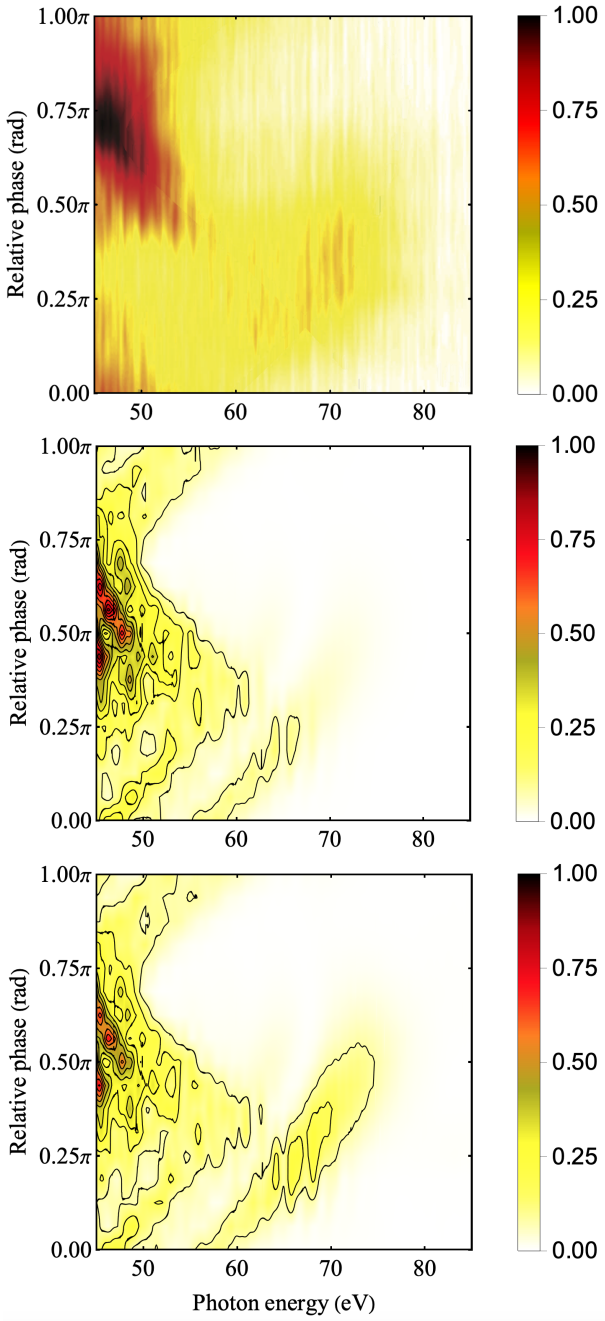

Figure 4.5: The HHG spectrum of Xe recorded as a function of the photon energy and the relative $\omega/2\omega$ phase χ. Top: Experimental spectra from [86]. Middle: Present TDSE calculation. Bottom: TDSE spectra enhanced by RRPA. Contours connect regions of equal intensity in intervals of approximately 7%.

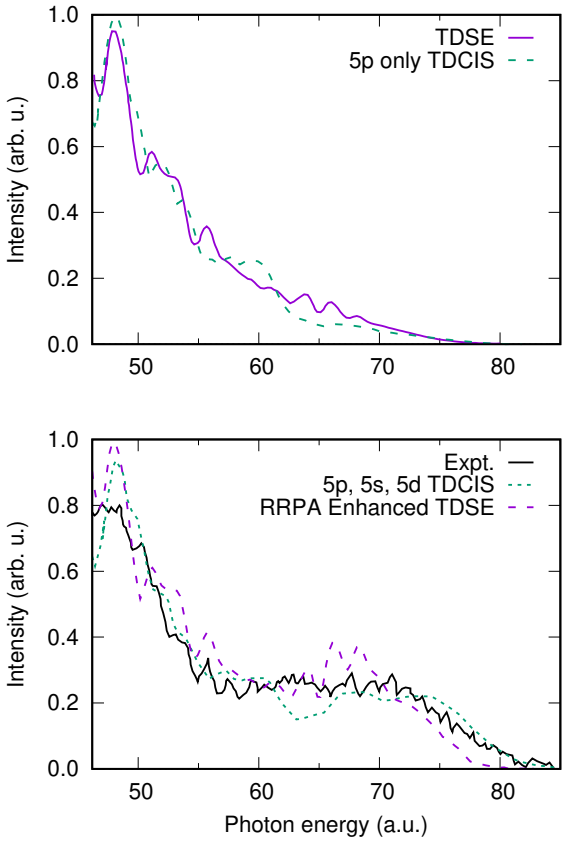

Figure 4.6: The maximum HHG yield of Xe with phase for a given photon energy ($\max_\chi \langle P_z^{\text{conv.}} \rangle$). Top: Our raw TDSE compared with the $5p$ only TDCIS theory [85]. Bottom: Enhanced TDSE result compared with the correlated TDCIS theory and experimental measurements [85].

Chapter 5

State-resolved acceleration of neutrals

This chapter is based on the following publication:

> A. W. Bray, U. Eichmann, S. Patchkovskii, "Dissecting strong-field excitation dynamics with atomic-momentum spectroscopy," Phys. Rev. Lett., *Submitted*.

Somewhat counterintuitively, linearly polarised fields with increasingly high intensities, rather than completely ionising the target atom, leads to atomic stabilisation [114, 115]. This effect at high frequencies has been interpreted in terms of the Kramers-Henneberger picture [4, 116] with the electron moving in a binding time-averaged effective potential, leaving the target in a complex mixture of Rydberg states.

This same phenomena has been observed in the context of today's IR pulsed laser systems via a process termed *frustrated tunnelling ionisation* [117]. In which case, the Rydberg state distribution was found to scale as $\langle n \rangle \propto \sqrt{E}/\omega$, consistent with the maximal excursion distance of the electron in the field $r_{\max} = E^2/\omega$ and the radial expectation of said states $\langle r_{\mathrm{Ryd}} \rangle \propto n^2$. However, an unexpected observation was the large (up to $10^{14}g$) acceleration of the neutral species produced [118]. Said acceleration was present only for those atoms at significant distance from the focal centre and, consequently, was attributed to the ponderomotive force from the large field gradient in this region. Convincing theoretical grounding exists for the total yields across a wide range of intensities [119], yet is lacking in a vital aspect, state resolution.

The acceleration of neutrals has two promising applications conditional on its state dependency. If the acceleration is widely universal, of particular interest if applicable to the ground state, then the process would represent an effective mechanism for their spatial manipulation. Instead, if there is large dispersion across electronic states, then via this mechanism one may design velocity selective gratings

for specific Rydberg states.

The remainder of this chapter is dedicated to the detailing and applying a theoretical method suitable for this very problem. Namely, the acceleration of the specific electronic states generated upon application of intense, linearly polarised, and non-spatially-uniform fields.

5.1 Non-dipole laser fields

The small length scales of atomic physics problems typically allow for external laser fields to be treated as spatially uniform (see Section 1.2.1). Nonetheless, the reality is such the fields involved in strong field problems do have spatial dependences. For a focussed laser beam, the lowest order solution for a sufficiently long pulse is of the form

$$\begin{aligned}\boldsymbol{A}(\boldsymbol{r},t) = A_0 \frac{w_0}{w(x)} \exp\left(-\frac{y^2+z^2}{w(x)^2} - \gamma t^2\right) \\ \times \cos\left[\omega t - kx - k\frac{y^2+z^2}{2R(x)} + \arctan(x/x_R) + \phi\right] \hat{\boldsymbol{z}}\end{aligned} \tag{5.1}$$

$$w(x) = w_0\sqrt{1+(x/x_R)^2} \tag{5.2}$$

$$R(x) = x + x_R^2/x\ , \tag{5.3}$$

known as a Gaussian mode [120], or equivalently, the transverse electromagnetic mode TEM_{00} [121]. Here $x_R = kw_0^2/2$ is the Rayleigh length, and w_0 is the beam waist which characterises the degree to which the beam is focused. γ, as has previously been denoted α (Eq. (1.6)), is the parameter that determines the Gaussian FWHM of the pulse intensity in time, and ϕ is again the carrier envelope phase (CEP). Without loss of generality, we have chosen x as the propagation, y as the transverse, and z as the polarisation directions respectively. Non-linear polarisation is achieved through superposition of several such fields.

As previously mentioned, typically in atomic physics problems this spatial dependence can be neglected due to the small length scales involved. However, an exception occurs when the physics itself stems from this dependency. This is true in our case as the observed ponderomotive acceleration is a result of the large field gradients experienced at distance far from the beam centre. Hence, for this problem we require the full treatment of the fields spatial dependency. In particular, we will consider a pulse of the form (5.1) at $\lambda = 800$ nm, peak intensity 1×10^{15} W/cm^2, beam waist $w_0 = 2\lambda$, and a temporal FWHM in intensity of 5.32 fs.

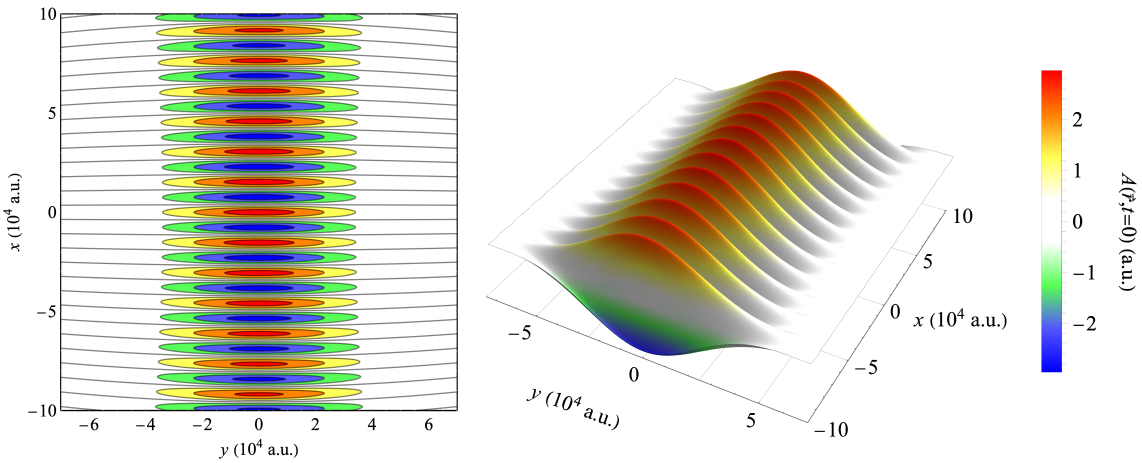

Figure 5.1: Representation of a Gaussian pulse (5.1) (x-propagation, z-polarization) at $t = 0$ along the $z = 0$ plane as contours (left) and shaded 3D surface (right). Pulse parameters are wavelength $\lambda = 800$ nm, peak intensity 1×10^{15} W/cm^2, beam waist $w_0 = 2\lambda$, and a FWHM in intensity of 5.32 fs.

5.2 Classical prediction

We now wish to derive the final velocity due to the ponderomotive force of an atom with polarisability α when exposed to the above non-uniform field (5.1). In the general case, we write Newton's law as the following:

$$M\frac{\partial \boldsymbol{v}}{\partial t} = -\boldsymbol{\nabla}_r\left(-\frac{E^2(\boldsymbol{r},t)}{2}\alpha\right) \ . \tag{5.4}$$

Letting t_b represent the time at which this particle is 'born' we can write Eq. (5.4) in integral form

$$\boldsymbol{v} = \frac{\alpha}{2M}\int_{t_b}^{\infty} \boldsymbol{\nabla}_r E^2(\boldsymbol{r},t)\ \mathrm{d}t \ . \tag{5.5}$$

Restricting to our specific field (x-propagation, z-polarisation) and the initial condition $x_0 = 0, z_0 = 0$ we have for the velocity in the transverse direction

$$v_y = -\frac{2y\alpha}{Mw_0^2}\int_{t_b}^{\infty} E^2(y,t)\ \mathrm{d}t \ . \tag{5.6}$$

We now make the assumption that the position of the atom does not change on the time scale of the pulse. This allows us to treat $y = y_0$ as a constant with respect to the integral and to write for the final transverse velocity

$$v_y = -\alpha A_0^2 \frac{2y_0}{Mw_0^2} e^{-2y_0^2/w_0^2}\int_{t_b}^{\infty} \left(\omega\sin(\omega t) + 2t\gamma\cos(\omega t)\right)^2 e^{-2\gamma t^2}\mathrm{d}t \ . \tag{5.7}$$

Finally, we recognise that the cosine term stems from the finite width of the pulse and for $\gamma \ll \omega^2$ its contribution is negligible. This is indeed the case for our pulse. Additionally, we recognise that Eq. (5.7) is a strictly increasing function as $t_b \to -\infty$

allowing us to compute an upper bound of

$$v_y^{\max} = -\alpha E_0^2 \frac{y_0}{m w_0^2} e^{-2y_0^2/w_0^2} \sqrt{\frac{\pi}{2\gamma}} \,. \tag{5.8}$$

Taking $\alpha_{\mathrm{f}} = -1/\omega^2$ as the polarisability of a free electron (5.8) evaluates to approximately 24.3 m s^{-1} compared to numeric solution of (5.6) 24.4 m s^{-1} thus validating the applicability of our assumptions. Instead, taking $\alpha_0 = 9/2$ as the polarisability of the ground state of hydrogen (5.8) yields approximately -0.4 ms^{-1}.

5.2.1 Reconstructing Rydberg ionisation times and ground state effective polarisability

Armed with Eq. (5.5) there are two further interesting comparisons we may make, in addition to the upper bounds on v_y computed above. Firstly, if we assume that each Rydberg produced has approximately the polarisability of a free electron, we can use our TDSE resultant v_y to solve Eq. (5.5) in reverse to yield the excitation time t_b. It must be stated however that as the polarisability is a cycle averaged quantity that determining t_b in this way cannot provide meaningful sub-cycle resolution. Secondly, the ground state does not have a birth time per se, rather it exists for all time $t_b = -\infty$. As such we may instead use Eq. (5.5) to compute the effective polarisability of this state by comparison with our TDSE value.

5.3 TDSE solution

Here we wish to formulate a Hamiltonian suitable for this problem from which we may construct our propagator. For its full derivation please see Appendix A.3.

We begin with the general minimal-coupling two-body expression

$$\begin{aligned}\hat{H} = &\frac{1}{2m_1}\left(\hat{p}_{r_1} - q_1 \boldsymbol{A}(\boldsymbol{r}_1)\right)^2 + \frac{1}{2m_2}\left(\hat{p}_{r_2} - q_2 \boldsymbol{A}(\boldsymbol{r}_2)\right)^2 \\ &+ v(\boldsymbol{r}_1 - \boldsymbol{r}_2) + u\left(\frac{m_1}{M}\boldsymbol{r}_1 + \frac{m_2}{M}\boldsymbol{r}_2\right)\end{aligned} \tag{5.9}$$

containing terms u and v representing potentials associated with the inter-particle separation and the centre of mass (c.o.m.) position. However, as the external field has no spherical symmetry, the solution of (5.9) is a truly 6-dimensional problem and is accordingly numerically challenging. Nonetheless, there are other properties that we may make use of. Namely:

1. $\boldsymbol{X} = \boldsymbol{r}_1 - \boldsymbol{r}_2 \,, \quad \boldsymbol{R} = \boldsymbol{r}_1 m_1/M + \boldsymbol{r}_2 m_2/M$

   We shift to c.o.m. coordinates.

2. $\mu = m_1 \ll m_2 = M$

Assume the mass of the nucleus is much greater than the electron.

3. $q_2 = -q_1 = -q$

   We say the two original particles are of equal and opposite charges.

4. $\boldsymbol{A}(\boldsymbol{X} + \boldsymbol{R}) \approx \boldsymbol{A}(\boldsymbol{X}) + \boldsymbol{\nabla}_R \boldsymbol{A}(\boldsymbol{X}) \cdot \boldsymbol{R}$

   Approximate the field as linear in $\boldsymbol{R}$ about $\boldsymbol{X}$ as $R \ll X$.

5. Drop terms of order μ/M or below in the reduced mass Hamiltonian $\hat{H}_X$.

6. Drop linear field correction term in the c.o.m. Hamiltonian $\hat{H}_R$.

   This essentially assumes that the dynamics of the c.o.m. come entirely from its coupling to the reduced mass particle. The constant field interaction term naturally cancels as the c.o.m. particle has no charge to zeroth order.

Having made these assumptions we may now write (5.9) as

$$\hat{H} = \hat{H}_X + \hat{H}_R \,, \qquad \hat{H}_X = \frac{1}{2\mu} \left(\hat{p}_X - q\boldsymbol{A}(\boldsymbol{R} + \boldsymbol{X})\right)^2 + v(\boldsymbol{X}) \tag{5.10}$$

$$\hat{H}_R = \frac{1}{2M}\hat{p}_R^2 + u(\boldsymbol{R}) \,, \tag{5.11}$$

and seek solutions in the close-coupling form

$$\Psi(\boldsymbol{X}, \boldsymbol{R}, t) = \sum_n \varphi_n(\boldsymbol{X}, t)\chi_n(\boldsymbol{R}) \,, \tag{5.12}$$

where the $\chi_n(\boldsymbol{R})$ are the time-independent eigenfunctions of $\hat{H}_R$. We now choose $u(\boldsymbol{R})$ as the harmonic oscillator potential $\hat{x}_R^2 k/2$ such that our solutions $\chi_n(\boldsymbol{R})$ of energy ϵ_n and all of their subsequent matrix elements (see Tables A.1 and A.2) are known analytically. In doing so, we must be careful that our choice of k is such that the trapping potential is of negligible influence in comparison to the remaining aspects of the physics. On the other hand however, we wish this potential to be of sufficient depth such that only the ground state and first order solutions for each Cartesian direction are populated. As a result of our investigations we find a value of $k = 10^{-4}$ to be satisfactory. The key physical question however is ensuring the c.o.m. motion of the target, which is characterized by a finite temperature, is appropriately treated by our choice of $u(\boldsymbol{R})$. In a gas, the position of the c.o.m. is determined to within the thermal de Broglie wavelength and is therefore best represented by a finite, compact wavepacket. As long as the de Broglie wavelength remains small compared to the laser wavelength, the exact shape and precise dimensions of this wavepacket are not material for the outcome, and as such, our choice is an appropriate one. Restricting ourselves to this regime, we have a Schrödinger

equation of the form

$$i\frac{\partial\varphi_n}{\partial t} = (\hat{h}_0 + \epsilon_n)\varphi_n + \sum_m \hat{h}_{nm}\varphi_m \qquad \text{for} \qquad n, m \in \{0, x, y, z\} \ , \tag{5.13}$$

where $\hat{h}_0$ and $\hat{h}_{nm}$ are complicated functionals of the field the reduced mass momentum operator $\hat{p}_X$, and harmonic oscillator matrix elements, but despite their complexity are straightforward to compute. For their exact forms please see Appendix A.3. Finally, we have formulated our problem (5.13) in terms of a system of four coupled three-dimensional equations, that may now be solved at a computational cost comparable with that involved in a fixed-nuclei electronic TDSE code.

5.3.1 Conditional velocity expectation

Presuming we have the solution $|\Psi\rangle$ of (5.13) at a time for which the pulse is gone, let us compute the experimental observable we are interested in: the c.o.m. velocity for a given electronic state. We begin with the expectation value of the final momentum given by

$$\langle\hat{p}_R\rangle = \langle\Psi|\hat{p}_R|\Psi\rangle = \sum_{nm}\langle\varphi_n|\varphi_m\rangle\boldsymbol{p}_{nm} \tag{5.14}$$

where

$$\boldsymbol{p}_{nm} = \langle\chi_n|\hat{p}_R|\chi_m\rangle \ . \tag{5.15}$$

The values of (5.15) are given in Table A.2. For the state-resolved velocity, we insert the identity

$$\mathbb{1} = \sum\!\!\!\!\!\!\int_f |\varphi_f\rangle\langle\varphi_f| \ , \tag{5.16}$$

divide by the c.o.m. mass, and look at the contribution from a single bound state $|\varphi_f\rangle$

$$\langle\hat{v}_{R,f}\rangle = \frac{1}{M}\sum_{nm}\langle\varphi_n|\varphi_f\rangle\langle\varphi_f|\varphi_m\rangle\boldsymbol{p}_{nm} \ . \tag{5.17}$$

This quantity is the contribution to the total velocity expectation from the given state. If, instead, we want the velocity *conditional* on having observed the system in said state, by Lüders' rule [122], we must normalise by the probability to be in this state,

$$\langle\hat{v}_{R,\text{cond. }f}\rangle = \frac{1}{M}\frac{\sum_{nm}\langle\varphi_n|\varphi_f\rangle\langle\varphi_f|\varphi_m\rangle\boldsymbol{p}_{nm}}{\sum_n|\langle\varphi_f|\varphi_n\rangle|^2} \ . \tag{5.18}$$

This has been argued (though with some contention [123, 124]) to be the quantum analogue of conditional probability

$$P(A|B) = \frac{P(A \cap B)}{P(B)} \ . \tag{5.19}$$

5.4 Results

In this section we present the results of our computations of centre of mass velocity conditional expectations (5.18) for the Gaussian pulse described in Section 5.1. Using these results we compute the ionisation times t_b for each excited state produced and the effective ground state polarisability as described in Section 5.2.1.

Before said presentation, however, there are several considerations that merit discussion. Firstly, we will restrict our discussion to states with magnetic quantum number $m = 0$. However, as this is a fully non-dipole treatment we indeed do find non-zero $m \pm 1$ (2) populations. However, they are four (eight) orders of magnitude smaller than for $m = 0$, a scaling consistent with the lowest-order magnetic transition probabilities. Secondly, we examine displacements from the beam centre exclusively along the y-axis. Doing so disentangles the three mechanisms for momentum transfer under such a scenario: the radiation pressure (x, propagation), ponderomotive (y, transverse), and asymmetry (z, polarisation). The velocity due to radiation pressure is uninteresting however, as it is determined entirely by the energy difference between the ground and excited states $v_x = (E_n - E_0)/Mc$. Furthermore, the asymmetry acceleration is approximately zero within numeric accuracy. As such, our analysis is entirely focused on the ponderomotive/transverse velocity. Accordingly, our displacement of choice is $y_0 = w_0/2$ and it is for this position that said velocity is maximised (inferred from Eq. (5.4)). Finally, in problems involving strong field excitation the effect of channel closings and associated resonances are highly prominent [119]. A channel closing occurs when the intensity rises to the point where a process involving n-photons of the laser frequency becomes insufficient to cause ionisation. For such a process to ionise the target we require $n\omega > I_p + U_p$, $U_p \propto I$. As such, with increasing intensity the n-photon absorption channel closes and instead comes into resonance with the Rydberg pseudo-continuum, enhancing the production of these reaction products. For an 800 nm laser this corresponds to a channel closing every 26 TW/cm^2. Accordingly, we average our result across 7 displacements corresponding to 12 TW/cm^2 steps along the Gaussian intensity profile centred about $w_0/2$. Doing so, we effectively suppress the resonance contributions which are highly sensitive to the intensity.

Our choice of Cartesian grid in performing the calculations is also worthily of mention. As we are interested in the species that remain bound, we do not need to prevent ionised flux from reaching the box boundaries. Nonetheless, the n species

distribution at 10^{15} W/cm^2 is expected to peak at approximately $n = 7$ [117], and with Rydberg radial expectation values scaling as n^2, this quickly proves to be a restriction. Furthermore, to support these states, we additionally need to account for the field induced oscillation of magnitude A_0/ω. An advantage, however, is that this oscillation occurs in the direction of polarisation (z) and accordingly does not need to be accounted for in the remaining propagation (x) and transverse (y) directions. For the radial box we have chosen $\{x \in \pm 78.6, y \in \pm 78.6, z \in \pm 152.1\}$, we are only able to fully support states up to $n \leq 6$ and, accordingly, it is for these that we present results.

5.4.1 Transverse velocities

The volume-averaged numerical results at this point are illustrated in Figure 5.2. The local peak intensity of the field is $\approx 6.1 \times 10^{14}$ W/cm^2. The ionization is in the saturation regime, with $\approx 9\%$ of the population surviving in the $1s$ ground state after the pulse. Additionally, $\approx 2.4\%$ of the atoms are excited to Rydberg states with $n \leq 6$. Although our simulation volume does not allow an accurate determination of excitation probabilities for higher Rydberg states, we estimate that at least 2% of the atoms are left in Rydberg states with $n \geq 7$. For all electronic states in Figure 5.2c other than the ground state, the final transverse velocities are in the range of 12 to 20 m s^{-1}.

5.4.2 Reconstructed Rydberg ionisation times

As described in Section 5.2.1, by assuming free-electron-like polarisability we may solve Eq. (5.5) for t_b to yield the excitation time. The results for the volume-averaged excitation time reconstruction are presented in Figure 5.3. In nearly all cases, excited states are formed before the peak of the envelope, with two main clusters at approximately -0.7 ($2p$, $3s$, $3d$, $4d$, $5s$, $5d$, $5f$, $5g$, $6d$, $6g$, and $6h$) and -1.7 fs ($3p$, $4s$, $4p$, $5p$, $6s$, $6p$, $6f$). Interestingly, both clusters gravitate towards the zeros of the vector-potential, near the peaks of the electric field. These times of birth are consistent with the expectations from the semi-classical frustrated tunneling model [22]. Intriguingly, two of the excited states ($2s$ and $4f$) appear to be preferentially formed near the peak of the vector-potential, respectively at -0.2 and $+0.2$ fs. These times of birth, and the broad spread of the times of birth within the two clusters in Figure 5.4 would seem to indicate that the multi-photon excitation mechanism is also active. This observation is consistent with the value of the Keldysh parameter, 0.4, indicating dynamics in a regime intermediate between tunnelling and multi-photon transitions.

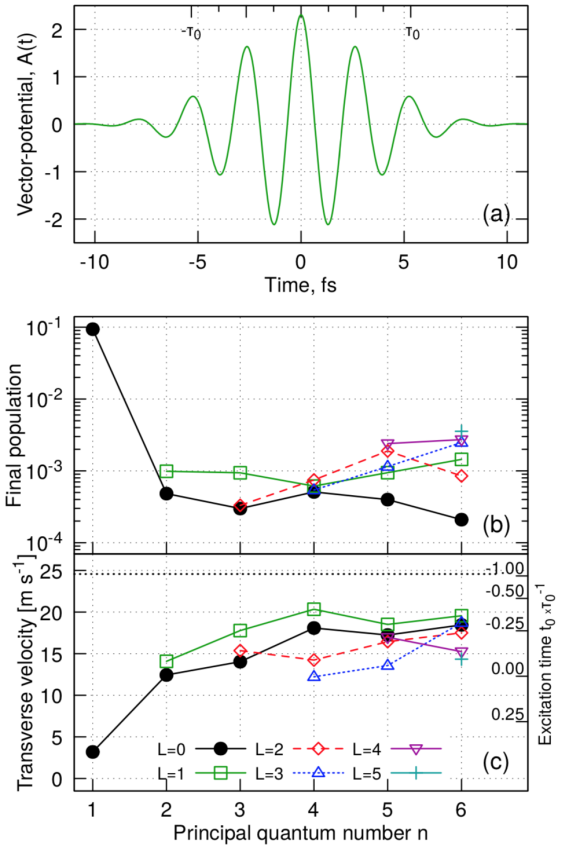

Figure 5.2: Hydrogen atom initially at the half-waist position. The results are volume-averaged about the Cartesian point $(0,\ w_0/2 \pm 648,\ 0)$. The local peak intensity is $\approx 6 \times 10^{14}$ W/cm^2. (a) Vector-potential at the initial position as a function of time. The upper horizontal axis gives the fraction of the pulse duration τ_0. (b) Population of the individual $m = 0$ bound states after the end of the pulse. (c) Final c.o.m. velocity in the outward transverse direction in meters per second (1 a.u. $\approx 2.19 \times 10^6$ m s^{-1}). The right vertical axis gives the time when a particle with free-electron polarisability needs to enter the field to reach the observed transverse velocity (Eq. (5.8)). Final velocities above the dotted horizontal line cannot be reached by a free-electron-like particle. The connecting lines in panels (b,c) are only a guide for the eye.

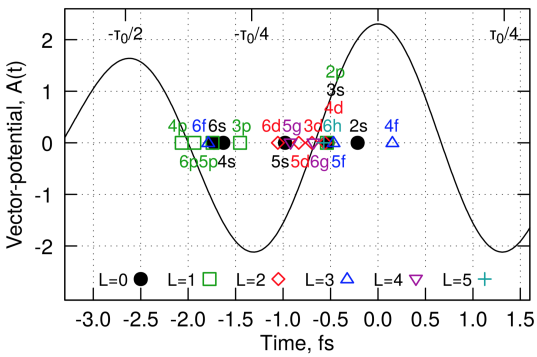

Figure 5.3: Reconstructed excitation times for the c.o.m. velocity spectra averaged over $\pm 648\ a_0$ about the half-waist position (See text and Figure 5.2 for the raw data). The vector potential at the Cartesian point $(0,\ w_0/2,\ 0)$ is given by the black solid line. Peak of the envelope is at the time zero.

5.4.3 Effective ground state polarisability

One result seen in Figure 5.2c, which so far has not been remarked upon, is the behaviour of the $1s$ ground state. For the laser pulse in Figure 5.2a, it is weak-field seeking, reaching the final outward velocity of ≈ 3.2 m s^{-1}. We additionally find the low-field-seeking behaviour of the $1s$ state persists for other field parameters as well. The final $1s$ velocity is also insensitive to channel-closing effects, indicating that it arises due to adiabatic modification of the ground state, rather than via transient population of high-Rydberg states. Because the $1s$ state existed before the arrival of the pulse, $t_b \to -\infty$, we solve Eq. (5.5) for the effective polarisability α_{eff}. We present α_{eff} as a function of the peak intensity of the laser pulse, for the same spatio-temporal pulse profile as used in Figure 5.2. The results for I_0 in the range of 0.5 to 20×10^{14} W/cm^2 are collected in Figure 5.4. At lower intensities, the numerical accuracy is insufficient to determine the final c.o.m. velocity, while at higher intensities the survival probability becomes too low. In the entire range of the intensities, the effective polarisability is negative, as opposed to $+9/2$ expected for $1s$ in a weak field. At higher intensities, the effective polarisability becomes comparable to the free-electron value (≈ -308 at this laser frequency). This indicates a remarkable, field-induced modification of the electronic structure of the ground state, characteristic of entering the Kramers-Henneberger regime [4]. Observation of Kramers-Henneberger regime for an atomic ground state in strong, low-frequency fields has been long sought after, with no unambiguous detection thus far [125].

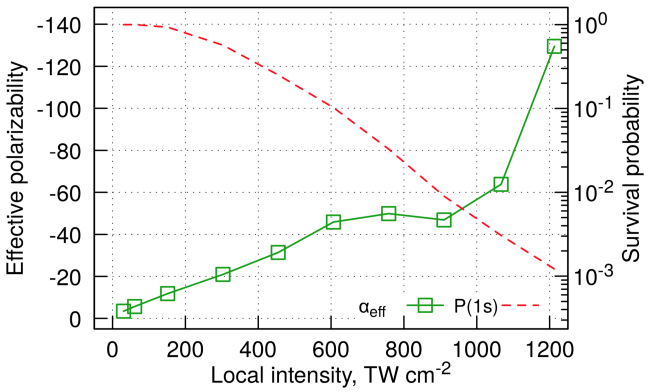

Figure 5.4: Effective polarisability α_{eff} (green solid line; left vertical axis) and survival probability (red dashed line; right vertical axis) of the $1s$ ground state. The spatio-temporal field profile is the same as in Figure 5.2. The peak intensity I_0 varies from 0.5 to 20×10^{14} W/cm^2. The horizontal axis shows the local peak intensity at the initial, half-waist position of the atom ($0.607 \times I_0$). These results are not volume-averaged as the ground state does not exhibit channel closing induced resonances.

5.5 Conclusions

We have developed a computationally tractable quantum mechanical approach to correlations between c.o.m. motion and internal electronic dynamics in strong, non-uniform laser fields. Using the technique, we demonstrate that the final c.o.m. velocity is sensitive to the internal excitation dynamics. In particular, the transverse ponderomotive velocity is determined by the total time the excited state spends in the field. In the absence of resonances, it yields a measurement of the preferential time of excitation. This procedure is robust to limited volume averaging, and can be applied for different CEP values, for longer pulses, and for non-paraxial beams. Finally, we demonstrate an unambiguous signature of the atomic ground state entering the Kramers-Henneberger regime in strong, low-frequency fields, which has been long sought-for. Taken together, our results suggest that c.o.m.-velocity spectroscopy is a powerful, and so far overlooked tool for understanding strong field bound-state electronic dynamics on their natural timescale.

Appendix A

Derivations

A.1 Pulse intensity

The Poynting vector ($\boldsymbol{S} = \boldsymbol{E} \times \boldsymbol{B}$ in vacuum) is the energy flux density of a given electromagnetic field. The magnitude of its time average gives the intensity

$$\begin{aligned} I &= |\langle \boldsymbol{S} \rangle| \\ &= \frac{1}{8\pi} |\boldsymbol{E}|^2 \end{aligned} \tag{A.1}$$

for a freely propagating sinusoidal field. Though note that this factor of $1/8\pi$ is typically absorbed into the atomic unit of intensity (see Eq. (A.5)) and as such in the same system of units simply $I = |\boldsymbol{E}|^2$. For two orthogonal infinite sinusoidal electric fields of amplitude $E_0/\sqrt{1+\epsilon^2}$ and $\epsilon E_0/\sqrt{1+\epsilon^2}$ the total intensity is simply their sum and is given by

$$\begin{aligned} I &= \frac{E_0^2}{1+\epsilon^2}\left(1+\epsilon^2\right) \\ &= E_0^2 \, . \end{aligned} \tag{A.2}$$

For a finite duration pulse we instead define the instantaneous intensity

$$I(t) = E(t)^2 \tag{A.3}$$

of which the peak is given by

$$\begin{aligned} I &= \max_t I(t) \\ &= E_0^2 \, . \end{aligned} \tag{A.4}$$

It is this quantity that is most commonly quoted simply as the 'intensity' of a given laser pulse.

For conversion to SI units recall that the atomic unit of intensity is given by the following

$$\begin{aligned} I_0 &= (E_h/(ea_0))^2 \frac{e^2}{8\pi\alpha\hbar} \\ &\approx 3.51 \times 10^{16}\ \mathrm{W/cm^2}\ . \end{aligned} \tag{A.5}$$

A.2 Gaussian full-width-half-maximum

We wish to know the relation between the full-width-half-maximum w of intensity and the parameter α for a Gaussian pulse of the form

$$A(t) = \exp(-\alpha t^2)\cos(\omega t)\ . \tag{A.6}$$

For this we need the upper bound of the instantaneous intensity which is related via

$$\begin{aligned} I &= E^2 \\ &= (-\partial A/\partial t)^2 \\ &= \Big(\exp(-\alpha t^2)\left[2t\alpha\cos(\omega t) + \omega\sin(\omega t)\right]\Big)^2 \\ &\leq \exp(-2\alpha t^2)(4t^2\alpha^2 + \omega^2)\ . \end{aligned} \tag{A.7}$$

Where we have used $(a\cos(x) + b\sin(x))^2 \leq a^2 + b^2$. At $t = 0$ Eq. (A.7) takes the value of ω^2. By definition we have that for $t = w/2$ it reaches half of this value, i.e.

$$\begin{aligned} \omega^2/2 &= \exp(-\alpha w^2/2)(w^2\alpha^2 + \omega^2) \\ \implies \qquad \alpha &= \frac{2}{w^2}\left[\ln 2 + \ln(1 + (w\alpha/\omega)^2\right]\ . \end{aligned} \tag{A.8}$$

Essentially our desired α is such that taking the RHS of (A.8) as a function and applying it leaves its value unchanged. Defining the sequence

$$\alpha_{n+1} = \frac{2}{w^2}\left[\ln 2 + \ln(1 + (w\alpha_n/\omega)^2)\right] \tag{A.9}$$

$$\alpha_0 = \frac{2\ln 2}{w^2} \tag{A.10}$$

we find its limit to rapidly converge to this value

$$\alpha = \lim_{n\to\infty} \alpha_n\ . \tag{A.11}$$

This same result is reached regardless of the sinusoid chosen in (A.6) or by addition of further orthogonal components and as such is applicable for the form (1.3).

A.3 Hamiltonian for acceleration of neutrals

Beginning again with the general minimal-coupling two-body expression

$$\hat{H} = \frac{1}{2m_1}\left(\hat{p}_{r_1} - q_1\boldsymbol{A}(\boldsymbol{r}_1)\right)^2 + \frac{1}{2m_2}\left(\hat{p}_{r_2} - q_2\boldsymbol{A}(\boldsymbol{r}_2)\right)^2 + v(\boldsymbol{r}_1 - \boldsymbol{r}_2) + u\left(\frac{m_1}{M}\boldsymbol{r}_1 + \frac{m_2}{M}\boldsymbol{r}_2\right) \tag{A.12}$$

we find by making the shift to c.o.m. coordinates

$$\boldsymbol{X} = \boldsymbol{r}_1 - \boldsymbol{r}_2 \ , \quad \boldsymbol{R} = \boldsymbol{r}_1 m_1/M + \boldsymbol{r}_2 m_2/M \ , \tag{A.13}$$

yields the expression

$$\begin{aligned}\hat{H} = {} & \frac{1}{2\mu}\hat{p}_X^2 - \left(\frac{1}{m_1}\boldsymbol{A}_1 - \frac{1}{m_2}\boldsymbol{A}_2\right)\cdot\hat{p}_X + \frac{1}{2m_1}A_1^2 + \frac{1}{2m_2}A_2^2 + v(\boldsymbol{X}) \\ & + \frac{1}{2M}\hat{p}_R^2 - \frac{1}{M}\left(\boldsymbol{A}_1 + \boldsymbol{A}_2\right)\cdot\hat{p}_R + u(\boldsymbol{R}) - \frac{1}{\mu}R_a\left(\boldsymbol{A}_1^{(a)} + \boldsymbol{A}_2^{(a)}\right)\cdot\hat{p}_X \\ & - R_a\left(\frac{1}{m_2}\boldsymbol{A}_1^{(a)} - \frac{1}{m_1}\boldsymbol{A}_2^{(a)}\right)\cdot\hat{p}_R + \frac{1}{\mu}\left(\boldsymbol{A}_1\cdot\boldsymbol{A}_1^{(a)} - \boldsymbol{A}_2\cdot\boldsymbol{A}_2^{(a)}\right) \\ & + \frac{1}{2\mu}R_aR_b\left(\frac{M}{m_2}\boldsymbol{A}_1^{(a)}\cdot\boldsymbol{A}_1^{(b)} + \frac{M}{m_1}\boldsymbol{A}_2^{(a)}\cdot\boldsymbol{A}_2^{(b)}\right)\end{aligned} \tag{A.14}$$

where repeated indexes $a, b \in \{x, y, z\}$ are summed over, we have used the shorthand

$$\boldsymbol{A}_1 = q_1\boldsymbol{A}\left(\frac{m_2}{M}\boldsymbol{X}\right) \tag{A.15}$$

$$\boldsymbol{A}_2 = q_2\boldsymbol{A}\left(-\frac{m_1}{M}\boldsymbol{X}\right) \tag{A.16}$$

$$\boldsymbol{A}^{(b)} = \frac{\partial}{\partial X_b}\boldsymbol{A} \ , \tag{A.17}$$

and assumed the field is both transverse $\boldsymbol{\nabla}\cdot\boldsymbol{A} = 0$, and can be approximated as linear in $\boldsymbol{R}$ about $\boldsymbol{X}$. We then take $q_1 = -q_2 = -q$, drop terms of order μ/M or smaller, and the field coupling term in $\hat{p}_R$ to write

$$\hat{H} = \frac{1}{2\mu}\left(\hat{p}_X - q\left(\boldsymbol{A} + \boldsymbol{A}^{(a)}R_a\right)\right)^2 + v(\boldsymbol{X}) + \frac{1}{2M}\hat{p}_R^2 + u(\boldsymbol{R}) \ . \tag{A.18}$$

We have confirmed that dropping such terms yields numerically equivalent results for our problem as the full expression Eq. (A.14). This is due to the short (sub-picosecond) and moderately-intense IR fields leading to c.o.m. displacements small compared to both the characteristic electron excursion and the laser-field wavelength. As previously mentioned with this Hamiltonian under such small c.o.m. displacements we can seek a close-coupling solution of the form

$$\Psi(\boldsymbol{X}, \boldsymbol{R}, t) = \sum_n \varphi_n(\boldsymbol{X}, t)\chi_n(\boldsymbol{R}) \ , \tag{A.19}$$

taking $n \in \{0, x, y, z\}$. Under this ansatz we seek solutions to the set of PDEs

$$i\frac{\partial}{\partial t}\varphi_n = \left(\hat{h}_0 + \epsilon_n\right)\varphi_n + \sum_m \hat{h}_{nm}\varphi_m \qquad n, m \in \{0, x, y, z\}\ , \tag{A.20}$$

$$\hat{h}_0 = \frac{1}{2\mu}\hat{p}_X^2 + v - \frac{q}{\mu}\boldsymbol{A}\cdot\hat{p}_X + \frac{q^2}{2\mu}A^2 \tag{A.21}$$

$$\hat{h}_{nm} = \boldsymbol{\eta}_{nm}\cdot\hat{p}_X + \kappa_{nm} \tag{A.22}$$

$$\boldsymbol{\eta}_{nm} = -\frac{q}{\mu}\boldsymbol{A}^{(a)}\langle\chi_n|R_a|\chi_m\rangle \tag{A.23}$$

$$\kappa_{nm} = \frac{q^2}{2\mu}\left[\left(A^2\right)^{(a)}\langle\chi_n|R_a|\chi_m\rangle + \boldsymbol{A}^{(a)}\cdot\boldsymbol{A}^{(b)}\langle\chi_n|R_aR_b|\chi_m\rangle\right]\ . \tag{A.24}$$

To do so we employ a leap-frog propagator [126] with time-step 0.005 a.u. and have verified its accuracy against the 4-th order Runge-Kutta [127, 128]. Taking u as the harmonic oscillator potential $\hat{x}_R^2 k/2$ and consequently

$$\langle R_a|\chi_j\rangle = \left(\frac{L}{\pi}\right)\frac{1}{2^j j!}H_j\left(L^{1/2}R_a\right)e^{-LR_a^2/2}\ , \tag{A.25}$$

the matrix elements present in Eqs. (A.23) and (A.24) are given in Table A.1. Here H_j are Hermite polynomials and $L = \sqrt{kM}$. Similarly the matrix elements required to evaluate Eq. (5.18) are found in Table A.2.

Table A.1: Harmonic oscillator matrix elements of the form $\langle\chi_n|R^n_{\{x,y,z\}}|\chi_m\rangle$, $n \in \{1, 2\}$.

Element	value
$\langle\chi_0\|R_x\|\chi_x\rangle = \langle\chi_0\|R_y\|\chi_y\rangle = \langle\chi_0\|R_z\|\chi_z\rangle$	$\frac{1}{\sqrt{2L}}$
$\langle\chi_0\|R_x^2\|\chi_0\rangle = \langle\chi_0\|R_y^2\|\chi_0\rangle = \langle\chi_0\|R_z^2\|\chi_0\rangle$	$\frac{1}{2L}$
$\langle\chi_x\|R_x^2\|\chi_x\rangle = \langle\chi_y\|R_y^2\|\chi_y\rangle = \langle\chi_z\|R_z^2\|\chi_z\rangle$	$\frac{3}{2L}$
$\langle\chi_x\|R_y^2\|\chi_x\rangle = \langle\chi_x\|R_z^2\|\chi_x\rangle =$ and others	$\frac{1}{2L}$
$\langle\chi_x\|R_xR_y\|\chi_y\rangle = \langle\chi_x\|R_xR_z\|\chi_z\rangle = \langle\chi_y\|R_yR_z\|\chi_z\rangle$	$\frac{1}{2L}$

Table A.2: Harmonic oscillator matrix elements of the form $\boldsymbol{p}_{nm} = \langle\chi_n|\hat{p}_R|\chi_m\rangle$.

n \ m	0	x	y	z
0	0	$-i\sqrt{\frac{L}{2}}\{1,0,0\}$	$-i\sqrt{\frac{L}{2}}\{0,1,0\}$	$-i\sqrt{\frac{L}{2}}\{0,0,1\}$
x	$i\sqrt{\frac{L}{2}}\{1,0,0\}$	0	0	0
y	$i\sqrt{\frac{L}{2}}\{0,1,0\}$	0	0	0
z	$i\sqrt{\frac{L}{2}}\{0,0,1\}$	0	0	0

Bibliography

[1] L. V. Keldysh, "Ionization in the field of a strong electromagnetic wave," Sov. Phys. JETP **20**, 1307–1314 (1965).

[2] L. B. Madsen, "Gauge invariance in the interaction between atoms and few-cycle laser pulses," Phys. Rev. A **65**, 053417 (2002).

[3] A. D. Bandrauk, F. Fillion-Gourdeau, and E. Lorin, "Atoms and molecules in intense laser fields: gauge invariance of theory and models," J. Phys. B **46**, 153001 (2013).

[4] W. C. Henneberger, "Perturbation method for atoms in intense light beams," Phys. Rev. Lett. **21**, 838–841 (1968).

[5] H. Muller, "An efficient propagation scheme for the time-dependent schrödinger equation in the velocity gauge," Laser Phys. **9**, 138–148 (1999), cited By 131.

[6] S. Patchkovskii and H. G. Muller, "Simple, accurate, and efficient implementation of 1-electron atomic time-dependent Schrödinger equation in spherical coordinates," Comput. Phys. Commun. **199**, 153 – 169 (2016).

[7] H. Muller, "Non-sequential double ionization of helium and related wave-function dynamics obtained from a five-dimensional grid calculation." Opt. Express **8**, 417–424 (2001).

[8] R. S. Varga, *Iterative analysis* (Springer, Prentice Hall, Englewood Cliffs, NJ, 1962).

[9] J. Crank and P. Nicolson, "A practical method for numerical evaluation of solutions of partial differential equations of the heat-conduction type," in *Mathematical Proceedings of the Cambridge Philosophical Society*, Vol. 43 (Cambridge University Press, 1947) pp. 50–67.

[10] D. W. Peaceman and H. H. Rachford, Jr, "The numerical solution of parabolic and elliptic differential equations," J. Soc. Indust. App. Math. **3**, 28–41 (1955).

[11] J. Douglas and H. H. Rachford, "On the numerical solution of heat conduction problems in two and three space variables," Trans. Am. Math. Soc. **82**, 421–439 (1956).

[12] L. Tao and A. Scrinzi, "Photo-electron momentum spectra from minimal volumes: the time-dependent surface flux method," New J. Phys. **14**, 013021 (2012).

[13] F. Morales, T. Bredtmann, and S. Patchkovskii, "iSURF: a family of infinite-time surface flux methods," J. Phys. B **49**, 245001 (2016).

[14] P. Eckle, M. Smolarski, P. Schlup, J. Biegert, A. Staudte, M. Schöffler, H. G. Muller, R. Dörner, and U. Keller, "Attosecond angular streaking," Nat. Phys. **4**, 565 (2008).

[15] L. A. MacColl, "Note on the transmission and reflection of wave packets by potential barriers," Phys. Rev. **40**, 621–626 (1932).

[16] A. S. Landsman and U. Keller, "Attosecond science and the tunnelling time problem," Phys. Rep. **547**, 1–24 (2015).

[17] T. E. Hartman, "Tunneling of a wave packet," J. Appl. Phys. **33**, 3427–3433 (1962).

[18] P. Eckle, A. N. Pfeiffer, C. Cirelli, A. Staudte, R. Dörner, H. G. Muller, M. Büttiker, and U. Keller, "Attosecond ionization and tunneling delay time measurements in helium," Science **322**, 1525–1529 (2008).

[19] A. N. Pfeiffer, C. Cirelli, M. Smolarski, D. Dimitrovski, M. Abu-Samha, L. B. Madsen, and U. Keller, "Attoclock reveals natural coordinates of the laser-induced tunnelling current flow in atoms," Nat. Phys. **8**, 76 (2012).

[20] A. S. Landsman, M. Weger, J. Maurer, R. Boge, A. Ludwig, S. Heuser, C. Cirelli, L. Gallmann, and U. Keller, "Ultrafast resolution of tunneling delay time," Optica **1**, 343–349 (2014).

[21] I. Ivanov and A. Kheifets, "Strong-field ionization of He by elliptically polarized light in attoclock configuration," Phys. Rev. A **89**, 021402 (2014).

[22] V. P. Majety and A. Scrinzi, "Absence of electron correlation effects in the helium attoclock setting," J. Mod. Opt. **64**, 1026–1030 (2017).

[23] N. Camus, E. Yakaboylu, L. Fechner, M. Klaiber, M. Laux, Y. Mi, K. Z. Hatsagortsyan, T. Pfeifer, C. H. Keitel, and R. Moshammer, "Experimental evidence for quantum tunneling time," Phys. Rev. Lett. **119**, 023201 (2017).

[24] L. Torlina, F. Morales, J. Kaushal, I. Ivanov, A. Kheifets, A. Zielinski, A. Scrinzi, H. G. Muller, S. Sukiasyan, M. Ivanov, and O. Smirnova, "Interpreting attoclock measurements of tunnelling times," Nat. Phys. **11**, 503 (2015).

[25] A. W. Bray, S. Eckart, and A. S. Kheifets, "Keldysh-Rutherford model for the attoclock," Phys. Rev. Lett. **121**, 123201 (2018).

[26] N. Douguet and K. Bartschat, "Attoclock setup with negative ions: A possibility for experimental validation," Phys. Rev. A **99**, 023417 (2019).

[27] H. Ni, U. Saalmann, and J.-M. Rost, "Tunneling exit characteristics from classical backpropagation of an ionized electron wave packet," Phys. Rev. A **97**, 013426 (2018).

[28] M. Han, P. Ge, Y. Fang, X. Yu, Z. Guo, X. Ma, Y. Deng, Q. Gong, and Y. Liu, "Unifying tunneling pictures of strong-field ionization with an improved attoclock," Phys. Rev. Lett. **123**, 073201 (2019).

[29] U. S. Sainadh, H. Xu, X. Wang, A. Atia-Tul-Noor, W. C. Wallace, N. Douguet, A. Bray, I. Ivanov, K. Bartschat, A. Kheifets, R. T. Sang, and I. V. Litvinyuk, "Attosecond angular streaking and tunnelling time in atomic hydrogen," Nature **568**, 75 (2019).

[30] C. Hofmann, A. S. Landsman, and U. Keller, "Attoclock revisited on electron tunnelling time," J. Mod. Opt. **66**, 1052–1070 (2019).

[31] H. Xie, M. Li, S. Luo, Y. Li, Y. Zhou, W. Cao, and P. Lu, "Energy-dependent angular shifts in the photoelectron momentum distribution for atoms in elliptically polarized laser pulses," Phys. Rev. A **96**, 063421 (2017).

[32] F. H. M. Faisal, "Multiphoton transitions. IV. bound-free transition integrals in compact forms," Journal of Physics B: Atomic and Molecular Physics **6**, 553–558 (1973).

[33] H. R. Reiss, "Gauges for intense-field electrodynamics," Phys. Rev. A **22**, 770–772 (1980).

[34] V. Mur, S. Popruzhenko, and V. Popov, "Energy and momentum spectra of photoelectrons under conditions of ionization by strong laser radiation (the case of elliptic polarization)," J. Exp. Theor. Phys. **92**, 777–788 (2001).

[35] D. B. Milošević, G. G. Paulus, D. Bauer, and W. Becker, "Above-threshold ionization by few-cycle pulses," J. Phys. B **39**, R203–R262 (2006).

[36] E. Rutherford, "LXXIX. the scattering of α and β particles by matter and the structure of the atom," Philos. Mag. **21**, 669–688 (1911).

[37] E. Everhart, G. Stone, and R. J. Carbone, "Classical calculation of differential cross section for scattering from a coulomb potential with exponential screening," Phys. Rev. **99**, 1287–1290 (1955).

[38] V. Véniard, R. Taïeb, and A. Maquet, "Phase dependence of $(n + 1)$-color $(n > 1)$ IR-UV photoionization of atoms with higher harmonics," Phys. Rev. A **54**, 721–728 (1996).

[39] P. M. Paul, E. S. Toma, P. Breger, G. Mullot, F. Augé, P. Balcou, H. G. Muller, and P. Agostini, "Observation of a train of attosecond pulses from high harmonic generation," Science **292**, 1689–1692 (2001).

[40] H. Muller, "Reconstruction of attosecond harmonic beating by interference of two-photon transitions," Appl. Phys. B **74**, s17–s21 (2002).

[41] P. Agostini, F. Fabre, G. Mainfray, G. Petite, and N. K. Rahman, "Free-free transitions following six-photon ionization of xenon atoms," Phys. Rev. Lett. **42**, 1127–1130 (1979).

[42] A. W. Bray, F. Naseem, and A. S. Kheifets, "Simulation of angular-resolved RABBITT measurements in noble-gas atoms," Phys. Rev. A **97**, 063404 (2018).

[43] N. M. Kroll and K. M. Watson, "Charged-particle scattering in the presence of a strong electromagnetic wave," Phys. Rev. A **8**, 804–809 (1973).

[44] A. Maquet and R. Taïeb, "Two-colour IR+XUV spectroscopies: the "soft-photon approximation"," J. Mod. Opt. **54**, 1847–1857 (2007).

[45] E. S. Toma and H. G. Muller, "Calculation of matrix elements for mixed extreme-ultraviolet–infrared two-photon above-threshold ionization of argon," J. Phys. B **35**, 3435–3442 (2002).

[46] I. A. Ivanov and A. S. Kheifets, "Angle-dependent time delay in two-color XUV+IR photoemission of He and Ne," Phys. Rev. A **96**, 013408 (2017).

[47] M. Y. Amusia, *Atomic photoeffect*, edited by K. T. Taylor (Plenum Press, New York, 1990).

[48] D. Guénot, K. Klünder, C. L. Arnold, D. Kroon, J. M. Dahlström, M. Miranda, T. Fordell, M. Gisselbrecht, P. Johnsson, J. Mauritsson, E. Lindroth,

A. Maquet, R. Taïeb, A. L'Huillier, and A. S. Kheifets, "Photoemission-time-delay measurements and calculations close to the 3*s*-ionization-cross-section minimum in Ar," Phys. Rev. A **85**, 053424 (2012).

[49] M. Isinger, R. J. Squibb, D. Busto, S. Zhong, A. Harth, D. Kroon, S. Nandi, C. L. Arnold, M. Miranda, J. M. Dahlström, E. Lindroth, R. Feifel, M. Gisselbrecht, and A. L'Huillier, "Photoionization in the time and frequency domain," Science **358**, 893–896 (2017).

[50] M. Schultze, M. Fieß, N. Karpowicz, J. Gagnon, M. Korbman, M. Hofstetter, S. Neppl, A. L. Cavalieri, Y. Komninos, T. Mercouris, C. A. Nicolaides, R. Pazourek, S. Nagele, J. Feist, J. Burgdörfer, A. M. Azzeer, R. Ernstorfer, R. Kienberger, U. Kleineberg, E. Goulielmakis, F. Krausz, and V. S. Yakovlev, "Delay in photoemission," Science **328**, 1658–1662 (2010).

[51] A. Sarsa, F. Gálvez, and E. Buendía, "Parameterized optimized effective potential for the ground state of the atoms He through Xe," At. Data Nucl. Data Tables **88**, 163 – 202 (2004).

[52] J. C. Slater, "A simplification of the Hartree-Fock method," Phys. Rev. **81**, 385–390 (1951).

[53] G. Wendin and A. F. Starace, "Perturbation theory in a strong-interaction regime with application to 4*d*-subshell spectra of Ba and La," J. Phys. B **11**, 4119 (1978).

[54] D. L. Miller and J. D. Dow, "Atomic pseudopotentials for soft X-ray excitations," Phys. Lett. A **60**, 16 – 18 (1977).

[55] Y. Ralchenko, A. E. Kramida, J. Reader, and NIST ASD Team, *NIST Atomic Spectra Database (version 3.1.5)*, Tech. Rep. (National Institute of Standards and Technology, Gaithersburg, MD., 2011).

[56] K. Codling, R. G. Houlgate, J. B. West, and P. R. Woodruff, "Angular distribution and photoionization measurements on the 2*p* and 2*s* electrons in neon," J. Phys. B **9**, L83 (1976).

[57] S. Heuser, A. Jiménez Galán, C. Cirelli, C. Marante, M. Sabbar, R. Boge, M. Lucchini, L. Gallmann, I. Ivanov, A. S. Kheifets, J. M. Dahlström, E. Lindroth, L. Argenti, F. Martín, and U. Keller, "Angular dependence of photoemission time delay in helium," Phys. Rev. A **94**, 063409 (2016).

[58] U. Fano, "Propensity rules: An analytical approach," Phys. Rev. A **32**, 617–618 (1985).

[59] J. Dahlström, D. Guénot, K. Klünder, M. Gisselbrecht, J. Mauritsson, A. L. Huillier, A. Maquet, and R. Taïeb, "Theory of attosecond delays in laser-assisted photoionization," Chem. Phys. **414**, 53–64 (2012).

[60] R. G. Houlgate, K. Codling, G. V. Marr, and J. B. West, "Angular distribution and photoionization cross section measurements on the $3p$ and $3s$ subshells of argon," J. Phys. B **7**, L470–L473 (1974).

[61] J. Mauritsson, M. B. Gaarde, and K. J. Schafer, "Accessing properties of electron wave packets generated by attosecond pulse trains through time-dependent calculations," Phys. Rev. A **72**, 013401 (2005).

[62] J. M. Dahlström and E. Lindroth, "Study of attosecond delays using perturbation diagrams and exterior complex scaling," J. Phys. B **47**, 124012 (2014).

[63] C. Cirelli, C. Marante, S. Heuser, C. L. M. Petersson, Á. J. Galán, L. Argenti, S. Zhong, D. Busto, M. Isinger, S. Nandi, S. Maclot, L. Rading, P. Johnsson, M. Gisselbrecht, M. Lucchini, L. Gallmann, J. M. Dahlström, E. Lindroth, A. L'Huillier, F. Martín, and U. Keller, "Anisotropic photoemission time delays close to a fano resonance," Nat. Commun. **9**, 955 (2018).

[64] D. L. Miller, J. D. Dow, R. G. Houlgate, G. V. Marr, and J. B. West, "The photoionisation of krypton atoms: a comparison of pseudopotential calculations with experimental data for the $4p$ asymmetry parameter and cross section as a function of the energy of the ejected photoelectrons," J. Phys. B **10**, 3205–3213 (1977).

[65] J. B. West, "Progress in photoionization spectroscopy of atoms and molecules: an experimental viewpoint," Appl. Opt. **19**, 4063–4067 (1980).

[66] D. Toffoli, M. Stener, and P. Decleva, "Application of the relativistic time-dependent density functional theory to the photoionization of xenon," J. Phys. B **35**, 1275 (2002).

[67] R. A. Phaneuf, A. L. D. Kilcoyne, N. B. Aryal, K. K. Baral, D. A. Esteves-Macaluso, C. M. Thomas, J. Hellhund, R. Lomsadze, T. W. Gorczyca, C. P. Ballance, S. T. Manson, M. F. Hasoglu, S. Schippers, and A. Müller, "Probing confinement resonances by photoionizing Xe inside a C_{60}^+ molecular cage," Phys. Rev. A **88**, 053402 (2013).

[68] A. S. Kheifets, "Time delay in valence-shell photoionization of noble-gas atoms," Phys. Rev. A **87**, 063404 (2013).

[69] S. E. Harris, "Generation of vacuum-ultraviolet and soft–X-ray radiation using high-order nonlinear optical polarizabilities," Phys. Rev. Lett. **31**, 341–344 (1973).

[70] M. Y. Kuchiev, "Atomic antenna," JETP Lett **45**, 404–406 (1987).

[71] P. B. Corkum, "Plasma perspective on strong field multiphoton ionization," Phys. Rev. Lett. **71**, 1994–1997 (1993).

[72] K. J. Schafer, B. Yang, L. F. DiMauro, and K. C. Kulander, "Above threshold ionization beyond the high harmonic cutoff," Phys. Rev. Lett. **70**, 1599–1602 (1993).

[73] A. McPherson, G. Gibson, H. Jara, U. Johann, T. S. Luk, I. A. McIntyre, K. Boyer, and C. K. Rhodes, "Studies of multiphoton production of vacuum-ultraviolet radiation in the rare gases," J. Opt. Soc. Am. B **4**, 595–601 (1987).

[74] J. Wildenauer, "Generation of the ninth, eleventh, and fifteenth harmonics of iodine laser radiation," J. Appl. Phys. **62**, 41–48 (1987).

[75] O. Smirnova and M. Ivanov, "Multielectron high harmonic generation: Simple man on a complex plane," Attosecond and XUV Physics , 201–256 (2014).

[76] A. L'Huillier, M. Lewenstein, P. Salières, P. Balcou, M. Y. Ivanov, J. Larsson, and C. G. Wahlström, "High-order harmonic-generation cutoff," Phys. Rev. A **48**, R3433–R3436 (1993).

[77] M. Lewenstein, P. Balcou, M. Y. Ivanov, A. L'Huillier, and P. B. Corkum, "Theory of high-harmonic generation by low-frequency laser fields," Phys. Rev. A **49**, 2117–2132 (1994).

[78] P. Salières, A. L'Huillier, and M. Lewenstein, "Coherence control of high-order harmonics," Phys. Rev. Lett. **74**, 3776–3779 (1995).

[79] M. Lewenstein, P. Salières, and A. L'Huillier, "Phase of the atomic polarization in high-order harmonic generation," Phys. Rev. A **52**, 4747–4754 (1995).

[80] C. Kan, C. E. Capjack, R. Rankin, and N. H. Burnett, "Spectral and temporal structure in high harmonic emission from ionizing atomic gases," Phys. Rev. A **52**, R4336–R4339 (1995).

[81] M. B. Gaarde, J. L. Tate, and K. J. Schafer, "Macroscopic aspects of attosecond pulse generation," J. Phys. B **41**, 132001 (2008).

[82] E. Lorin, S. Chelkowski, and A. Bandrauk, "A numerical maxwell–schrödinger model for intense laser–matter interaction and propagation," Comp. Phys. Commun. **177**, 908 – 932 (2007).

[83] A. D. Shiner, C. Trallero-Herrero, N. Kajumba, H.-C. Bandulet, D. Comtois, F. Légaré, M. Giguère, J.-C. Kieffer, P. B. Corkum, and D. M. Villeneuve, "Wavelength scaling of high harmonic generation efficiency," Phys. Rev. Lett. **103**, 073902 (2009).

[84] A. D. Shiner, B. E. Schmidt, C. Trallero-Herrero, H. J. Wörner, S. Patchkovskii, P. B. Corkum, J.-C. Kieffer, F. Légaré, and D. M. Villeneuve, "Probing collective multi-electron dynamics in xenon with high-harmonic spectroscopy," Nat. Phys. **7**, 464–467 (2011).

[85] D. Faccialà, S. Pabst, B. D. Bruner, A. G. Ciriolo, S. De Silvestri, M. Devetta, M. Negro, H. Soifer, S. Stagira, N. Dudovich, and C. Vozzi, "Probe of multielectron dynamics in xenon by caustics in high-order harmonic generation," Phys. Rev. Lett. **117**, 093902 (2016).

[86] D. Faccialà, S. Pabst, B. D. Bruner, A. G. Ciriolo, M. Devetta, M. Negro, P. P. Geetha, A. Pusala, H. Soifer, N. Dudovich, S. Stagira, and C. Vozzi, "High-order harmonic generation spectroscopy by recolliding electron caustics," J. Phys. B **51**, 134002 (2018).

[87] P. B. Corkum, N. H. Burnett, and M. Y. Ivanov, "Subfemtosecond pulses," Opt. Lett. **19**, 1870–1872 (1994).

[88] P. Antoine, B. Piraux, D. B. Milošević, and M. Gajda, "Generation of ultrashort pulses of harmonics," Phys. Rev. A **54**, R1761–R1764 (1996).

[89] P. Antoine, A. L'Huillier, and M. Lewenstein, "Attosecond pulse trains using high–order harmonics," Phys. Rev. Lett. **77**, 1234–1237 (1996).

[90] G. Vampa, C. R. McDonald, G. Orlando, D. D. Klug, P. B. Corkum, and T. Brabec, "Theoretical analysis of high-harmonic generation in solids," Phys. Rev. Lett. **113**, 073901 (2014).

[91] G. Vampa, T. J. Hammond, N. Thiré, B. E. Schmidt, F. Légaré, C. R. McDonald, T. Brabec, and P. B. Corkum, "Linking high harmonics from gases and solids," Nature **522**, 462–464 (2015).

[92] S. Ghimire and D. A. Reis, "High-harmonic generation from solids," Nature Physics **15**, 10–16 (2019).

[93] M. A. Fareed, V. V. Strelkov, M. Singh, N. Thiré, S. Mondal, B. E. Schmidt, F. Légaré, and T. Ozaki, "Harmonic generation from neutral manganese atoms in the vicinity of the giant autoionization resonance," Phys. Rev. Lett. **121**, 023201 (2018).

[94] L. J., "LXIII. on the theory of the magnetic influence on spectra; and on the radiation from moving ions," Philos. Mag. **44**, 503–512 (1897).

[95] B. Sundaram and P. W. Milonni, "High-order harmonic generation: Simplified model and relevance of single-atom theories to experiment," Phys. Rev. A **41**, 6571–6573 (1990).

[96] J. L. Krause, K. J. Schafer, and K. C. Kulander, "Calculation of photoemission from atoms subject to intense laser fields," Phys. Rev. A **45**, 4998–5010 (1992).

[97] K. Burnett, V. C. Reed, J. Cooper, and P. L. Knight, "Calculation of the background emitted during high-harmonic generation," Phys. Rev. A **45**, 3347–3349 (1992).

[98] P. Ehrenfest, "Bemerkung über die angenäherte gültigkeit der klassischen mechanik innerhalb der quantenmechanik," Zeitschrift für Physik **45**, 455–457 (1927).

[99] A. S. Kheifets, A. W. Bray, and I. Bray, "Attosecond time delay in photoemission and electron scattering near threshold," Phys. Rev. Lett. **117**, 143202 (2016).

[100] T. Morishita, A. Le, Z. Chen, and C. D. Lin, "Accurate retrieval of structural information from laser-induced photoelectron and high-order harmonic spectra by few-cycle laser pulses," Phys. Rev. Lett. **100**, 013903 (2008).

[101] A. Le, R. R. Lucchese, S. Tonzani, T. Morishita, and C. D. Lin, "Quantitative rescattering theory for high-order harmonic generation from molecules," Phys. Rev. A **80**, 013401 (2009).

[102] C. D. Lin, A. Le, C. Jin, and H. Wei, "Elements of the quantitative rescattering theory," J. Phys. B **51**, 104001 (2018).

[103] M. Y. Amusia and L. V. Chernysheva, *Computation of atomic processes: A handbook for the ATOM programs* (CRC Press, 1997).

[104] W. R. Johnson and C. D. Lin, "Multichannel relativistic random-phase approximation for the photoionization of atoms," Phys. Rev. A **20**, 964–977 (1979).

[105] F. Cloux, B. Fabre, and B. Pons, "Semiclassical description of high-order-harmonic spectroscopy of the cooper minimum in krypton," Phys. Rev. A **91**, 023415 (2015).

[106] M. Y. Amusia and N. A. Cherepkov, "Many-electron correlations in scattering processes," Case Stud. At. Phys. **5**, 47–179 (1975).

[107] D. Thouless, *Quantum mechanics of many-body systems* (Academic Press, New York, 1961) Chap. 4,5.

[108] T. N. Chang and U. Fano, "Many-body theory of atomic transitions," Phys. Rev. A **13**, 263–281 (1976).

[109] A. Kheifets, A. Mandal, P. C. Deshmukh, V. K. Dolmatov, D. A. Keating, and S. T. Manson, "Relativistic calculations of angle-dependent photoemission time delay," Phys. Rev. A **94**, 013423 (2016).

[110] A. D. Shiner, B. E. Schmidt, C. Trallero-Herrero, P. B. Corkum, J.-C. Kieffer, F. Légaré, and D. M. Villeneuve, "Observation of cooper minimum in krypton using high harmonic spectroscopy," J. Phys. B **45**, 074010 (2012).

[111] O. Hassouneh, A. C. Brown, and H. W. van der Hart, "Harmonic generation by noble-gas atoms in the near-IR regime using ab initio time-dependent R-matrix theory," Phys. Rev. A **90**, 043418 (2014).

[112] J. P. Connerade, J. E. Esteva, and R. Karnatak, *Giant Resonance in Atoms, Molecules and Solids*, Nato Science Series B, Vol. 151 (Plenum, New York, 1986).

[113] C. Trallero-Herrero, C. Jin, B. E. Schmidt, A. D. Shiner, J.-C. Kieffer, P. B. Corkum, D. M. Villeneuve, C. D. Lin, F. Légaré, and A. T. Le, "Generation of broad XUV continuous high harmonic spectra and isolated attosecond pulses with intense mid-infrared lasers," J. Phys. B **45**, 011001 (2011).

[114] M. V. Fedorov and A. M. Movsesian, "Field-induced effects of narrowing of photoelectron spectra and stabilisation of Rydberg atoms," J. Phys. B **21**, L155–L158 (1988).

[115] J. H. Eberly and K. C. Kulander, "Atomic stabilization by super-intense lasers," Science **262**, 1229–1233 (1993).

[116] V. C. Reed and K. Burnett, "Ionization of atoms in intense laser pulses using the Kramers-Henneberger transformation," Phys. Rev. A **42**, 3152–3155 (1990).

[117] T. Nubbemeyer, K. Gorling, A. Saenz, U. Eichmann, and W. Sandner, "Strong-field tunneling without ionization," Phys. Rev. Lett. **101**, 233001 (2008).

[118] U. Eichmann, T. Nubbemeyer, H. Rottke, and W. Sandner, "Acceleration of neutral atoms in strong short-pulse laser fields," Nature **461**, 1261 (2009).

[119] H. Zimmermann, S. Patchkovskii, M. Ivanov, and U. Eichmann, "Unified time and frequency picture of ultrafast atomic excitation in strong laser fields," Phys. Rev. Lett. **118**, 013003 (2017).

[120] G. Grynberg, A. Aspect, and C. Fabre, *Introduction to quantum optics: from the semi-classical approach to quantized light* (Cambridge university press, 2010) Chap. 3B, pp. 239–246.

[121] M. Lax, W. H. Louisell, and W. B. McKnight, "From Maxwell to paraxial wave optics," Phys. Rev. A **11**, 1365–1370 (1975).

[122] G. Lüders, "Über die zustandsänderung durch den meßprozeß," Annalen der Physik **443**, 322–328 (1950).

[123] S. Martinez, "A search for the physical content of Luders' rule," Synthese **82**, 97–125 (1990).

[124] I. G. Bobo, "On quantum conditional probability," Theoria. Revista de Teoría, Historia y Fundamentos de la Ciencia **28**, 115–137 (2013).

[125] Q. Wei, P. Wang, S. Kais, and D. Herschbach, "Pursuit of the Kramers-Henneberger atom," Chem. Phys. Lett. **683**, 240 – 246 (2017).

[126] J. A. Snyman, "A new and dynamic method for unconstrained minimization," Appl. Math. Model. **6**, 449 – 462 (1982).

[127] C. Runge, "Ueber die numerische auösung von dierentialgleichungen," Math. Ann. **46** (1895).

[128] W. Kutta, "Beitrag zur naherungsweisen integration totaler differentialgleichungen," Z. Math. Phys. **46**, 435–453 (1901).